MAPPING AND ANALYZING THE FULL VASCULAR NETWORK IN THE MOUSE BRAIN AT SUBMICROMETER RESOLUTION

A Dissertation

by

JUNSEOK LEE

Submitted to the Office of Graduate and Professional Studies of
Texas A&M University
in partial fulfillment of the requirements for the degree of

DOCTOR OF PHILOSOPHY

Chair of Committee,	Yoonsuck Choe
Committee Members,	John Keyser
	Scott Schaefer
	Louise Abbott
Head of Department,	Dilma Da Silva

August 2018

Major Subject: Computer Science

ABSTRACT

Mapping the microvascular networks in the brain can lead to significant scientific and clinical insights. The recent advances of high-throughput physical sectioning light microscopy have greatly contributed to reducing the gap in neuroimaging between large-scale, low-resolution techniques and small-scale, high-resolution methods. The Brain Networks Laboratory at Texas A&M University developed a serial sectioning microscopy technique called the Knife-Edge Scanning Microscopy (KESM) to section and image the entire mouse brain at submicrometer resolution. The KESM can be used to obtain information about a small animal organ, such as a whole mouse or rat brain, at submicrometer resolution of $0.6\,\mu\mathrm{m} \times 0.7\,\mu\mathrm{m} \times 1.0\,\mu\mathrm{m}$ voxel size. In our effort to map the entire vascular network in the mouse brain, the Brain Networks Laboratory perfused the mouse brain vessels with India ink, and used the KESM to image the prepared brain.

However, the image data size of the entire mouse brain from the KESM is about 1.5 TB, and is not easy to handle or analyze. Moreover, the dataset contains unintended noise from the serial sectioning process. Because of these difficulties, previous studies partially analyzed the structure of the mouse brain by manually selecting a small, noise-free portion (volume size under $1000 \times 1000 \times 1000$ voxel) in the dataset. In addition to the KESM dataset, there have been studies for vessel reconstruction and analysis of the whole mouse brain at lower resolution or of partial brain regions at submicrometer resolution. However, to the best of our knowledge, there has been no study for vessel reconstruction and analysis of the whole mouse brain at submicrometer resolution.

In this dissertation, I will present my dataset, and computational algorithms I developed to trace and analyze morphological properties of the whole mouse brain vascular network at submicrometer resolution. Since the data is available across the entire brain in full detail (the smallest capillaries can be observed in our data), it enables the comparison of regional differences in morphological properties and provides the systematic cleaning to remove and consolidate erroneous images automatically, which enables the full tracing and analysis of the whole KESM mouse brain

dataset with richer vasculature information. I expect this dissertation can provide rich insights to brain and neuroscience researchers.

DEDICATION

To my wife, my children, my parents, my father-in-law, and my mother-in-law,

Minjeong Kim, Dain Lee, Dayul Lee,

Jongkeun Lee, Yeonsik Shin, Jaekwan Kim, and Youngja Kim.

ACKNOWLEDGMENTS

First of all, I would like to thank my adviser Dr. Yoonsuck Choe for his sincere interest and endless support. He taught me the true meaning of the adviser. I would also like to thank Dr. Jaewook Yoo, for sharing my concerns about this research and giving me valuable comments.

I would also like to thank the committee members Dr. John Kaiser, Dr. Scott Schaefer, and Dr. Louise Abbott. They gave me continuous interest and advice to my research. I would also like to thank my laboratory members for their curiosity and support: Dr. Chul Sung, Michael Nowak, Han Wang, Khuong Nguyen, Qing Wan, Wenjie Yang, Wencong Zhang, Shashwat Lal Das, Ankur Singhal, Sungjune Lim, Wookyung An, Randall Reams, Dr. Sangheon Lee, and Dr. Changyeol Yum. I would also like to thank Kelly Erwin for carefully reading and commenting on the manuscript.

I am grateful to Heechul Yoon (Ph.D. student at the University of Alabama), Yongjun Park (Ph.D. student at the University of Texas at Dallas), Daeeun Kim, and Kyunghoon Kim for providing valuable comments and good relationship. I am also grateful to the Republic of Korea Army and Korea Army Academy at Yeongcheon for providing the doctoral program opportunity and scholarship. In particular, Dr. Kiwan Kim and Dr. Namguk Hur encouraged me to do my best.

Finally, I am deeply grateful to my wife, Minjeong Kim, and my daughters, Dain Lee and Dayul Lee, for their endless patience, belief, and love.

This research was supported by the National Science Foundation (grants #1256086, #1208174, #0905041, and NIH/NINDS grant #1R01-MH66991).

Junseok Lee

Texas A&M University

August 2018

TABLE OF CONTENTS

Page

LIST OF FIGURES

FIGURE Page

LIST OF TABLES

TABLE Page

INTRODUCTION

Despite the long time and effort, we have not been able to pinpoint the precise cause of Alzheimer's Disease (AD) yet. [38, 92]. Some studies [22, 21, 24, 92] claim that AD is caused by cerebral vascular injury. A progressive microvascular disease is an example of a major factor in increasing the risk of stroke and vascular dementia [42, 69, 39]. In addition, vascular structure analysis has been used in traumatic brain injury and retinal vasculature studies where classical vascular analysis (bifurcation points, length, vessel diameter, and vessel density) was considered [1, 66]. Therefore, the study of microvasculature structures is very important and can help the understanding of the role of the blood vessel organization of the brain, in brain disorders, and as a result help advances in clinical research.

It has been challenging historically mapping and imaging the whole mouse brain at submicrometer resolution [4]. However, recent advances in imaging techniques have enabled brain blood vessel studies to be conducted in ways that were previously unthinkable [43]. The Knife-Edge Scanning Microscope (KESM) [60, 12, 13, 14] was developed by the Brain Networks Laboratory at Texas A&M University. The KESM allows high-throughput, and high-resolution images of the entire mouse brain. A high-speed line-scan camera captures the sectioned tissue when it passes over the diamond knife as the top of the specimen block is being cut. The imaged voxel size in KESM is $0.6\,\mu\mathrm{m} \times 0.7\,\mu\mathrm{m} \times 1.0\,\mu\mathrm{m}$ and up to $\sim 1\,\mathrm{cm}^3$ volume of tissue that can be imaged. The resulting dataset size is about 1.5 TB of raw data. The KESM was used to scan the C57BL/6J mouse brain stained with India-ink (vascular network), Golgi (neuronal morphology), and Nissl (soma distribution).

In this dissertation, I used the C57BL/6J mouse brain stained with India-ink data set acquired by the KESM for analyzing the microvascular structure. The whole-brain cerebrovascular

data of the C57BL/6J mouse perfused with India-ink was obtained from the KESM Brain Atlas (KESMBA) website (kesmba.cs.tamu.edu) as a sequence of 8560 coronal image slices of dimension 12000×12000 px, at a voxel resolution of approximately $0.6\,\mu\mathrm{m}$ laterally and $0.7\,\mu\mathrm{m}$ longitudinally by $1.0\,\mu\mathrm{m}$ axially [15]. This dataset underwent post-acquisition processing to remove lighting defects and noise due to mechanical chatter prior to being published to the KESMBA [87].

Motivation

Whole mouse brain microvascular images at submicrometer scale can be obtained by Knife-Edge Scanning Microscopy (KESM) [57]. However, due to the large size of the image dataset and the noise from the serial sectioning process of the KESM, whole mouse brain vascular reconstruction and analysis with submicrometer resolution have not been achieved yet, while several previous studies [85, 50, 64] demonstrated manually selected small noise-free portion of the KESM dataset. In addition to the KESM dataset, there have been study [94] for vessel reconstruction and analysis of the whole mouse brain at lower resolution or of partial brain regions at submicrometer resolution. However, to the best of my knowledge, there has been no study for vessel reconstruction and analysis of the whole mouse brain at submicrometer resolution.

To build and analyze the full structure of the whole mouse brain at submicrometer resolution, I propose four goals as follows: (1) Preparing a whole mouse brain dataset for 3D reconstruction. (2) Measuring and categorizing by the vascular diameter (3) 3D tracing and geometric analysis. (4) Convolutional Neural Network (CNN) for the automatic classification of impaired mouse brain images.

Approach

(1) For preparing the whole mouse brain dataset, an axial direction sub-sampling method and a convex hull masking method are proposed. First, I propose an axial direction sub-sampling method, where averaging consecutive image pairs and replacing significant degradation images with a blank image are used. The resulting sub-sampled images are greatly reduced in size for visualizing and analyzing but retain more information than sub-sampled images from other sub-

sampling methods [6, 50]. In addition, I propose a convex hull masking method to automatically detect the boundary of the mouse brain and eliminate unnecessary information (including noise) outside of the region of interest(ROI). This method allows me to use a more aggressive threshold option, which results in more abundant vascular information. (2) For measuring and categorizing by the vascular diameter of the dataset from (1), I will calculate the diameters of the mouse brain vessels in the section images and categorize them according to the diameter sizes. Then, for tracing, the center points of two vessels are connected if their cross-sectional regions are connected in consecutive slices along the z-axis [50]. The distributions of the vessels along with different diameter sizes are visualized and analyzed using the centerlines and diameters. (3) For 3D tracing and geometry analysis, I will create a 3D reconstruction of the whole mouse brain. Then I will trace the vascular structure using 3D Visualization Assisted Analysis (Vaa3D) [71] software. Based on the tracing result, I will analyze geometric features of the vascular structure. (4) For the automatic classification of impaired mouse brain images, I will apply the Convolutional Neural Network (CNN) [45] method to the KESM dataset. I expect that using CNN could improve the classification accuracy of the impaired images for the KESM dataset compared to the baseline method, Support Vector Machine (SVM) [9]. Previously, significantly damaged or impaired images were collected manually due to the low performance of automatic classifications.

I expect this dissertation to enable the full tracing and analysis of the whole mouse brain along with the systematic cleaning to remove and consolidate erroneous images automatically. In addition, I expect this dissertation to provide rich insights into the brain for neuroscience researchers.

Organization of the Dissertation

The rest of this dissertation is organized as follows. In Chapter 2, I discuss background information that is the KESM and the KESM India ink dataset. In particular, I will describe the operational principle and process of the KESM and the characteristics and resolution of the KESM India ink dataset.

In Chapter 3, I describe preparing a whole mouse brain data set for 3D reconstruction. I will explain in detail the image subsampling method which can maintain more vessel information and

the technique which can automatically remove noise. I also use two kinds of thresholding method to compare and analyze the results of a dataset according to the options selected when binarizing the image.

In Chapter 4, I focus on categorizing blood vessels according to their diameter size. Then, the categorization of the blood vessels classified according to the size of the diameter can be visualized in 3D.

In Chapter 5, I describe tracing and geometric analysis of the blood vessels using the dataset from Chapter 2. In particular, traces of blood vessels in 3D can be traced, and the characteristics of blood vessels can be geometrically analyzed by obtaining the diameter, number of the bifurcation points, surface, and volume values of the blood vessels.

In Chapter 6, I discuss the use of Convolutional Neural Network (CNN) for the automatic classification of impaired mouse brain images. Specifically, in order to overcome the inconvenience of manually classifying images, I will design a platform and implement a system that automatically classifies images using machine learning techniques.

In Chapter 7, I describe related works and its results for comparing and analyzing my results.

Finally, I will discuss and conclude the dissertation in Chapter 8.

BACKGROUND

Knife-Edge Scanning microscope (KESM)

Critical gap in neuroimaging between large-scale, low-resolutions methods and small-scale, high-resolutions techniques has been significantly addressed by recent advances in high-throughput physical sectioning light microscopy. Knife-Edge Scanning Microscopy (KESM) is one approach that has emerged from such an advance in neuroimaging and Table.2.1 provides the summary comparison of high-throughput imaging and analysis methods. Figure 2.1 shows the KESM (US patent $\#6,744,572$) [59] developed by the Brain Networks Laboratory at Texas A&M University [60]. The KESM allows obtaining high-throughput, high-resolution images of whole mouse brains at submicrometer-level [14]. A high-speed line-scan camera captures the sectioned tissue when it passes over the diamond knife as the top of the specimen block is being cut (Figure 2.1b). The imaged voxel size in KESM is $0.6\,\mu\mathrm{m} \times 0.7\,\mu\mathrm{m} \times 1.0\,\mu\mathrm{m}$ and up to $\sim 1\,\mathrm{cm}^3$ volume of tissue can be imaged within 100 hours. The resulting dataset size is about 1.5 TB of raw data. The KESM was used to scan the C57BL/6L mouse brain stained with India-ink (vascular network) [14], Golgi (neuronal morphology), and Nissl (soma distribution) [55].

KESM India ink dataset

Whole-brain cerebrovasculature data of the C57BL/6J mouse perfused with India-ink was obtained from the KESM as a sequence of 8,560 coronal image slices of dimension 7,790 px $\times$ 6,050 px, at a voxel resolution of approximately $1.2\,\mu\mathrm{m}$ laterally and $1.4\,\mu\mathrm{m}$ longitudinally by $1.0\,\mu\mathrm{m}$ axially [15].

Figure 2.2 illustrates the process of obtaining a tissue image using KESM. Through this process, I get the cross section of the mouse brain image shown in Figure 2.3. Figure 2.3 is a cross

Table 2.1: Summary comparison of high-throughput imaging and analysis methods

Method	Resolution (x,y)	Resolution (z)	Volume	Time
All-Optical Histology [91]	$0.5\,\mu m$	$1\,\mu m$	$1\,cm^3$	$\sim 900\ hours$
KESM	$0.3 \sim 0.6\,\mu m$	$0.5 \sim 1\,\mu m$	$1\,cm^3$	$\sim 100\ hours$
Array Tomography [62]	$\sim 0.6\,\mu m$	$0.05 \sim 0.2\,\mu m$	$100\,\mu m^3$	N/A
SBF-SEM* [23]	$\sim 0.01\,\mu m$	$\sim 0.03\,\mu m$	$\sim 500 \mu m^3$	N/A
ATLUM** [33]	$\sim 0.01\,\mu m$	$0.05\,\mu m$	$\sim 2.15 mm^3$	N/A

Adapted from [12].
*SBF-SEM (Serial Block-Face Scanning Election Microscopy)
**ATLUM (Automatic Tape-Collecting Lathe Ultramicrotome)

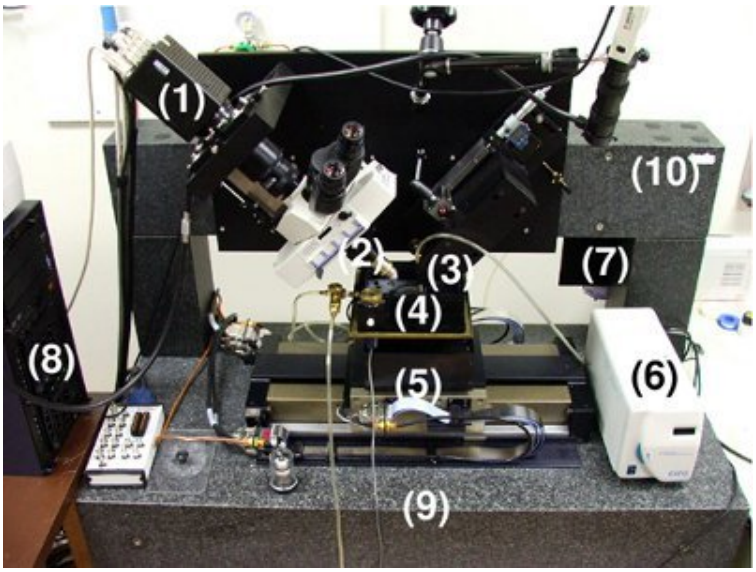

(a) KESM

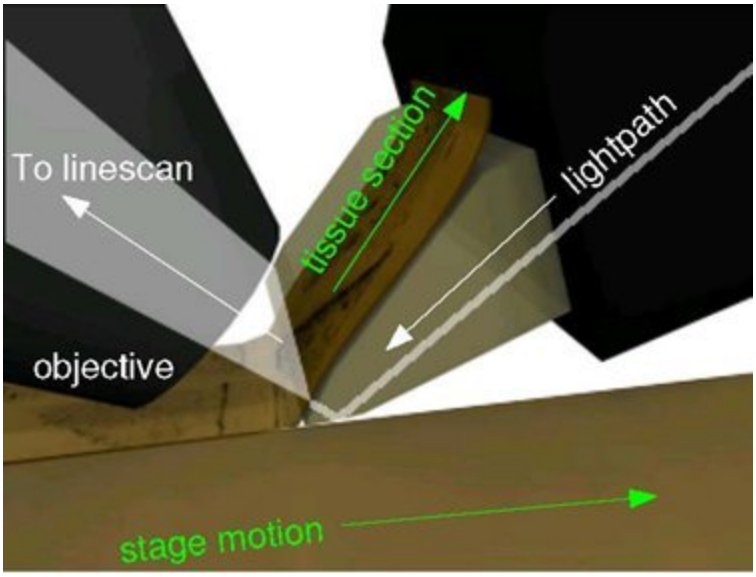

(b) The principle of operation

Figure 2.1: **Knife-Edge Scanning Microscope (KESM).** (a) Major components of the KESM are shown: (1) high-speed line-scan camera, (2) microscope objective, (3) diamond knife assembly and light collimator, (4) specimen tank (for water immersion imaging), (5) three-axis precision air-bearing stage, (6) white-light microscope illuminator, (7) water pump (in the black) for the removal of sectioned tissue, (8) PC server for stage control and image acquisition, (9) grantie base, and (10) grantie bridge. (b) An illustration of the principle of operation of the KESM. Adapted from [14].

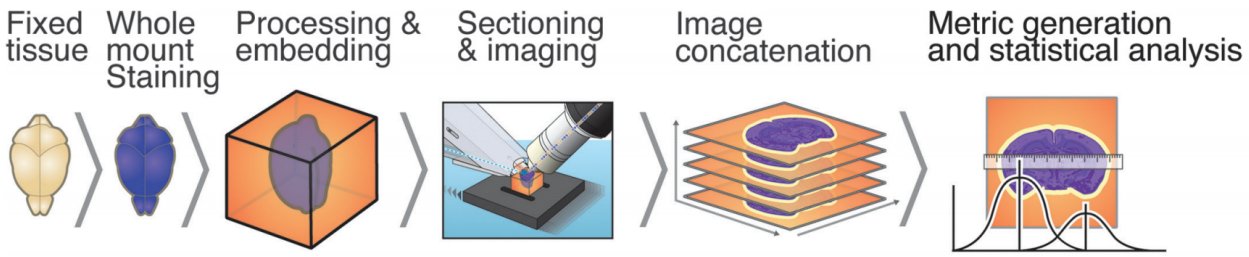

Figure 2.2: **KESM tissue imaging workflow.** It illustrates the process of obtaining a tissue image using KESM. Adapted from [72].

section of the mouse brain and the black parts are blood vessel stained with India ink [14]. This image contains noise as well as information about blood vessels, and it requires various image processing techniques to analyze only the blood vessels portion. Figure 2.4 is the KESM India ink data. Figure 2.4a ia a zoom-in of the vascular data (width ~ $100\,\mu\mathrm{m}$) and Figure 2.4b ~ Figure 2.4d are 3D visualizations of the KESM India ink sub-sampled dataset for the whole mouse brain vasculature (width ~ 10 mm) [14].

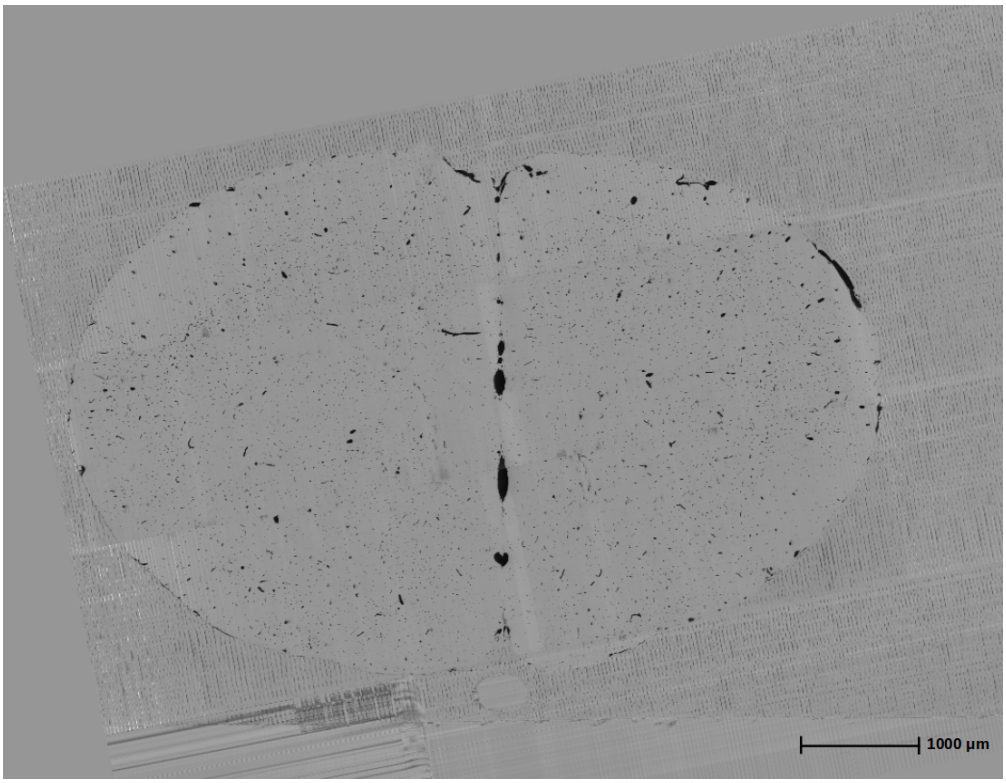

Figure 2.3: **A cross section of the mouse brain.** The black parts are vascular stained with India ink. Coronal view (↑ : Dorsal, ↓ : Ventral).

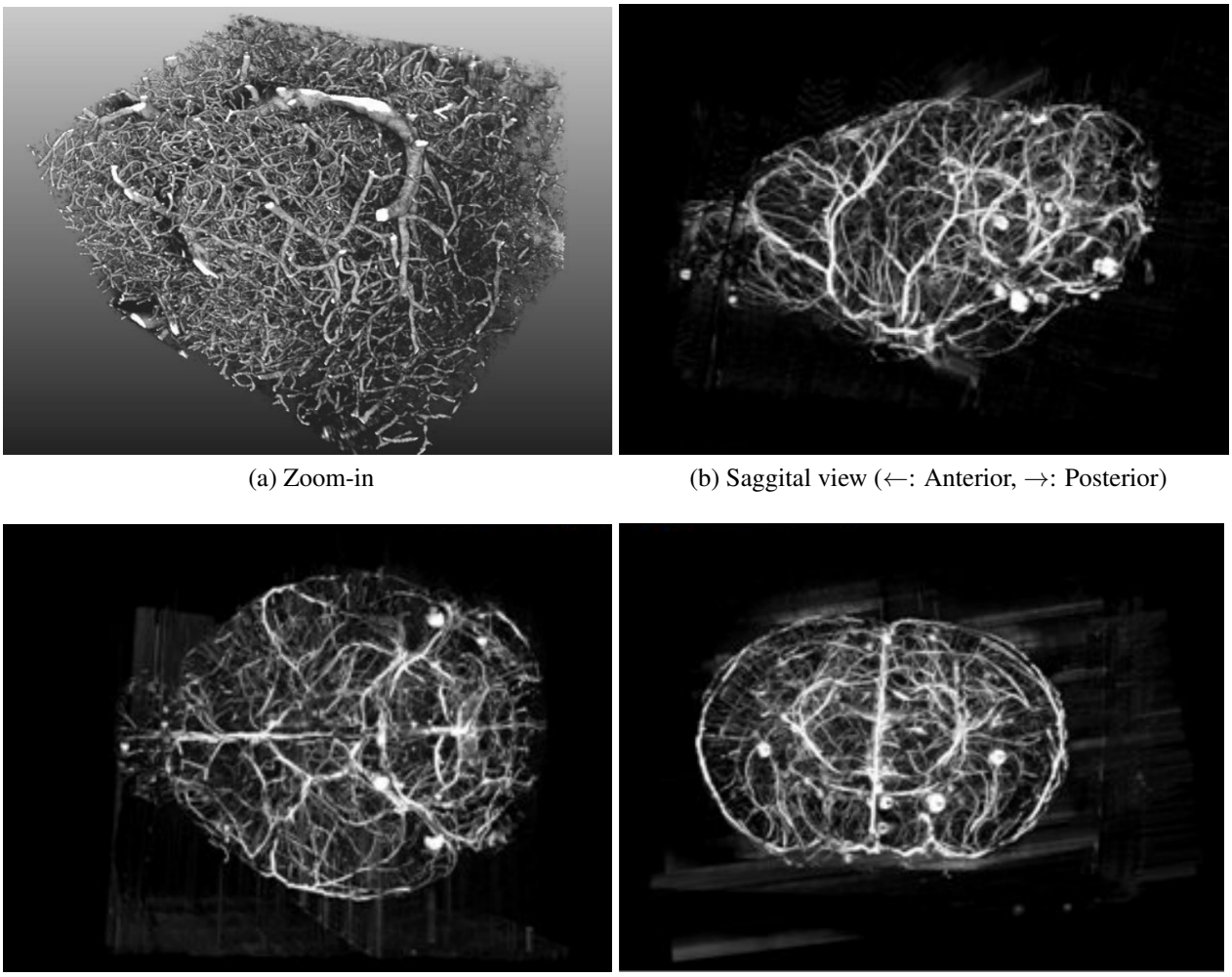

(a) Zoom-in

(b) Saggital view (←: Anterior, →: Posterior)

(c) Horizontal view (←: Anterior, →: Posterior)

(d) Coronal view (↑: Dorsal, ↓: Ventral)

Figure 2.4: **KESM India ink data.** (a) Zoom-in of the vascular data (width a 1.5 mm-wide block). (b ~ d) 3D visualizations of the KESM India ink sub-sampled dataset for the whole mouse brain vasculature (width ~ 10mm). (a) adapted from [13]. (b ~ d) adapted from [14]

PREPARING A WHOLE MOUSE BRAIN DATA SET FOR 3D RECONSTRUCTION

Motivation

Noise in KESM data

KESM represents a classical microscope and has typical noise as such and, several other types of noise. These entail camera alignment, lighting frequency, and small lighting irregularities caused by knife vibrations during the cutting process [57]. Figure 3.1 shows lighting defects and knife chatter. The effect of these unique noises can reduce the amount of information that can be obtained from the image.

Typical sub-sampling method

The images (Image Z ~ Z+7 in Figure 3.2) are cross-sections of the mouse brain as shown in Figure 2.3. Figure 3.2 describes typical sub-sampling by z-axis. Using the typical sub-sampling method as shown in Figure 3.2a, four consecutive images (Image Z ~ Z+3) use only one image (Image Z) while going through two stages of sub-sampling by z-axis. In addition, if the first image (Image Z+4)of four consecutive images (Image Z+4 ~ Z+7) is a heavily damaged image as shown in Figure 3.2b, it is removed from the dataset while undergoing the two-step sub-sampling process by z-axis. If the image is removed in this way, it will distort the size of the mouse brain dataset. The following image processing step proposes a down-sampling method that can take advantage of all four consecutive images without distorting the dataset.

(a) Lighting Defects (arrows)

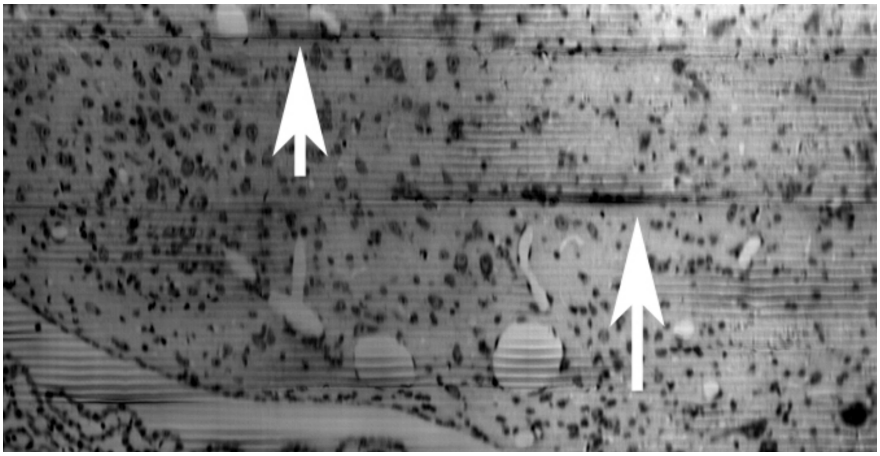

(b) Knife Chatter (arrows)

Figure 3.1: **Noise of KESM data.** KESM represents a classical microscope and several other types of noise. These entail camera alignment, lighting frequency, and small lighting irregularities caused by knife vibrations when the cutting process. (a) shows lighting defects and (b) shows knife chatter. Adapted from [57].

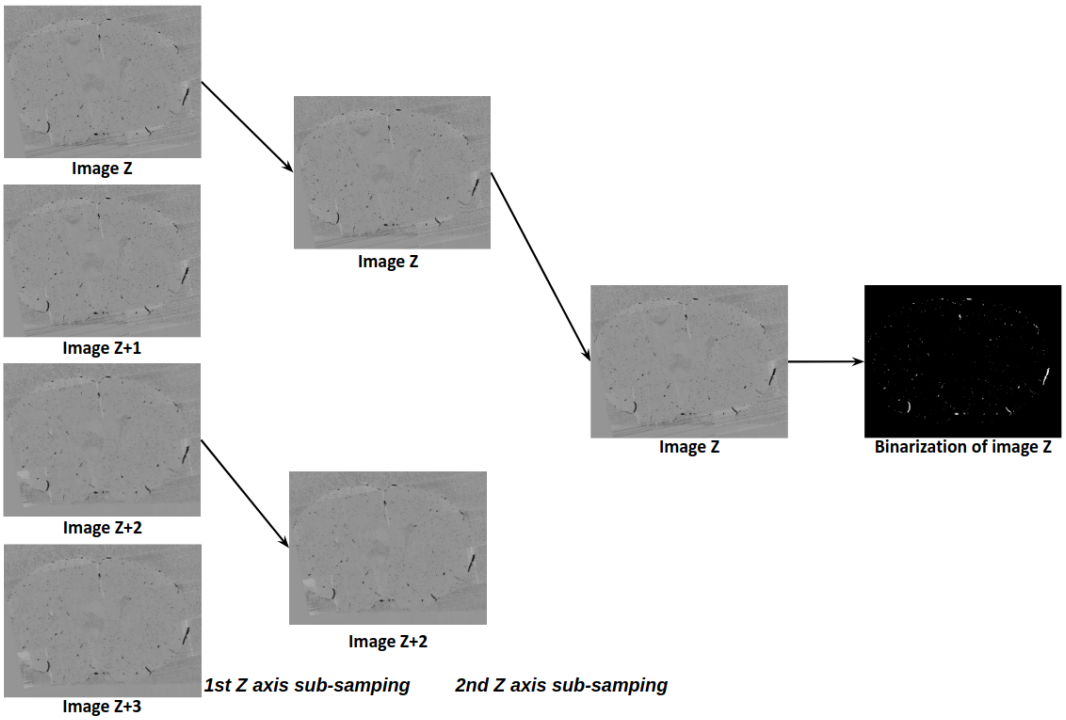

(a) Good images

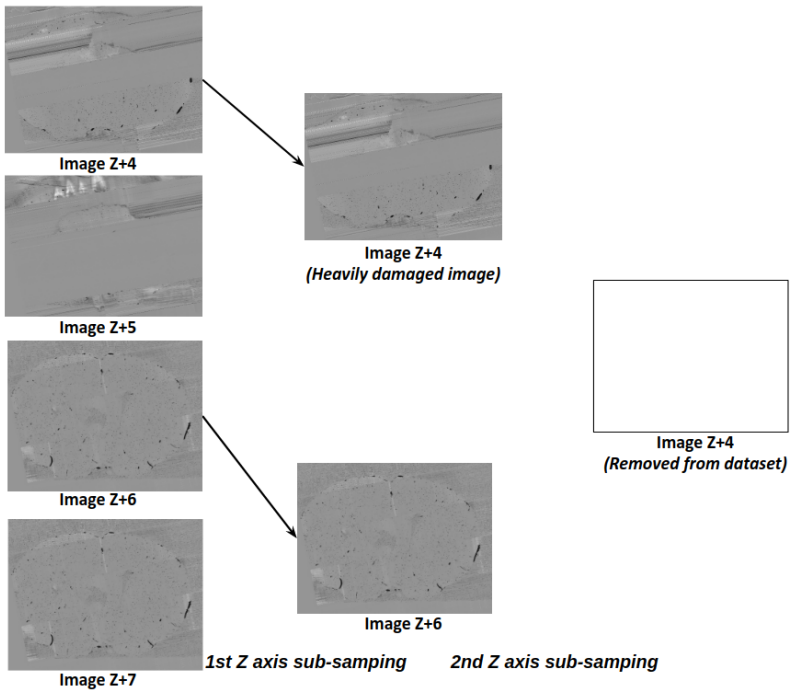

(b) Good and heavily damaged images

Figure 3.2: **Typical sub-sampling methods by z-axis.** (a) Four consecutive images (Image Z ~ Z+3) use only one image (Image Z) while going through two stages of sub-sampling by z-axis. (b) In addition, if the first image (Image Z+4)of four consecutive images (Image Z+4 ~ Z+7) is a heavily damaged image, it removed from the dataset while undergoing the two-step sub-sampling process by z-axis. Coronal view ($\uparrow$: $Dorsal$, $\downarrow$: $Ventral$).

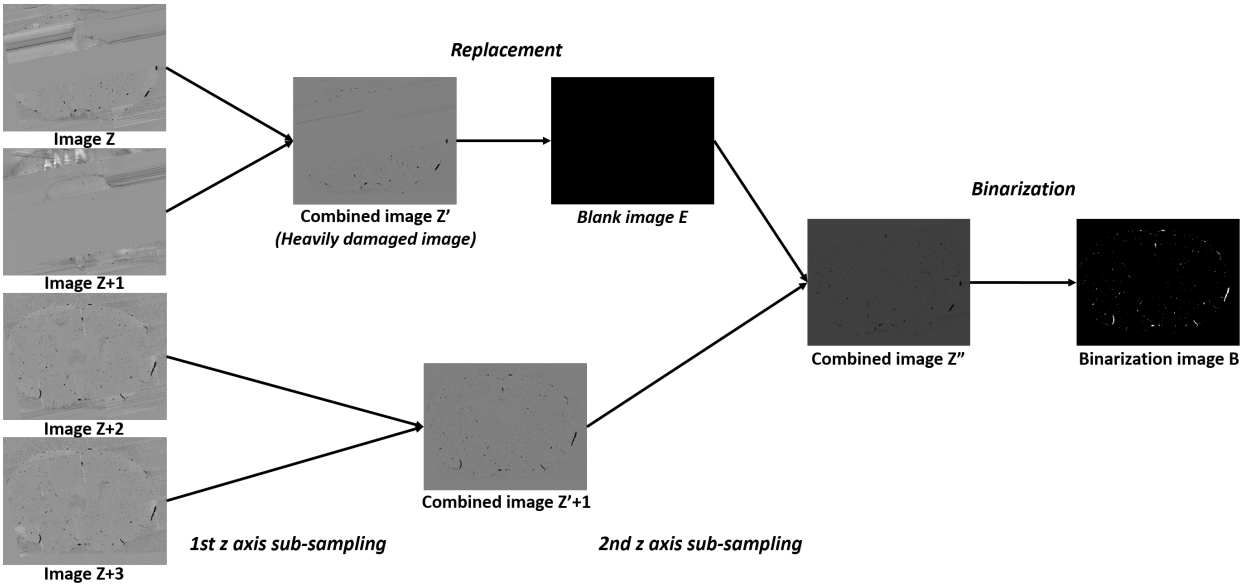

Figure 3.3: **Z axis sub-sampling and binarization process.** Z´ is the average of image Z and Z+1. E is a blank image for replacing damaged image. Z˝ is the average of E and Z´ +1. B is the thresholding result of Z˝. Coronal view ($\uparrow$: $Dorsal, \downarrow$: $Ventral$). Adapted from [47].

Image processing

The resulting dataset is about 1.5 TB per brain, which poses a significant challenge for computational analysis, especially when it comes to whole mouse brain analysis. Moreover, the dataset of the whole mouse brain include noise and irregularities owing to the serial sectioning process. [57]. The obtained coronal image slices were subjected to median filtering [34] to reduce the lighting defects (Figure 3.1a) and mechanical chatter (Figure 3.1b) left-over from the post-acquisition processing procedures. In order to analyze and visualize the huge volume data sets, sub-sampling methods have been commonly used for reducing the computational overhead.

Sub-sampling method

I propose a sub-sampling method (Figure 3.3) that combines two consecutive images to overcome the problems of the typical sub-sampling method (Figure 3.2) for the z-axis. I down-sampled the filtered image stack in the axial-direction by fifty percent. This was accomplished by averaging the consecutive image pairs. I then determined the heavily damaged image manually if it was

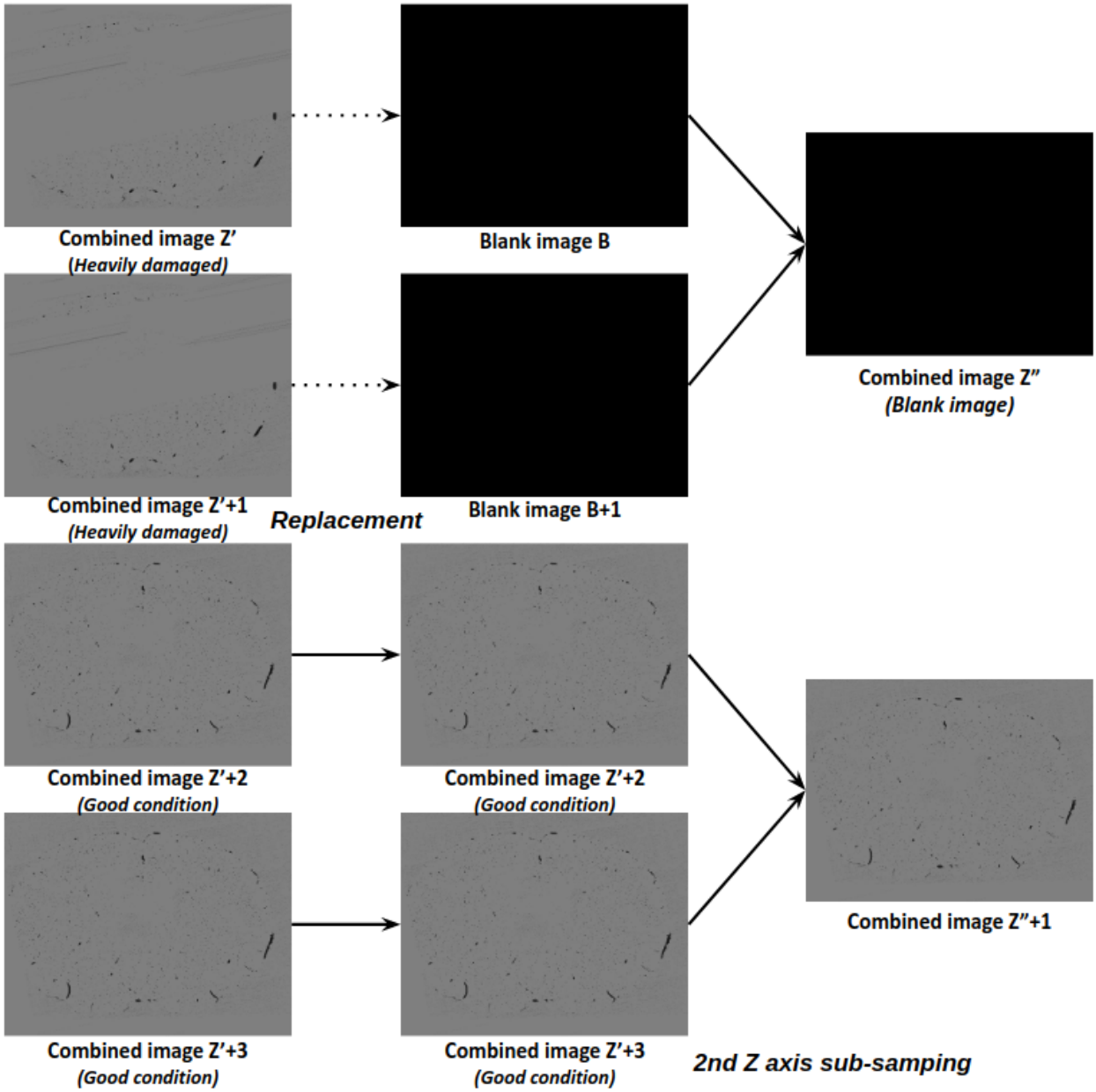

Figure 3.4: **The necessity of reordering.** After the first z-axis sub-sampling, if the heavily damaged images are located consecutively (Z´, Z´+1), the second z-axis subsampling causes the blank image to remain (Z´´) and cannot be included in the dataset.

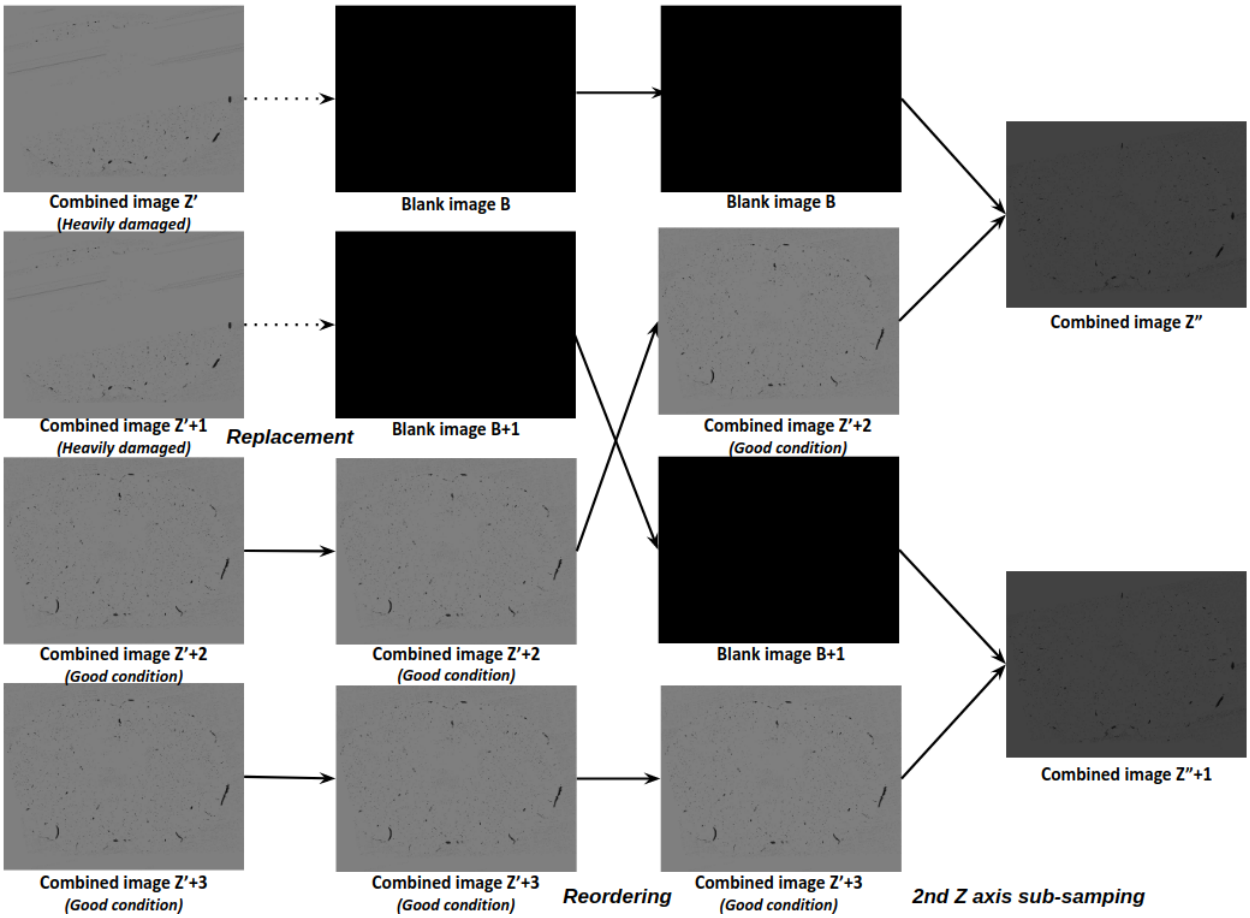

Figure 3.5: **Reordering of images.** After the first z-axis sub-sampling in Figure 3.5, if the heavily damaged images are located consecutively (Z´, Z´+1), a good condition image (Z´+2) is inserted between the blank images (B, B+1) such that the blank image is not continuous by applying the reordering technique.

found that many parts were physically missing as shown in Image Z and Image Z+1 in Figure 3.3, and replaced those with significant degradation with a blank image in order to maintain the depth throughout the axially. After the first z-axis sub-sampling in Figure 3.4, if the heavily damaged images are located consecutively (Z´, Z´+1), the second z-axis sub-sampling causes the blank image to remain (Z´´) and cannot be included in the dataset. Because of this problem, it is necessary to re-order the image sequence so that the blank images are not placed consecutively before proceeding with the second sub-sampling of the z-axis. After the first z-axis sub-sampling in Figure 3.5, if the heavily damaged images are located consecutively (Z´, Z´+1), a good condition image (Z´+2) is inserted between the blank images (B, B+1) such that the blank image is not continuous by applying the reordering technique. By rearranging the order of the images in this way (B, Z´+2, B+1, Z´+3 in Figure 3.5), it is possible to obtain an image preserving the information about the blood vessels such as Z´´ and Z´´+1 after the second z-axis sub-sampling and eliminate the distortion of the entire dataset size. After this second z-axis sub-sampling process, 2,140 consecutive coronal imaging slices are obtained.

Thresholding method

The thresholding method is the simplest method of image segmentation. The threshold value is used to make the image of the gray-scale level a binary image. A pixel having a value smaller than the threshold value is set to 0, and a pixel having a value equal to or larger than the threshold value is set to 1.

If $f(x, y)$ is a pixel, $g(x, y)$ is a threshold version of $f(x, y)$, and T is some global threshold [19],

$$g(x,y) = \begin{cases} 0 & f(x,y) < T \\ 1 & f(x,y) \geq T \end{cases} \tag{3.1}$$

There are many ways to determine the threshold T for image segmentation [25, 41]. As the vascular filaments embedded in the resultant images can be isolated by pixel intensity, I employed the global (histogram-derived) thresholding method [83] to the binarized dataset and applied the

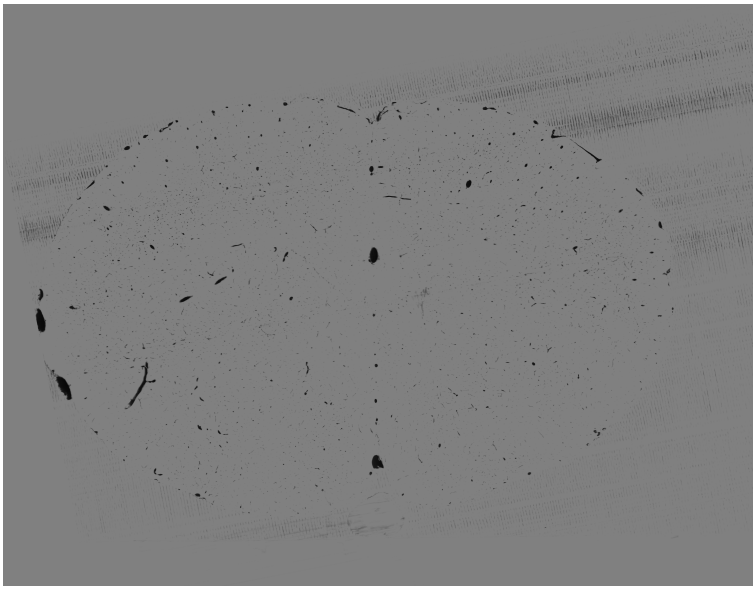

(a) An image sub-sampled twice along the z-axis.

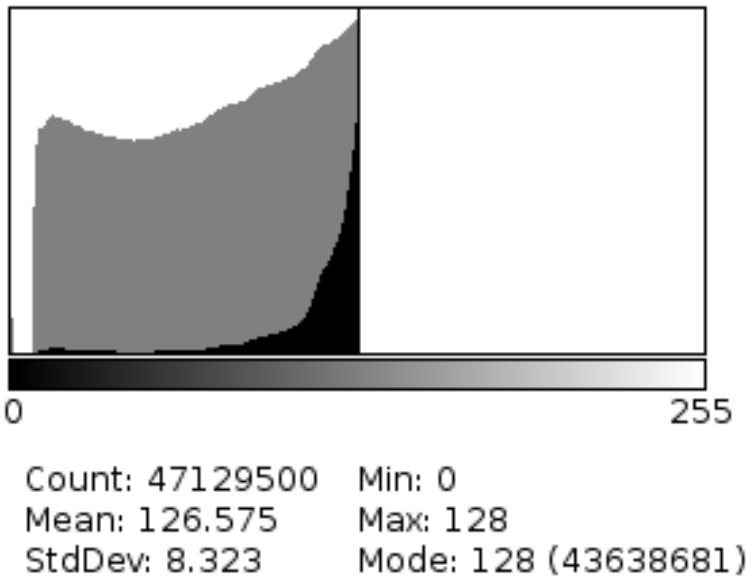

(b) Histogram of image (a)

Figure 3.6: **An image sub-sampled twice along the z-axis and its histogram.** (a) Image sub-sampled twice along the z-axis. (b) Histogram of the image (a). The x-axis is the gray-scale value (0 ~255) of the pixel and the y-axis is the number of pixels corresponding to the value. (The gray portion of the y-axis is the logarithmic scale). Adapted from [48].

minimum [74] and Otsu's [68] method of the threshold to the dataset to segment the vascular. Figure 3.6 shows an image sub-sampled twice in the z-axis and a histogram of Figure 3.6a. The minimum threshold method is to binarize the image by choosing T (Equation. 3.1, 0 ~255) as the lowest value of the y-axis between the two local maxima as shown in Figure 3.6b.

Equations 3.2 and 3.3 represent the formula of Otsu's threshold method. Otsu's threshold method chooses the T (Equation. 3.1, 0 ~255) to minimize the intraclass (within-class, Equation. 3.2) variance and to maximize the interclass (between-class, Equation. 3.3) variance of the two local maxima as shown in Figure 3.6b.

The probability of the two classes separated by the threshold T is $\omega_0(t)$ and $\omega_1(t)$ (weights), σ_0^2 and σ_1^2 are variances of the two classes, and μ is class means.

$$\sigma_w^2(T) = \omega_0(T)\sigma_0^2(T) + \omega_1(T)\sigma_1^2(T) \tag{3.2}$$

$$\begin{aligned} \sigma_b^2(T) &= \sigma^2 - \sigma_w^2(T) = \omega_0(\mu_0 - \mu_T)^2 + \omega_1(\mu_1 - \mu_T)^2 \\ &= \omega_0(T)\omega_1(T)\left[\mu_0(T) - \mu_1(T)\right]^2 \end{aligned} \tag{3.3}$$

Subsequently, I down-sampled the binarized images by twenty-five percent, laterally. As fragmentation amongst some of the embedded filaments occur during this process, I elected to resolve the matter through the application of morphological methods; I specifically employed morphological closing and hole filling operations successively across the stack [30]. I then proceeded with the extraction of the vascular filaments embedded in this processed image. By this point, I have attained the final voxel resolution to $4.8\,\mu\mathrm{m}$ laterally and $5.6\,\mu\mathrm{m}$ longitudinally by $4.0\,\mu\mathrm{m}$ axially. As a result of the image processing method, the raw image at 7790×6050 resolution was downsized to 1947×1512 resolution, and through the two step process of combining two consecutive images, 8,460 raw images were rebuilt into a $2,140$ dataset. Fig. 3.7 is an overflow of the image processing.

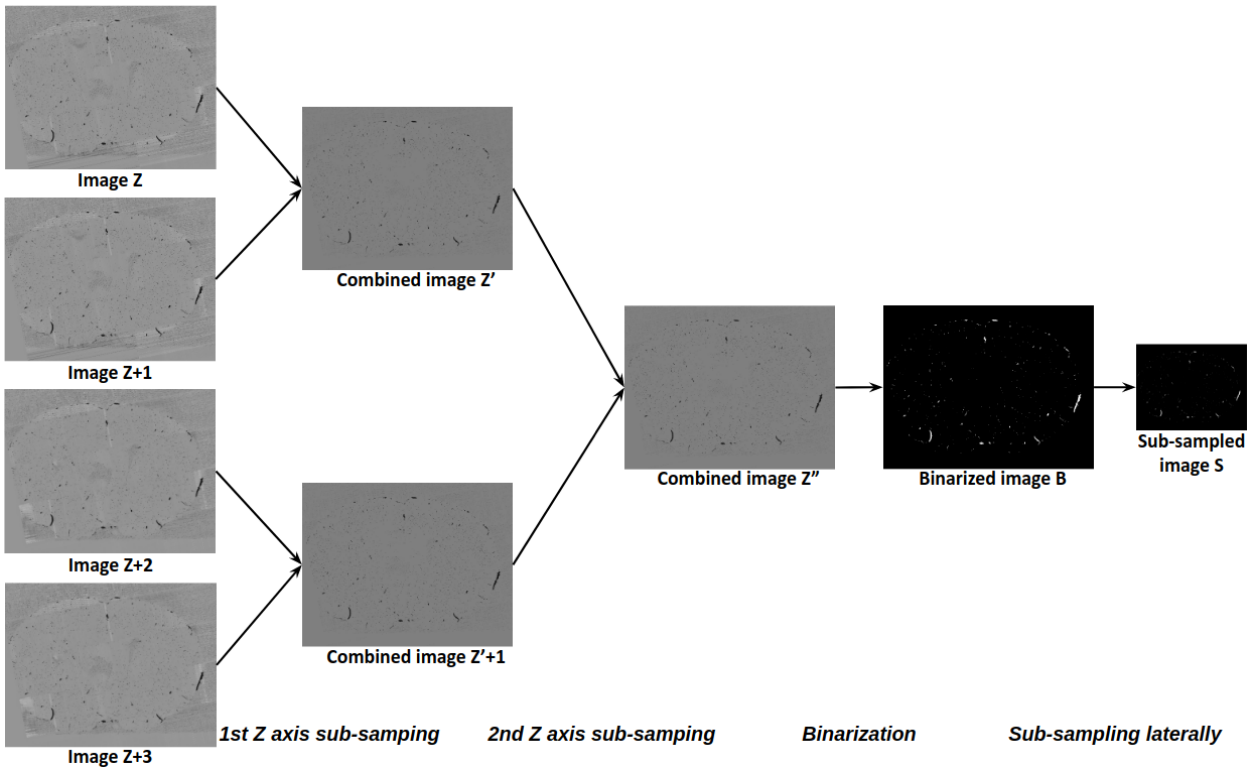

Figure 3.7: **An overview of the image processing steps.** Z´ is the average of image Z and Z+1. Z´´ is the average of Z´ and Z´+1. B is the thresholding result of Z´´. S is a result of sub-sampling laterally. As a result of the image processing methods, the raw image at 7790×6050 resolution was downsized to 1947×1512 resolution, and through the two step process of combining two consecutive images, $8,460$ raw images were rebuilt into a $2,140$ dataset. Coronal view ($\uparrow$: $Dorsal, \downarrow$: $Ventral$).

Convex hull method (Fully automated)

Motivation

The combined mouse brain image not only contains information about the vessels but also includes noise outside the brain. Noise, in this case, is in the form of comb stripes outside the brain as in Figure 3.6a. The noise also affects the amount of vascular information in the process of binarization imaging.

In order to segment only the brain part from the raw image (Figure 3.8a), An $et\ al.$ [6] described the region of interest (ROI) as the brain's inside area. They created a freehand mask (Figure 3.8b) that manually painted an ROI boundary to remove noise outside the brain. Then, they segmented the brain region by combining with 20 consecutive raw images per a freehand mask. This operation requires a lot of time and effort.

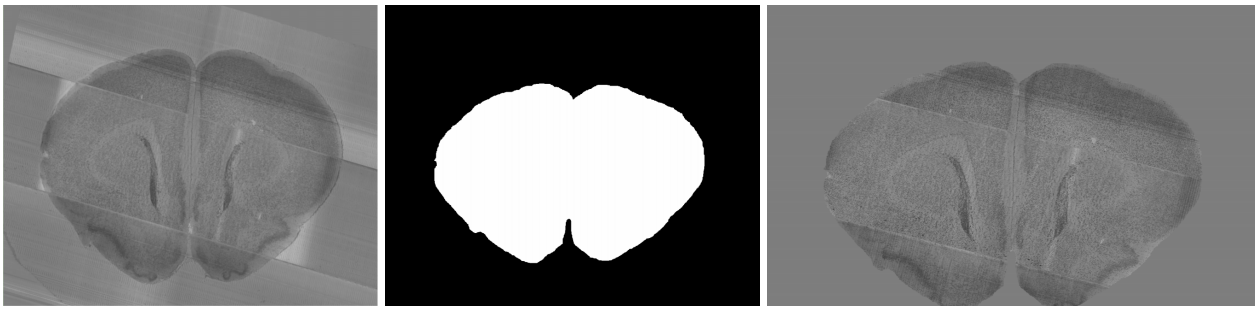

(a) Raw image (b) Freehand mask (c) Segmented image

Figure 3.8: **The region of interest (ROI) as the mouse brain's inside area with Nissl stained data.** (a) Raw image. (b) Freehand mask. (c) Segmented image after applying the freehand mask (b). A freehand mask manually painted an region of interest to remove noise outside the mouse brain. Adapted from [5].

Background

Convex Hull [20] is the smallest convex polygon that contains all points when given multiple points (Figure 3.9). In Figure 3.9b, when nine points from P1 to P9 are distributed, the convex

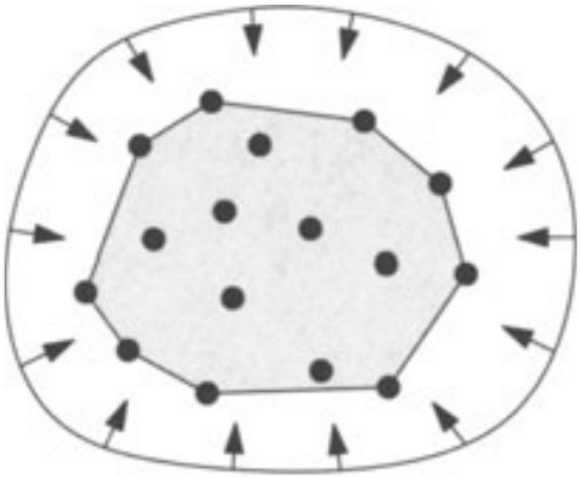

(a) Example of convex hull.

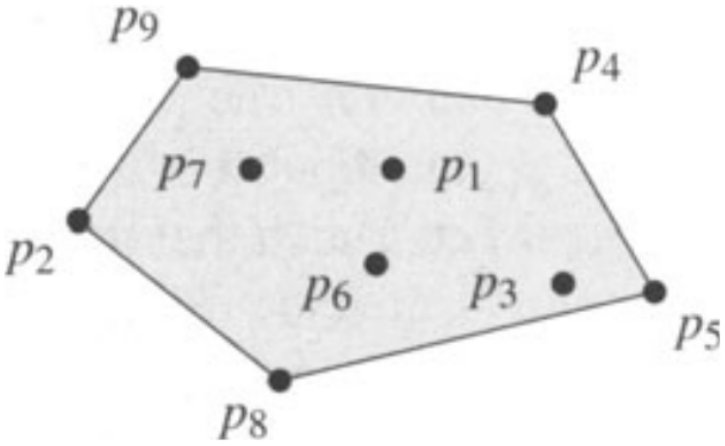

(b) Convex hull

Figure 3.9: **Convex hull method.** (a) Example of a convex hull. (b) Convex hull. When nine points from P1 to P9 are distributed, the convex hull is the minimum convex set ($P9, P2, P8, P5, P4$: polygon) containing all points. Adapted from [20].

hull is the minimum convex set ($P9, P2, P8, P5, P4$: polygon) containing all points. By using the convex hull method, ROI free mask as shown in Figure 3.8b can be created automatically.

Approach

Figure 3.10a is a combined mouse brain image (Z˝ in Figure 3.7). The image not only contains information about the vessels, but also includes noise in and outside the brain. In addition, this noise also affects the amount of vascular information in the process of binarization imaging (Figure 3.11a, 3.11b). As mentioned in section 3.2.2, I used the minimum threshold method and the Otsu's threshold method for image binarization. By applying the minimum method, the noise outside the brain can be removed, but information about blood vessels is also lost (Figure 3.11a). On the other hand, when the Otsu's threshold method is applied, as shown in Figure 3.11b, compared with Figure 3.11a, abundant information about the blood vessel can be obtained, but the noise outside the brain remains. Using an image obtained with the minimum method removes noise outside the brain, but loses information about small vessels.For this reason, I would like to use the image results obtained from the vascular information-rich, Otsu's threshold method to create a dataset. Using the method does not remove noise outside the brain, and making an accurate analysis of the cerebral vascular is impossible.

To solve this problem, I propose a method to automatically create a mask to remove noise outside the brain using the convex hull method. To apply the convex hull method, I used the image obtained from the minimum threshold method. This image does not provide enough information about the blood vessel, but it is detailed enough to get the shape of the brain contour. Figure 3.10d shows the resulting mask obtained by applying the convex hull method to Figure 3.10c. Combining the images with the convex hull mask (Figure 3.10d) and the Otsu's threshold method (Figure 3.10e) shows that the information about the blood vessel is abundant, as shown in Figure 3.12, and the noise outside the brain is removed.

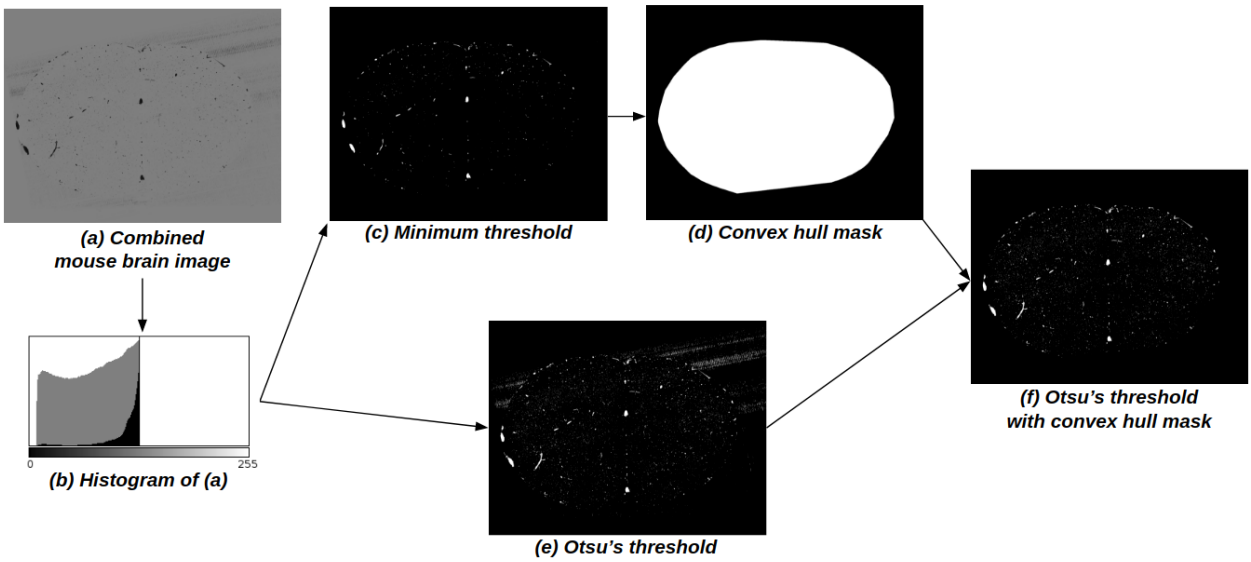

Figure 3.10: **Convex hull method (Fully automated).** (a) Combined mouse brain image. (b) Histogram of (a). The x-axis is the gray-scale value (0 ~255) of the pixel and the y-axis is the number of pixels corresponding to the value. (The gray portion of the y-axis is the logarithmic scale). (c) The result image of minimum threshold method. (d) Convex hull mask. (e) The result image of Otsu's threshold method. (f) The result image of Otsu's threshold method with convex hull mask. (e) showed increased blood vessel information compared to (b). Also, (e) was less noise than (d). I propose a convex hull masking method to automatically detect the boundary of the mouse brain and eliminate unnecessary information (including noise) outside of the region of interest(ROI). Coronal view ($\uparrow$: $Dorsal$, $\downarrow$: $Ventral$).

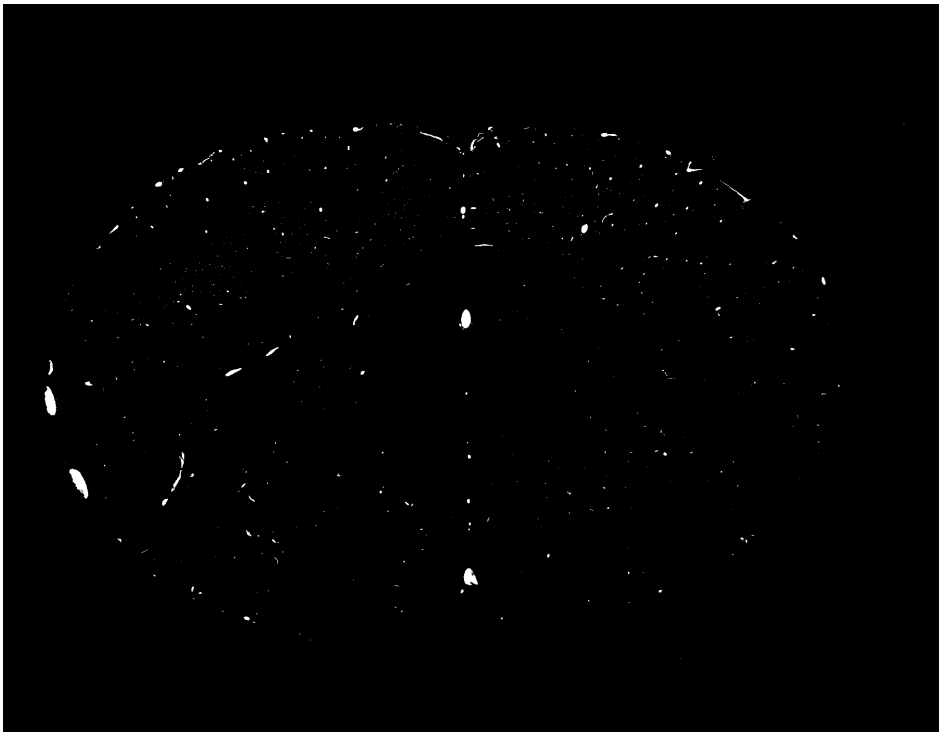

(a) The binarization result image of minimum threshold method

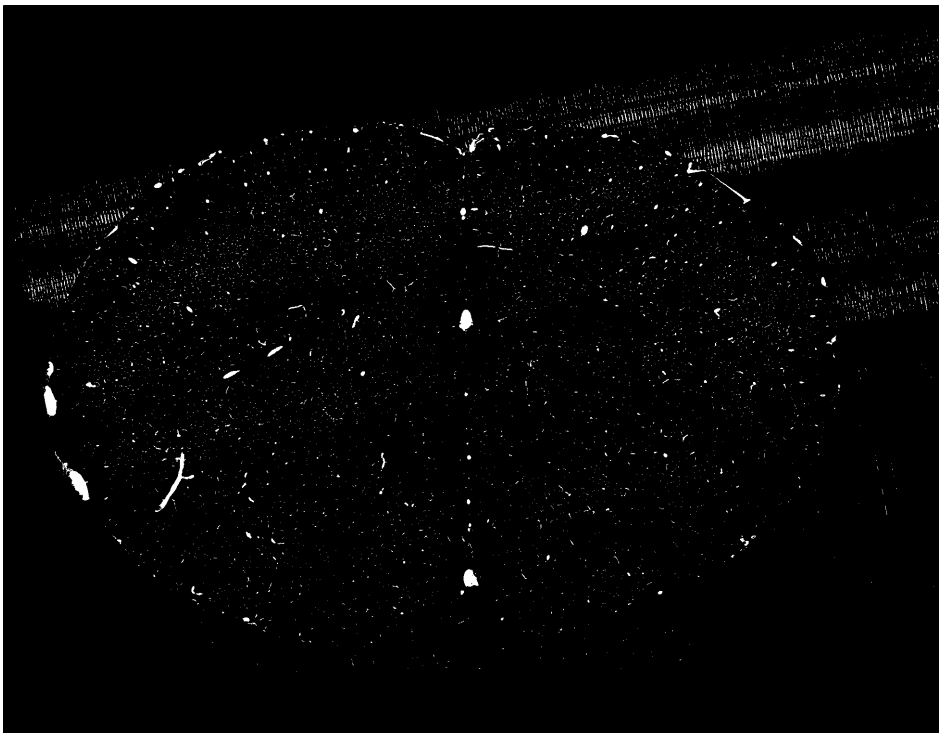

(b) The binarization result image of Otsu's threshold method

Figure 3.11: **The binarization result images.** (a) The binarization result image of minimum threshold method (b) The binarization result image of Otsu's threshold method. (a) and (b) are enlarged images of Figure 3.10c and 3.10e.

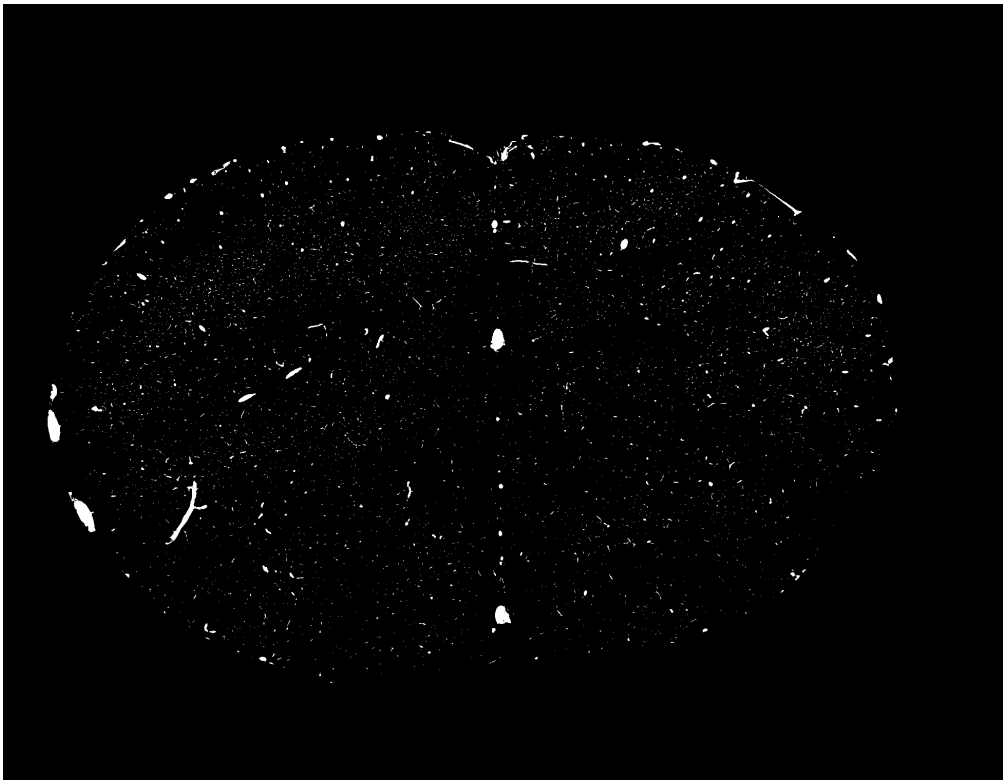

Figure 3.12: **Combining the image with the convex hull mask and the Otsu's threshold method.** This is an enlarged image of Figure 3.10f and shows that the information about the blood vessel is abundant, but the noise outside the brain is removed.

Results and analysis

I propose an axial direction sub-sampling method, where averaging consecutive image pairs and replacing significantly degraded images with a blank image are used. The resulting sub-sampled images are greatly reduced in size for visualizing and analyzing, but retain more information than sub-sampled images from other sub-sampling methods. In addition, I propose a convex hull masking method to automatically detect the boundary of the mouse brain and eliminate unnecessary information (including noise) outside of the region of interest(ROI). This method allows me to use a more aggressive threshold option, which results in more abundant vascular information.

Figure 3.12 is one of the proposed data images. Figure 3.13 and Figure 3.14 are 3D visualizations of the data set in different views, and it can see that the noise outside the brain has been removed. As a result of image processing and convex hull mask methods, the raw image at 7790×6050 resolution was downsized to 1947×1512 resolution, and through the two step process of combining two consecutive images, 8460 raw images were rebuilt into a 2140 dataset.

Summary

In this chapter, I described the process of preparing a whole mouse brain dataset for 3D reconstruction. In order to analyze a KESM dataset, a sub-sampling method to reduce the size of the data is needed. In order to overcome the limitations of the existing sub-sampling method, a method of combining successive images and replacing a heavy damaged image with a blank image has been applied. I also binarized the images using the minimum and Otsu's threshold methods, and created a convex hull mask that can remove noise outside the brain while obtaining an abundance of information about the blood vessels. The resulting KESM dataset is expected to be useful for analyzing the whole mouse brain microvasculature.

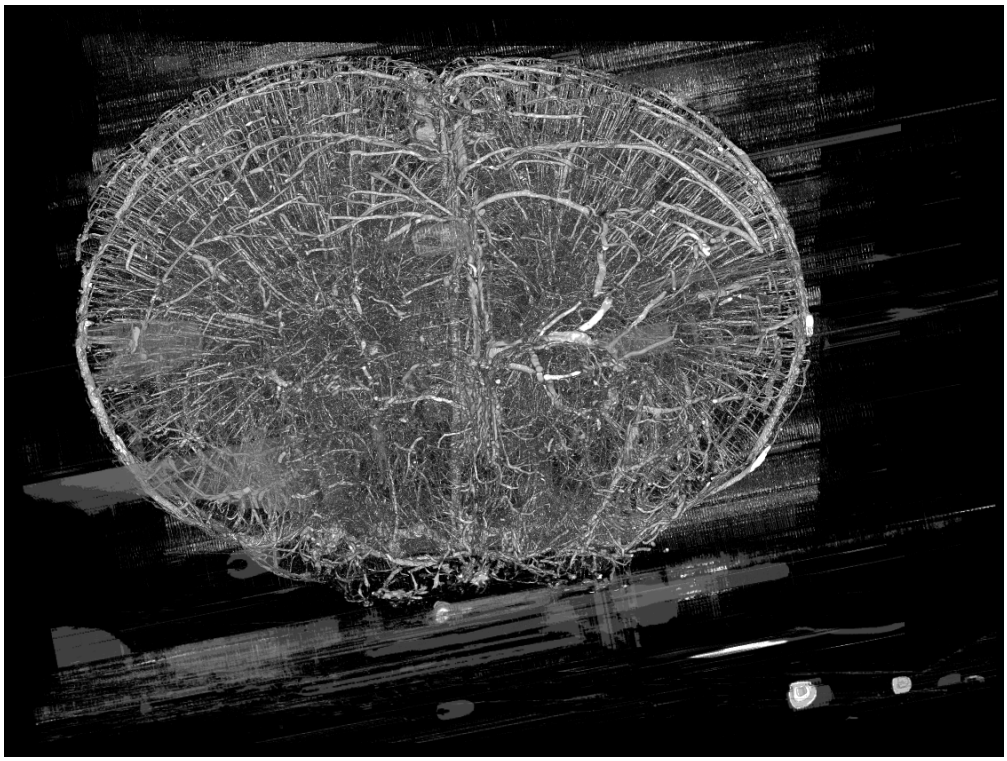

(a) Otsu's threshold method

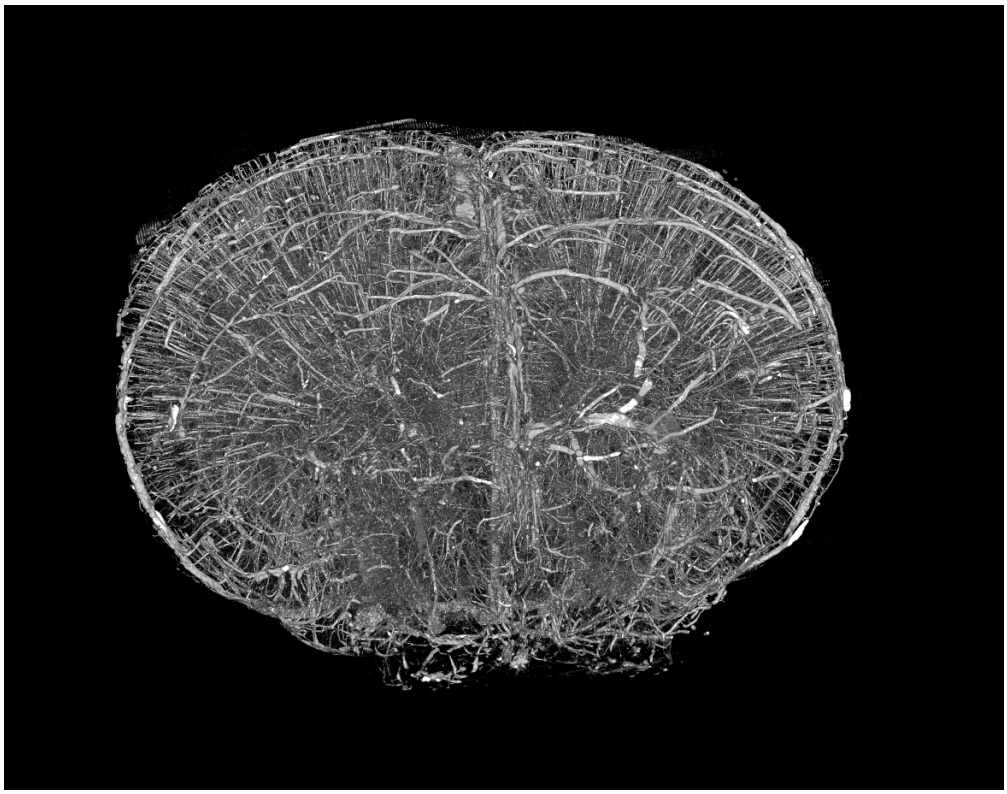

(b) Otsu's threshold method with convex hull mask

Figure 3.13: **3D visualization of dataset with coronal view.** ($\uparrow$: $Dorsal, \downarrow$: $Ventral$). Adapted from [48].

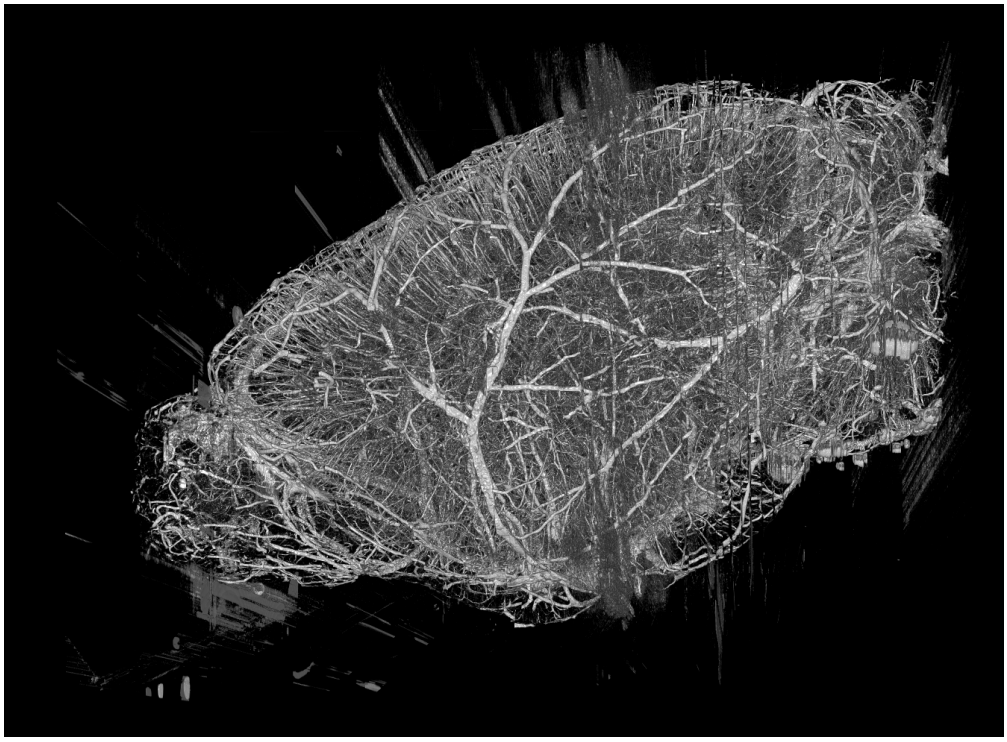

(a) Otsu's threshold method

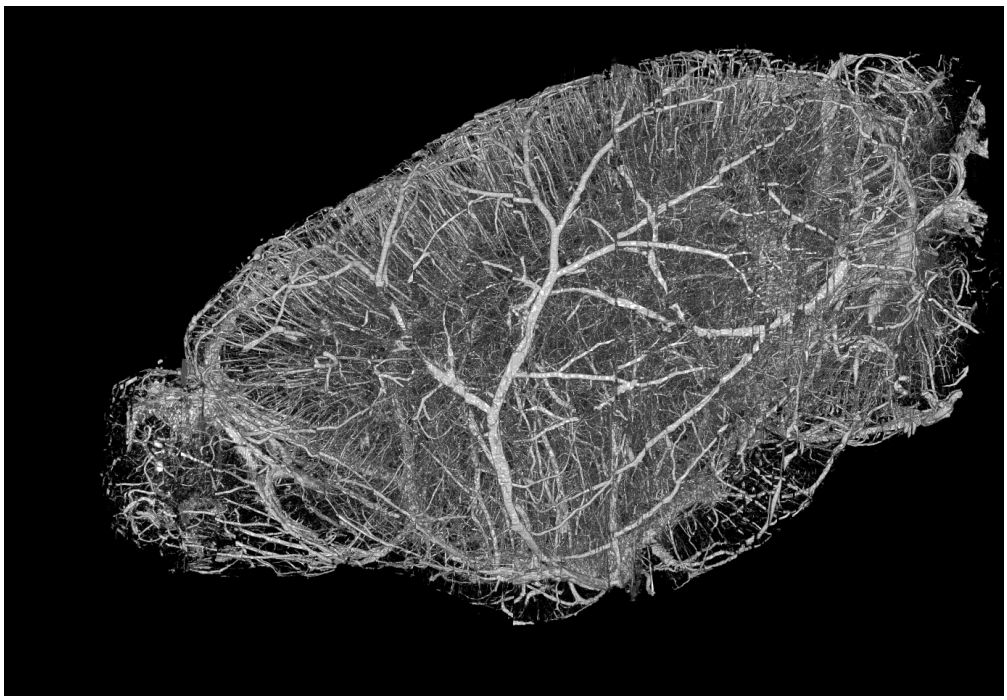

(b) Otsu's threshold method with convex hull mask

Figure 3.14: **3D visualization of dataset with sagittal view.** (←: Anterior, →: Posterior)

MEASURING AND CATEGORIZING BY THE VASCULAR DIAMETER

Motivation

In this chapter, I lay the foundation from which multiscale atlases characterizing cerebrovasculature structural variation comprised of the KESM dataset can be constructed from KESM datasets. Through the geometric reconstruction of the vascular filaments embedded in the volumetric imaging dataset, the capability to distinguish cerebral vessels based on diameter and other morphological properties across the whole-brain is provided. This results in a means to study local variations in small vessel morphometry, which has a profound effect on surrounding neuronal composition in different cerebral regions, as well as the robust and fragile aspects of the cerebrovasculature system across the larger vessels. Based on previous studies [8, 37, 54, 17, 61], blood vessels can be categorized as capillaries (diameter of $\leq 10\,\mu\mathrm{m}$), medium-sized vessels (diameter of 11 ~$20\,\mu\mathrm{m}$), or large-sized vessels (diameter of > $20\,\mu\mathrm{m}$). Xiong $et\ al.$ [96] classify the veins and arteries of the whole mouse brain as 3 levers with diameters size (diameter < $40\,\mu\mathrm{m}$, $40\,\mu\mathrm{m}$ < diameter < $90\,\mu\mathrm{m}$, diameter > $90\,\mu\mathrm{m}$).

Method

In order to analyze the structure of the blood vessels distributed in the mouse brain, according to the size of the blood vessel diameter, I refer to the previous studies [8, 37, 54, 17, 61, 96] and applied the blood vessel diameter to four criteria as shown in Table. 4.1.

Figure 4.1a is a sectioned image sub-sampled and binarized with Otsu's threshold method. After the application of these pre-processing steps, the size of each coronal slice is 1947×1512 pixels and the resolution is $4.8\,\mu\mathrm{m} \times 5.6\,\mu\mathrm{m}$. To calculate the diameter of the vessel, I took advantage of the features of finding the diameter of the image processing toolbox [31, 29] provided by MATLAB [77]. Then, four criteria were applied as shown in Table. 4.1, and the corresponding portions were extracted from the Figure 4.1 according to the diameter of the blood vessel to make Figure 4.1b $\sim$ e. After that, when the two vessel cross-sections are connected by a continuous slice

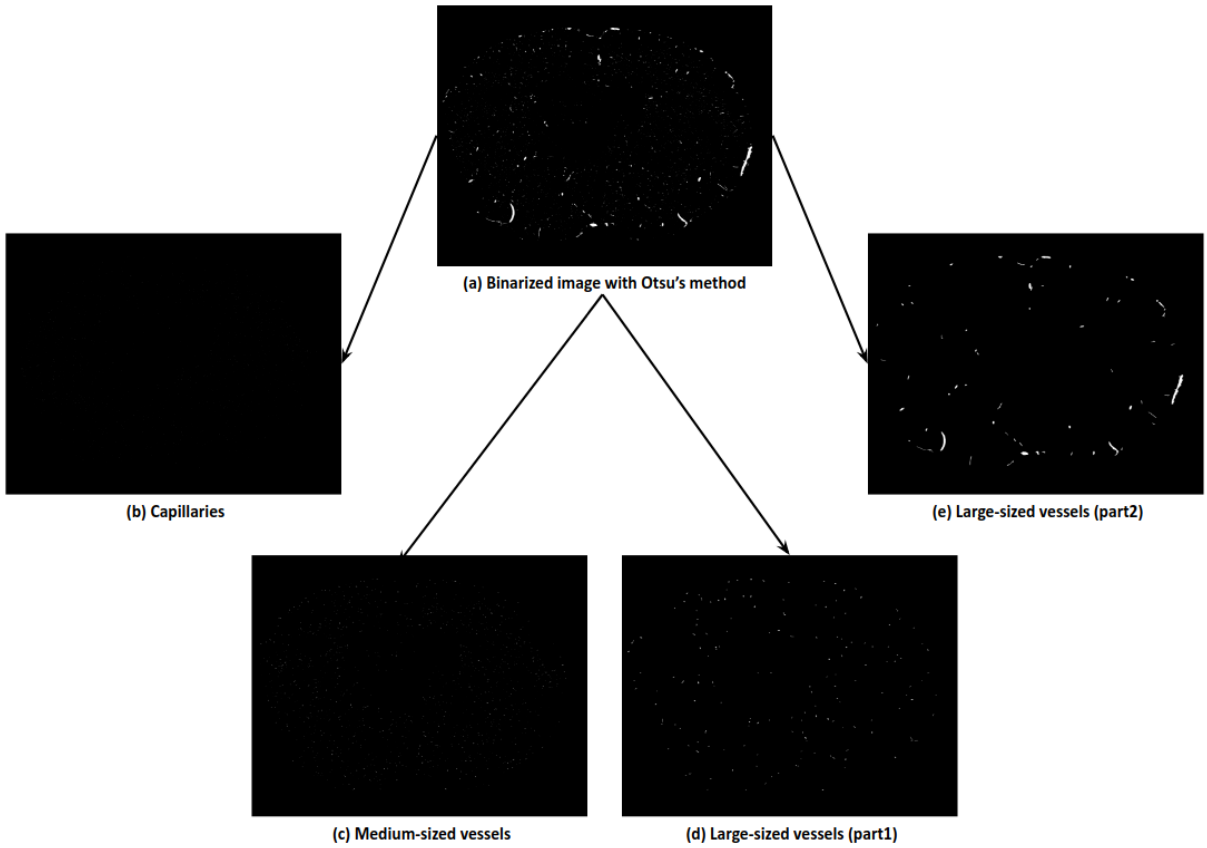

Figure 4.1: **Categorization of the vessel in the coronal imaging slice according to the diameter size.** After the application of these pre-processing steps, the size of each coronal slice is 1947×1512 pixels and the resolution is $4.8\,\mu\text{m} \times 5.6\,\mu\text{m}$. (a) Binarized image with Otsu's threshold method. It is classified into four groups depending on the size of the blood vessel diameter (b $\sim$ e). (b) Capillaries ($Diameter \leq 10.4 \pm 0.8\mu\text{m}$). (c) Medium-sized vessels ($10.4 \pm 0.8\mu\text{m} < Diameter \leq 20.8 \pm 1.6\mu\text{m}$). (d) Large-sized vessels (part1) ($20.8 \pm 1.6\mu\text{m} < Diameter \leq 41.6 \pm 3.2\mu\text{m}$). (e) Large-sized vessels (part2) ($Diameter > 41.6 \pm 3.2\mu\text{m}$).

Table 4.1: Four criteria of the blood vessel diameter (D).

Classification	The size of the vessel	Actual size range*
$Capillaries$	$D \leq 10\,\mu m$	$D \leq 10.4 \pm 0.8\,\mu m$
$Medium-sized\ vessels$	$11\,\mu m < D \leq 20\,\mu m$	$10.4 \pm 0.8\,\mu m < D \leq 20.8 \pm 1.6 \mu m$
$Large-sized\ vessels\ (part1)$	$21\,\mu m < D \leq 40\,\mu m$	$20.8 \pm 1.6\,\mu m < D \leq 41.6 \pm 3.2 \mu m$
$Large-sized\ vessels\ (part2)$	$D > 40\,\mu m$	$D > 41.6 \pm 3.2\,\mu m$

*Actual size range: Original resolution $(4.8\,\mu m \times 5.6\,\mu m)$ applied $(4.8\,\mu m\ or\ 5.6\,\mu m\ per\ 1\ pixel)$.

along the z-axis, they connect the center point of the vessel [50] and leave relevant information in Visualization Toolkit (VTK) file format [82]. As a result, I get four categorized vessel tracing results (Four VTK files). I also traced the vessels using the KESM dataset that used the minimum threshold method in the same way.

Results and analysis

I qualitatively illustrate the distribution of vascular filaments by diameter size and they are visualized by different colors for different diameter ranges (Figure 4.2). Across the whole-brain of the C57BL/6J mouse model, the rendering of the full-scale cerebrovasculature system are shown from the transverse plane (Figure 4.3), coronal (Figure 4.4a) and sagittal (Figure 4.4b) views. As shown in Figure 4.2, I categorized blood vessels from capillaries ($Diameter \leq 10.4 \pm 0.8\mu m$) in blue, medium-sized vessels ($10.4 \pm 0.8\mu m < Diameter \leq 20.8 \pm 1.6\mu m$) in black, large-sized vessels (part1) ($20.8 \pm 1.6\mu m < Diameter \leq 41.6 \pm 3.2\mu m$) in green, and large-sized vessels (part2) ($Diameter > 41.6 \pm 3.2\mu m$) in red.

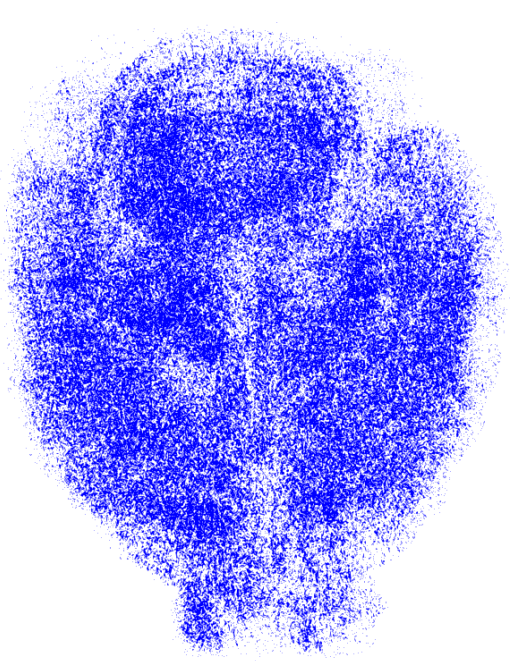

(a) Capillaries

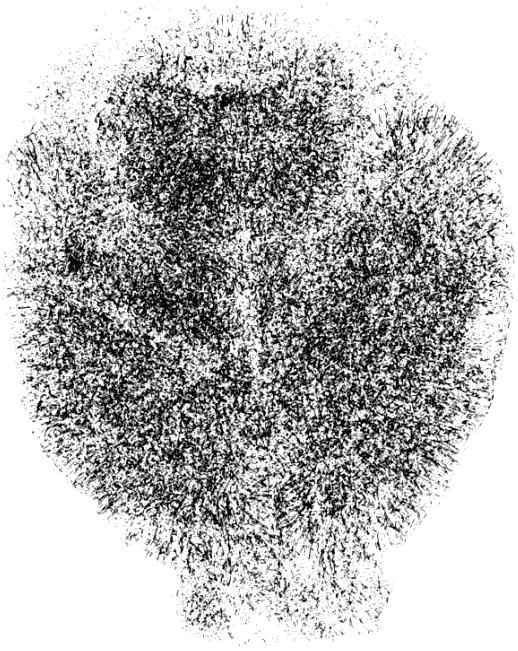

(b) Medium-sized vessels

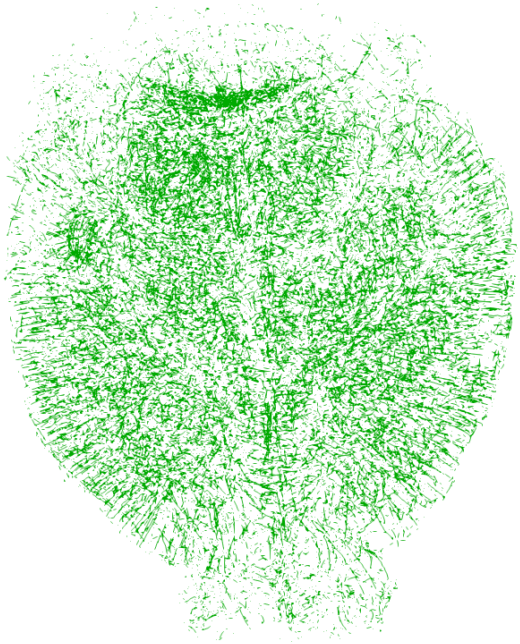

(c) Large-sized vessels (part1)

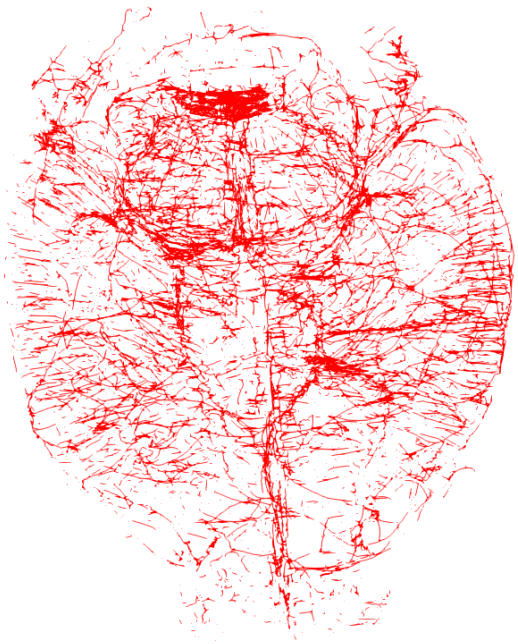

(d) Large-sized vessels (part2)

Figure 4.2: **Categorized vessels according to diameter size (Otsu's threshold method).** (a) Capillaries ($Diameter \leq 10.4 \pm 0.8\mu m$). (b) Medium-sized vessels ($10.4 \pm 0.8\mu m < D \leq 20.8 \pm 1.6\mu m$). (c) Large-sized vessels (part1) ($20.8 \pm 1.6\mu m < D \leq 41.6 \pm 3.2\mu m$). (d) Large-sized vessels (part2) ($D > 41.6 \pm 3.2\mu m$).

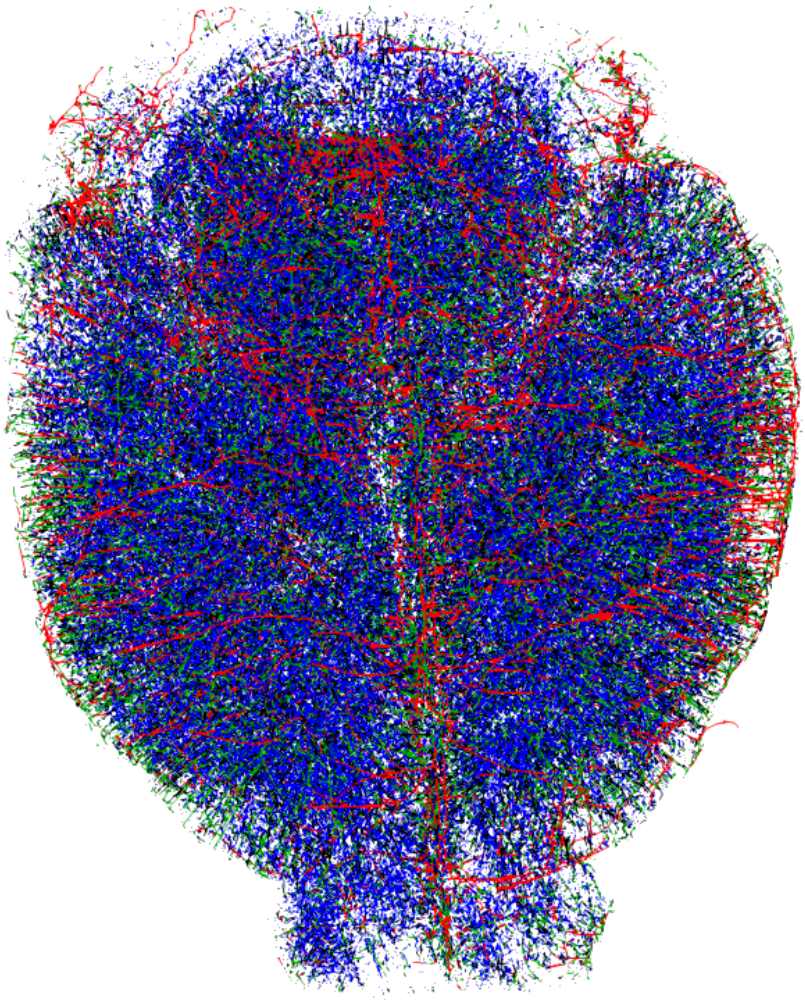

Figure 4.3: **Distribution of vessels according to diameter size over the whole mouse brain (Otsu's threshold method).** I categorized blood vessels from capillaries ($Diameter \leq 10.4 \pm 0.8\mu m$) in blue, medium-sized vessels ($10.4 \pm 0.8\mu m < Diameter \leq 20.8 \pm 1.6\mu m$) in black, large-sized vessels (part1) ($20.8 \pm 1.6\mu m < Diameter \leq 41.6 \pm 3.2\mu m$) in green, and large-sized vessels (part2) ($Diameter > 41.6 \pm 3.2\mu m$) in red. Transverse plane ($\uparrow$: Posterior, $\downarrow$: Anterior)

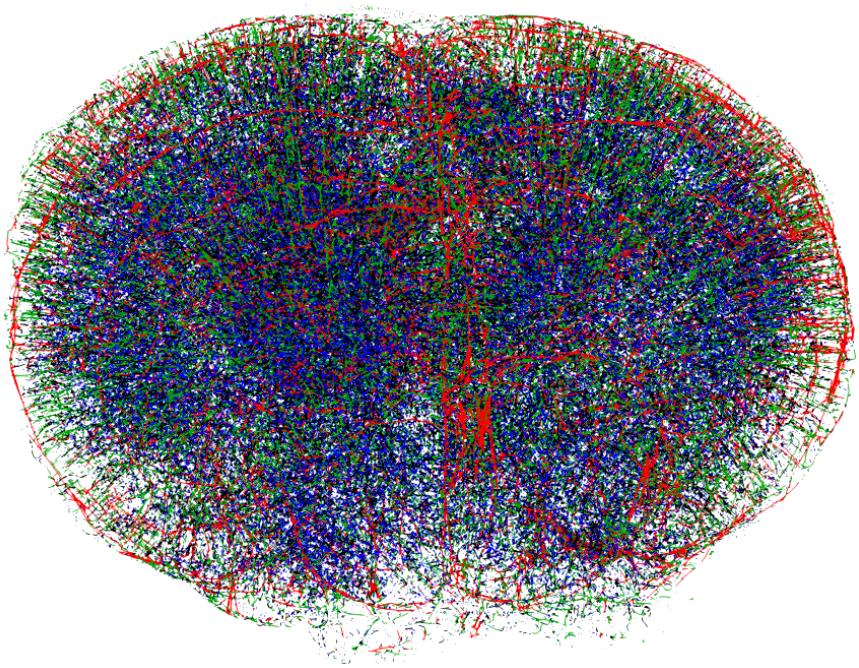

(a) Coronal view (↑: Dorsal, ↓: Ventral)

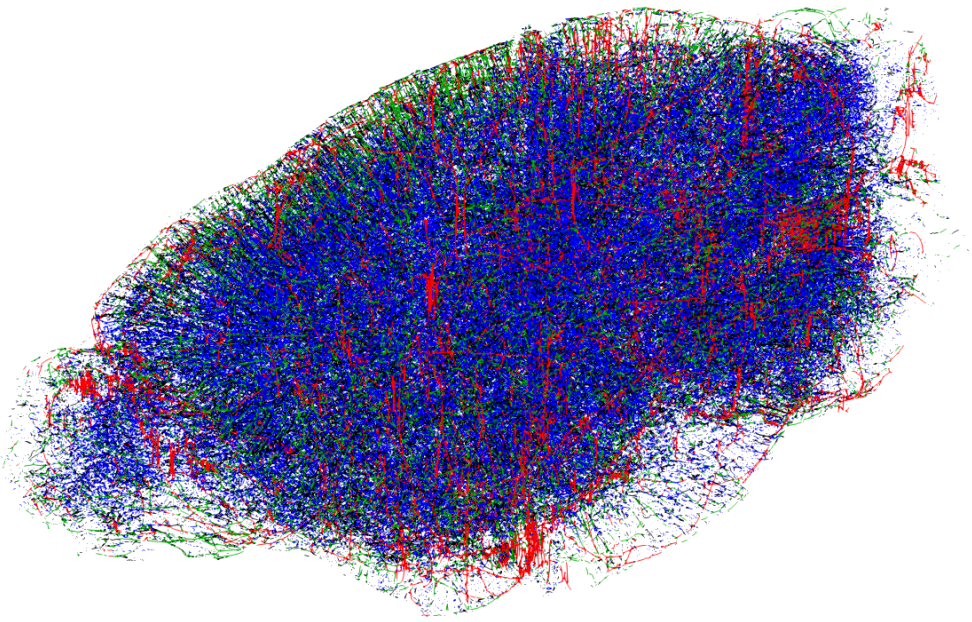

(b) Sagittal view (←: Anterior, →: Posterior)

Figure 4.4: **Distribution according to vessel diameter size with different views (Otsu's threshold method).** I categorized blood vessels from capillaries ($Diameter \leq 10.4 \pm 0.8\mu m$) in blue, medium-sized vessels ($10.4 \pm 0.8\mu m < Diameter \leq 20.8 \pm 1.6\mu m$) in black, large-sized vessels (part1) ($20.8 \pm 1.6\mu m < Diameter \leq 41.6 \pm 3.2\mu m$) in green, and large-sized vessels (part2) ($Diameter > 41.6 \pm 3.2\mu m$) in red.

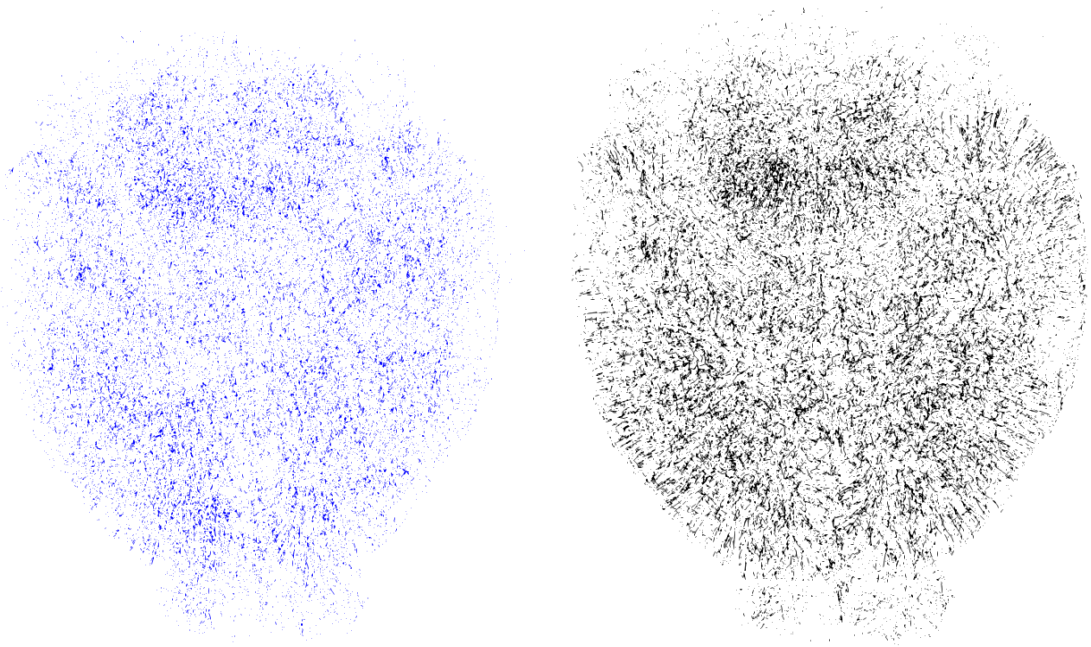

(a) Capillaries

(b) Medium-sized vessels

(c) large-sized vessels (part1)

(d) large-sized vessels (part2)

Figure 4.5: **Categorized vessels according to diameter size (Minimum threshold method).** (a) Capillaries ($Diameter \leq 10.4 \pm 0.8\mu m$). (b) Medium-sized vessels ($10.4 \pm 0.8\mu m < D \leq 20.8 \pm 1.6\mu m$). (c) large-sized vessels (part1) ($20.8 \pm 1.6\mu m < D \leq 41.6 \pm 3.2\mu m$). (d) large-sized vessels (part2) ($D > 41.6 \pm 3.2\mu m$).

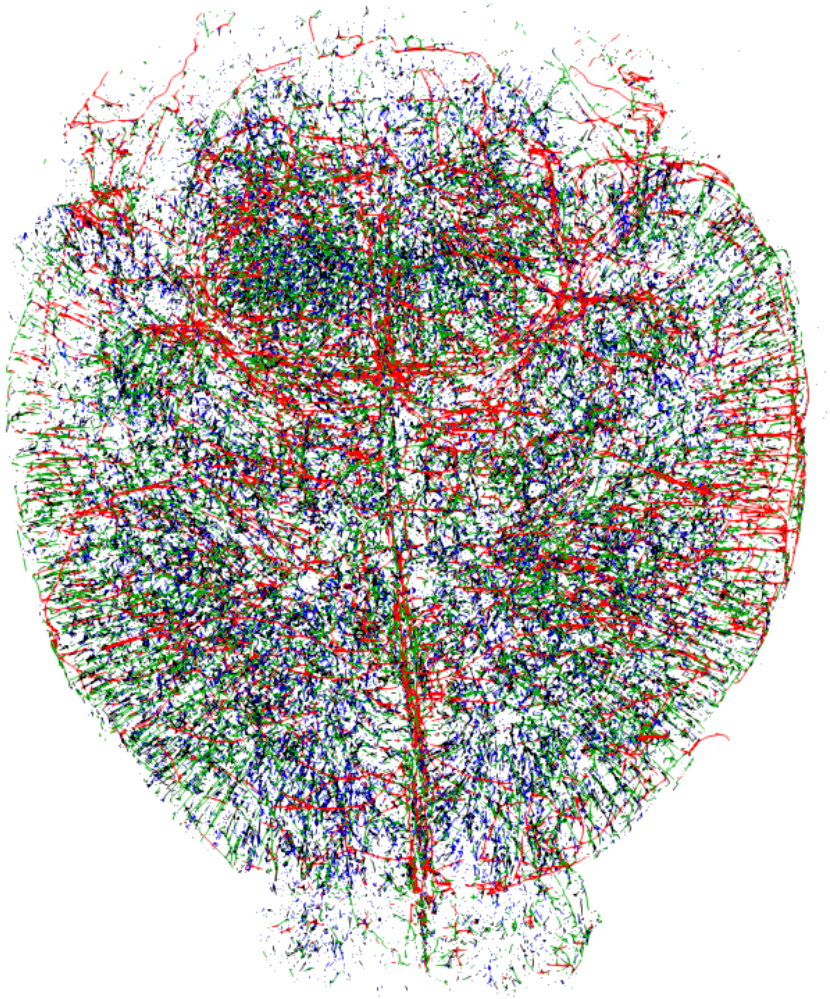

Figure 4.6: **Distribution of vessels according to diameter size over the whole mouse brain (Minimum threshold method).** I categorized blood vessels from capillaries ($Diameter \leq 10.4 \pm 0.8\mu m$) in blue, medium-sized vessels ($10.4 \pm 0.8\mu m < Diameter \leq 20.8 \pm 1.6\mu m$) in black, large-sized vessels (part1) ($20.8 \pm 1.6\mu m < Diameter \leq 41.6 \pm 3.2\mu m$) in green, and large-sized vessels (part2) ($Diameter > 41.6 \pm 3.2\mu m$) in red. Transverse plane ($\uparrow$: Posterior, $\downarrow$: Anterior)

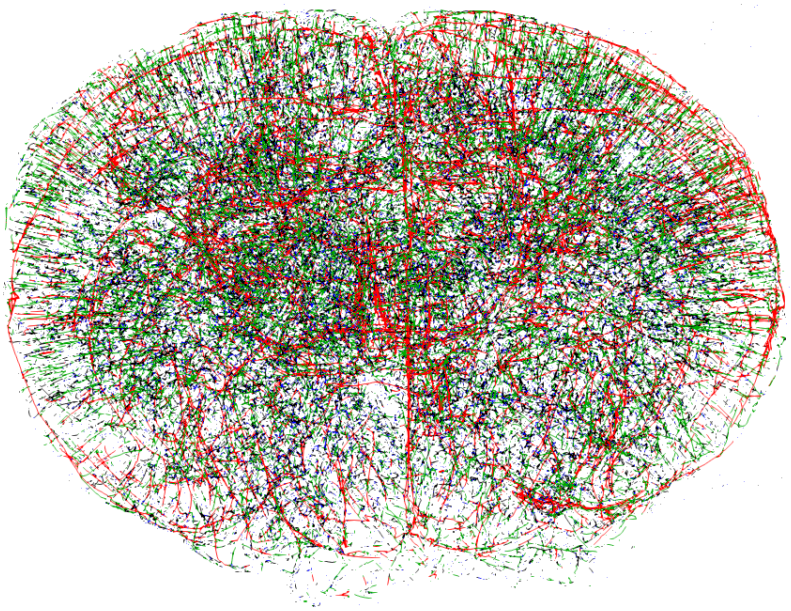

(a) Coronal view (↑: Dorsal, ↓: Ventral)

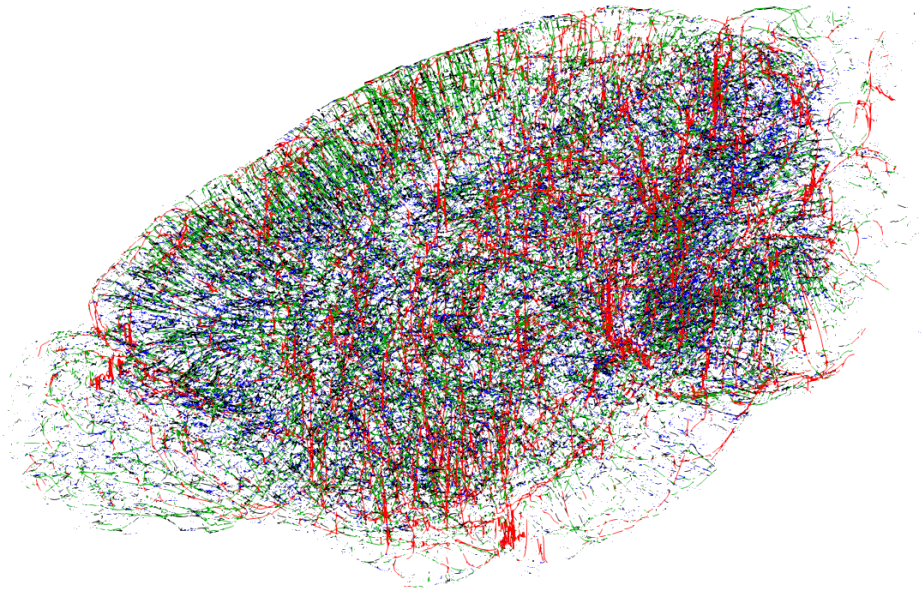

(b) Sagittal view (←: Anterior, →: Posterior)

Figure 4.7: **Distribution according to vessel diameter size with different views (Minimum threshold method).** I categorized blood vessels from capillaries ($Diameter \leq 10.4 \pm 0.8\mu m$) in blue, medium-sized vessels ($10.4 \pm 0.8\mu m < Diameter \leq 20.8 \pm 1.6\mu m$) in black, large-sized vessels (part1) ($20.8 \pm 1.6\mu m < Diameter \leq 41.6 \pm 3.2\mu m$) in green, and large-sized vessels (part2) ($Diameter > 41.6 \pm 3.2\mu m$) in red.

I used the ParaView (Data analysis and visualization software.) application [7] to visualize the structure of the blood vessels by running the VTK files. From the transverse plane (Figure 4.3), the cerebral vessels comprising the Circle of Willis [28] are clearly visible, as are the penetrating vessels that serve as the bottleneck to cortical blood flow. The variability of filament size across the cortical hemispheres is clear as I travel laterally from the midline towards the pial surface; vessel size variations are also apparent from coronal (Figure 4.4a) and sagittal (Figure 4.4b) viewpoint. I obtained the tracing results shown in Figure 4.5, Figure 4.6, and Figure 4.7 using the KESM dataset of minimum threshold method in the same way.

Summary

In this chapter, I presented data illustrating how KESM-acquired datasets provide the means to study cerebrovasculature variation across the whole-brains of small animal models. This results can also be used in studies to compare normal healthy brains and brains damaged by disease.

Figure 4.8a shows the vascular structure of a healthy mouse brain. The whole blood vessel is connected well, including the part of the white arrows. On the other hand, Figure 4.8b shows the vascular structure of an ischemic mouse brain, and there are considerable parts of the blood vessel that are incomplete, including the part with an asterisk (*) and white arrows. As a result, we can obtain the characteristics of each brain by analyzing normal brains and diseased brains as shown in Figure 4.9. Figure 4.9a shows the total vascular length density and shows that the non-ischemic brain has a higher density value than the ischemic brain. Figure 4.9b shows the vasculature length stratified by vascular diameter. When the diameter of blood vessels is less than $20\,\mu\mathrm{m}$, the density of non-ischemic brain is larger than an ischemic brain. In particular, it can be seen that the difference in the results is considerably large when the diameter of the blood vessel is less than $10\,\mu\mathrm{m}$ (capillaries) [52].

Therefore, I expect that this foundation will prove invaluable towards data-driven, quantitative investigations into the system-level architectural layout of the cerebrovasculature and surrounding cerebral microstructures.

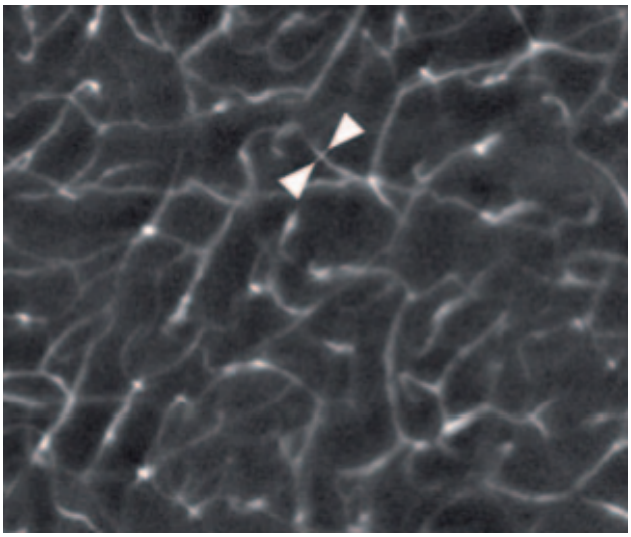

(a) A healthy mouse brain

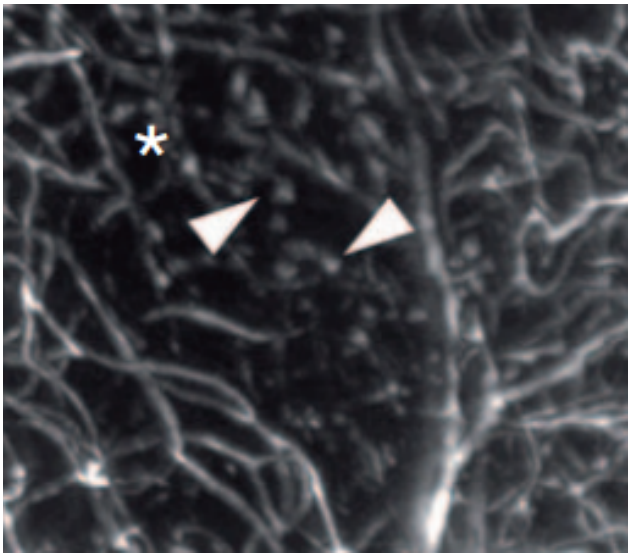

(b) An ischemic mouse brain

Figure 4.8: **Vascular architecture of a healthy and an ischemic mouse brain.** (a) shows the vascular structure of a healthy mouse brain. The whole blood vessel is connected well, including the part shown by the white arrows. (b) shows the vascular structure of an ischemic mouse brain, and there are considerable parts of the blood vessel that are incomplete, including the part indicated by an asterisk (*) and white arrows. Adapted from [52].

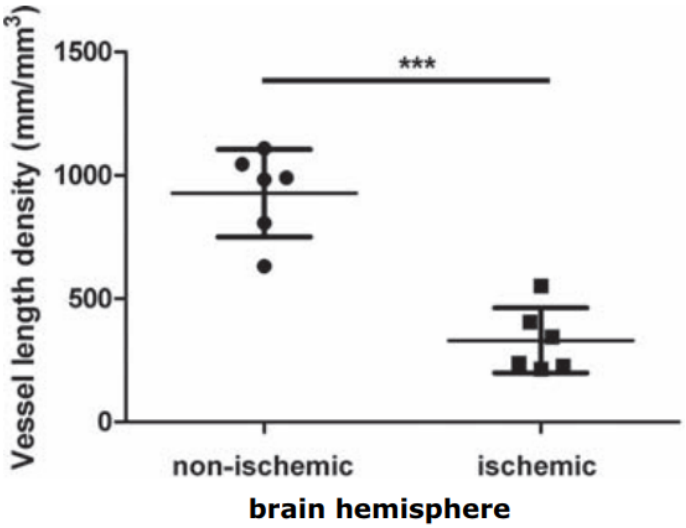

(a) Total vasculature length density

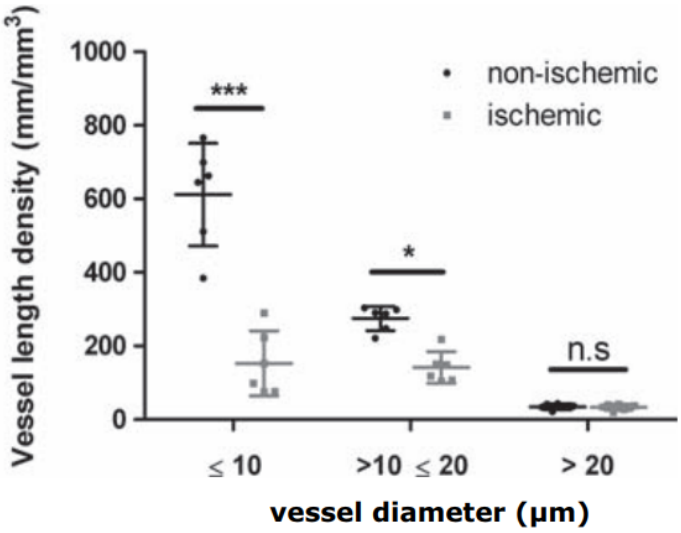

(b) The vasculature length density stratified by vascular diameter

Figure 4.9: **Comparison of vessel length density in a healthy and an ischemic mouse brain.** (a) shows the total vascular length density and shows that the non-ischemic brain has a higher density value than the ischemic brain. (b) shows the vasculature length stratified by vascular diameter. When the diameter of blood vessels is less than $20\,\mu\mathrm{m}$, the density of the non-ischemic brain is larger than of an ischemic brain. In particular, it can be seen that the difference in the results is considerably large when the diameter of the blood vessel is less than $10\,\mu\mathrm{m}$ (capillaries). Adapted from [52].

3D TRACING AND GEOMETRY ANALYSIS

The stacked image obtained through KESM was made into a dataset through Chapter. 3. In this Chapter, I describe the 3D reconstruction, tracing, and analysis of the vascular structure of the whole mouse brain using the KESM dataset. Figure 5.1 shows the whole process of obtaining a dataset using KESM and reconstructing it using the obtained KESM dataset. M is a ground truth, V is a 3D volume, I is a Image stack, $\hat{\mathrm{V}}$ is an estimated data volume, and $\hat{\mathrm{M}}$ is an estimated 3D reconstruction.

3D reconstruction of the vasculature

After creating a whole mouse brain dataset (Section. 3), I proceeded with 3D reconstruction using the resultant images for geometric analysis and visualization of the whole mouse brain microvascular structure. Using the 3D viewer plug-in [80], which is basically provided by ImageJ Software [25], it is possible to visualize the binarized 2D KESM dataset into 3D reconstruction. It can stack 2D images and view them in 3D, view the whole mouse brain structure from various directions, and also includes a zoom function. At this time, the voxel size of the KESM dataset used is $1947 \times 1512 \times 2140$ pixels and the resolution is $4.8\,\mu\mathrm{m} \times 5.6\,\mu\mathrm{m} \times 4.0\,\mu\mathrm{m}$.

Tracing the vasculature

After 3D reconstruction of the vasculature, I traced the 3D microvascular network using morphological analysis. Vaa3D (3D Visualization-Assisted Analysis) software [71] supports visualization and analysis of microvascular features depending on voxel resolution. In order to trace the vascular structure, I used the MOST tracing plugin [94] provided by Vaa3D, that implements the

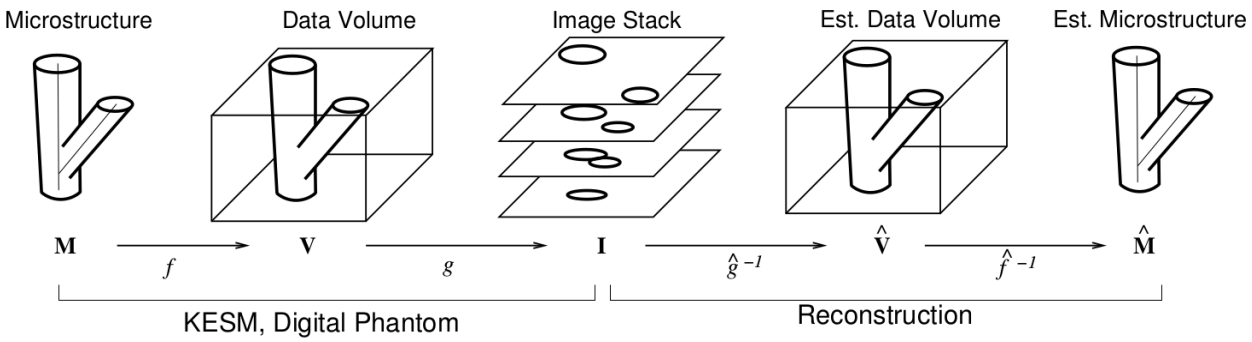

Figure 5.1: **Overview of reconstruction.** Ground truth of microstructure (M), Data volume (V), Image stack (I), Estimated data volume ($\hat{V}$), Estimated 3D reconstruction ($\hat{M}$). $\hat{g}$-1 is an estimated composition of the segmentation. $\hat{f}$-1 is the estimated 3D reconstruction process. Adapted from [12, 13]

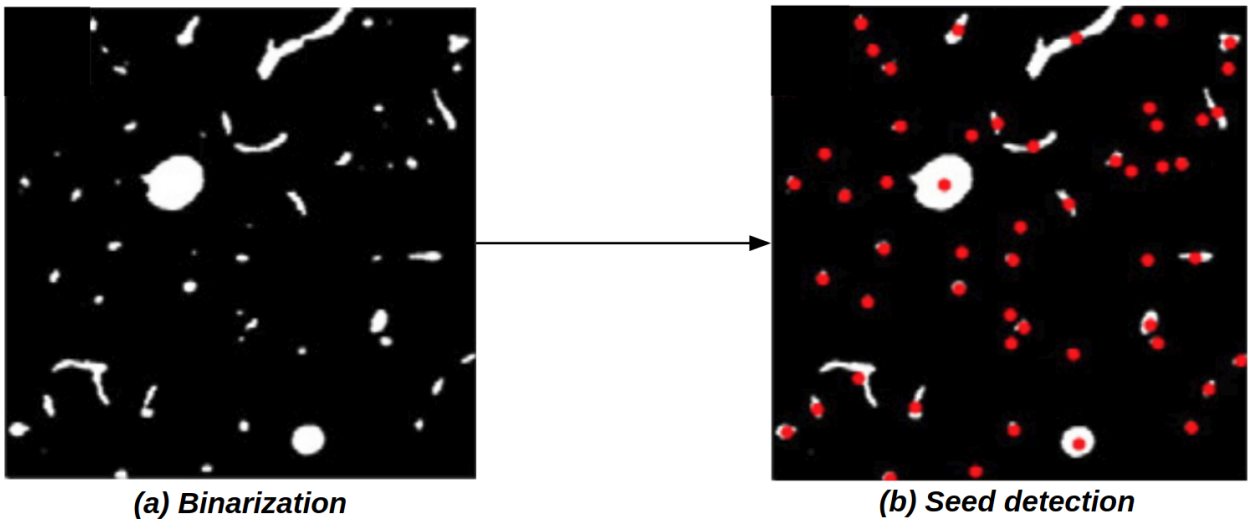

Figure 5.2: **Seed detection in blood vessel.** (a) Binarized image. (b) The result of seed detection. It shows the result of detecting the seed in the binarized image. The centroids of connected areas (white parts) in a 2D binarized image were seeds (red points). Adapted from [94]

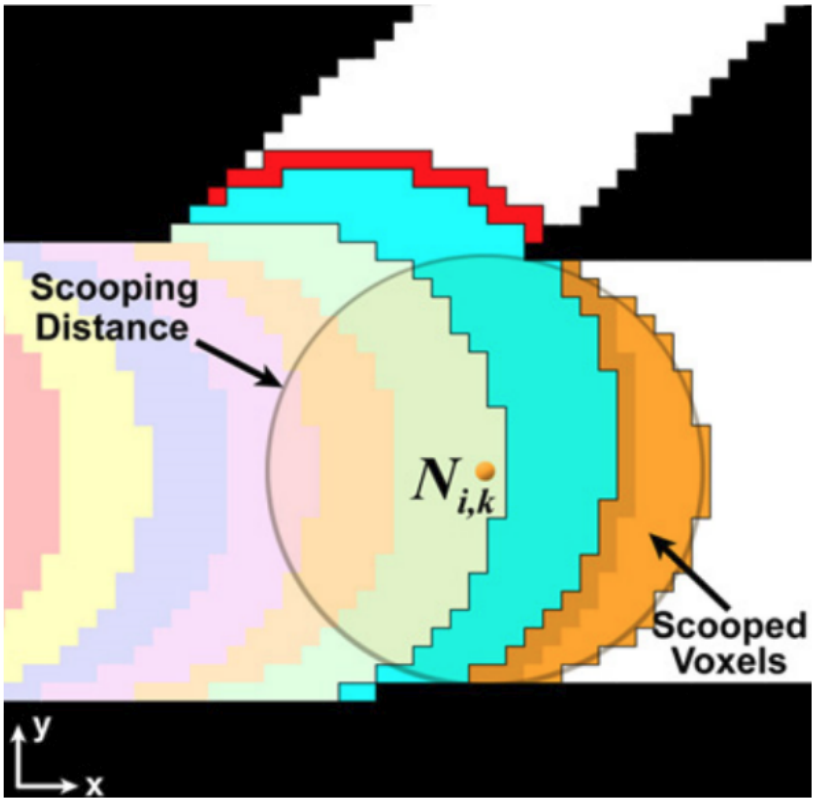

Figure 5.3: **Voxel scooping.** Starting from the seed (Figure 5.2b), it scoops the voxels by repeatedly creating clusters using the method of extending the region. $N_{i,k}$ is a centroid of a scooped voxel. Adapted from [94].

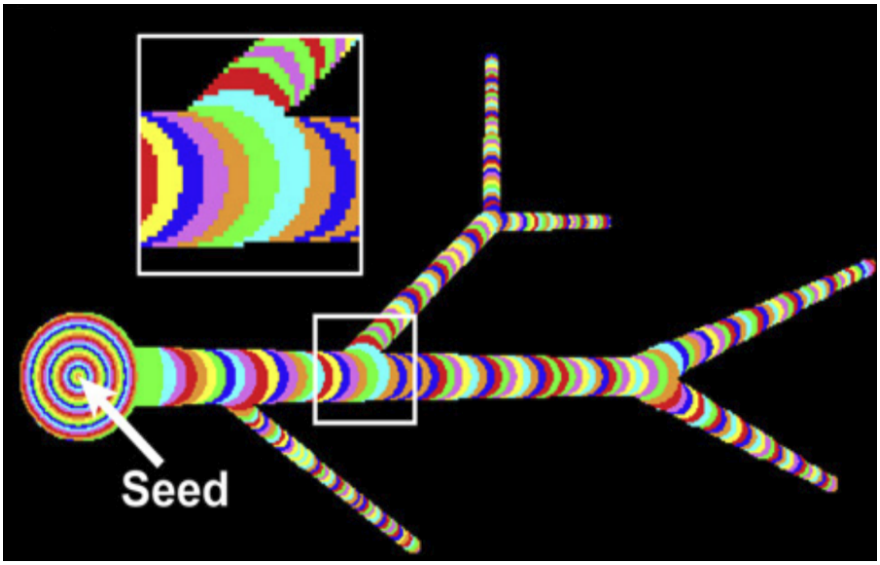

(a) Clusters after voxel scooping

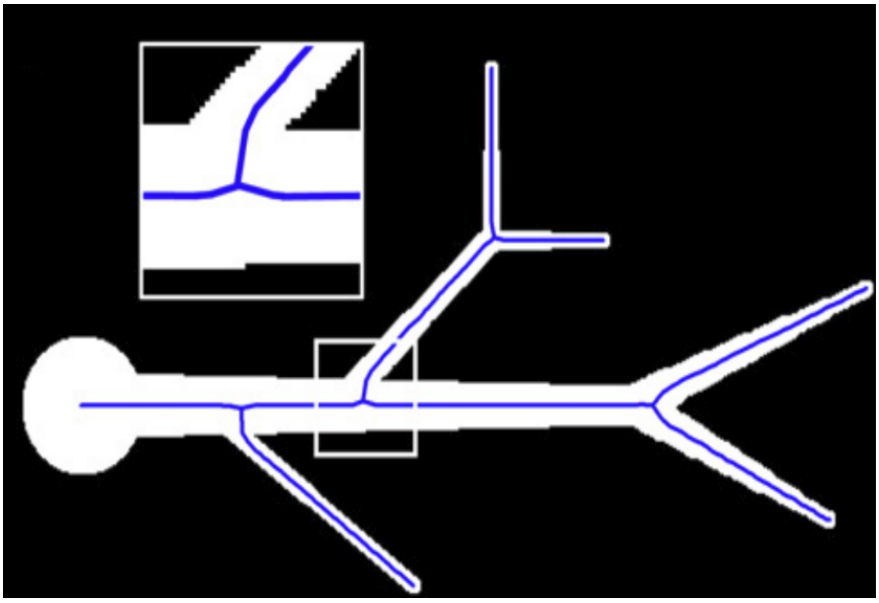

(b) The resulting centerline

Figure 5.4: **The result of voxel scooping method** (a) Clusters after vexel scooping. (b) The resulting centline. Voxel scooping until there is no unvisited region creates clusters with the structure. By connecting the centroids ($N_{i,k}$, Figure 5.3) obtained by the voxel scooping method, a blue centerline can be obtained. Adapted from [94].

```
#name MOST_Tracing
#comment
##n,type,x,y,z,radius,parent
1 3 3072.000 2928.800 776.000 4.800 -1
2 3 3071.200 2929.578 779.667 4.800 1
3 3 3073.239 2937.290 783.355 4.800 2
4 3 3067.200 2914.800 796.000 4.800 3
5 3 3064.800 2898.000 786.000 4.800 3
6 3 3069.600 2889.600 784.000 4.800 5
7 3 3059.200 2885.867 796.000 4.800 5
8 3 3062.400 2877.000 796.000 4.800 7
9 3 3120.000 2688.000 756.000 4.800 -1
10 3 3124.800 2856.000 576.000 19.200 -1
11 3 3126.390 2859.902 577.200 19.200 10
12 3 3139.604 2882.710 555.730 19.200 11
13 3 3114.542 2834.006 600.226 16.800 11
14 3 3113.673 2823.673 608.909 15.600 13
15 3 3110.965 2816.536 616.800 12.600 14
16 3 3116.160 2816.800 624.000 8.700 15
```

Figure 5.5: **SWC file format.** It consists of the central point, radius of the microvascular, and information about the connectivity. Figure 5.6 shows a visualized SWC file in Vaa3d software.

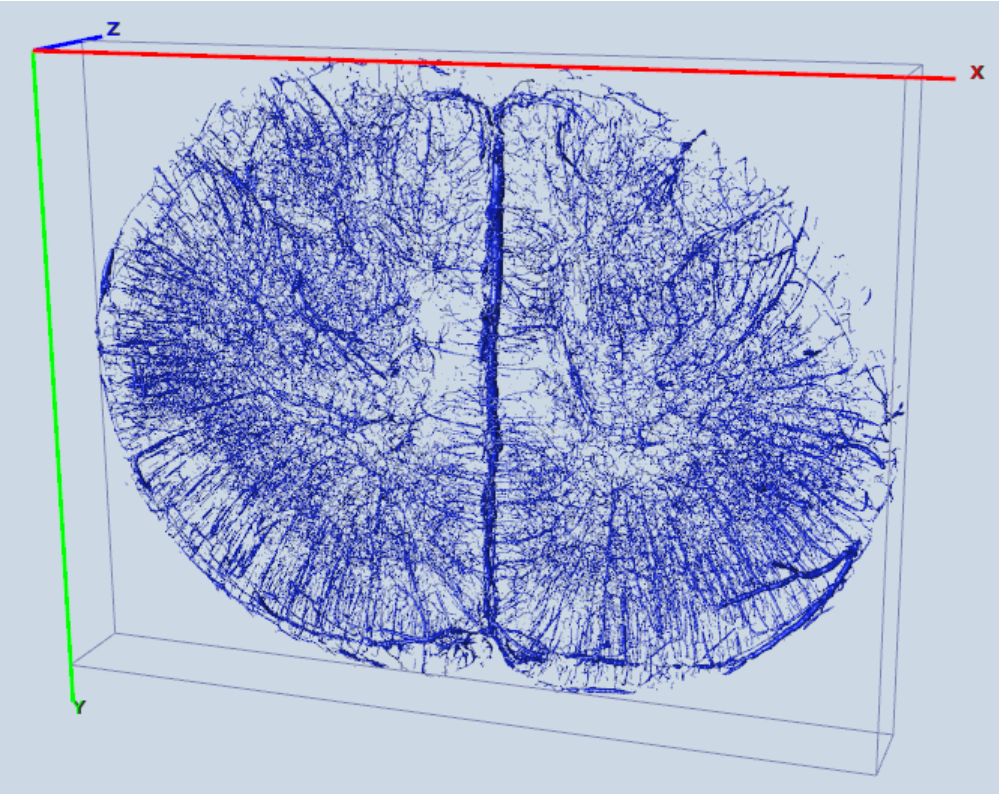

Figure 5.6: **Visualization of one SWC file.** It shows a result of one of the eleven sections of vascular tracing results with 3D viewer plugin of Vaa3D.

voxel scooping method [78].

This voxel scooping method consists of three steps as follows. To use the voxel scooping method, (1) it needs to find the seeds in the binarized image (Figure 5.2). The centroids of connected areas (white parts) in a 2D binarized image were seeds (red points). (2) Starting from the seed, in Figure 5.3, it scoops the voxels by repeatedly creating clusters (layers of different colors) using the method of extending the region. As shown in Figure 5.3, voxel scooping (until there is no unvisited region) creates clusters with the structure shown in Figure 5.4a. (3) By connecting the centroids ($N_{i,k}$, Figure 5.3) obtained by the voxel scooping method, a blue centerline can be obtained as shown in Figure 5.4b.

In order to apply the voxel scooping method, I recovered the KESM dataset to its original resolution (15,580 $\times$ 12,100 $\times$ 8,560 pixels) for tracing. The traced results cannot be obtained all at once due to the limitations of computing power at submicrometer resolution ($0.6\,\mu\mathrm{m} \times 0.7\,\mu\mathrm{m} \times 0.1\,\mu\mathrm{m}$). For this reason, I split the KESM dataset into 11 parts and traced each part. It is necessary to modify the value of the z coordinate to make each part unite, therefore local z coordinates were converted to global z coordinates along with the endpoint connections for stitching the 11 SWC files [10]. Figure 5.6 shows a result of one of the eleven sections of vascular tracing results with 3D viewer plugin [70] of Vaa3D.

After using the voxel scooping method, I can get 11 SWC files which consist of the central point, radius of the microvascular, and information about connectivity (Figure 5.5). In addition, I converted the SWC file format to a VTK file format for 3D visualization using ParaView software. The 3D viewer provided by Vaa3D is limited in showing large SWC files. However, using ParaView software does not cause any problems with running large VTK files.

2D based diameter measurement

In Figure 5.7, I used another algorithm for measuring the microvascular diameters. In the binarized 2D images, I picked the center point (x,y coordinates) of the microvacular segments in the same way as in Figure 5.2. Then, for each segment, distances from the center point to the boundary pixels were measured, among which, the minimum distance was used for a radius. As

shown in Figure 5.7a, when measuring the diameter of a blood vessel, the shortest length of the section becomes the diameter. At this time, I doubled the binarized image size and set the x, y resolution to $2.4\,\mu\mathrm{m} \times 2.8\,\mu\mathrm{m}$ when measuring the radius.

Results and analysis

Figure 5.8 and 5.10 show the 3D reconstruction of the whole mouse brain microvascular structure with minimum (Figure 3.11a) and Otsu's (including convex hull method, Figure 3.12) method of the KESM dataset. It can be seen that the results obtained using the Otsu's threshold method have rich vascular information including smaller vessels more than those using the minimum threshold method. In addition, the convex hull method removed noise outside the brain from the KESM dataset.

Analysis of the resulting SWC files allowed me to estimate the distribution of microvascular diameters as shown in Figure 5.9 and Figure 5.11. This is because the SWC file consists of the central point, radius of the microvascular, and information about the connectivity (Figure 5.5). In Figure 5.9a and Figure 5.11a, as the diameter size increases, the corresponding numbers sharply decrease (y-axis is log scale). Figure 5.9b and Figure 5.11b show the number of blood vessels in the categorized range according to the diameter size of the blood vessels with a percentage.

Table 5.1: Analysis of microvascular diameter ($\mu\mathrm{m}$). Adapted from [48].

	Average	Median	Min	Max
3D Otsu's (Figure 5.9)	10.62	9.60	9.60	192.00
3D Minimum (Figure 5.11)	13.39	9.60	9.60	140.40
2D-Based Minimum (Figure 5.7)	9.23	5.60	4.80	227.00

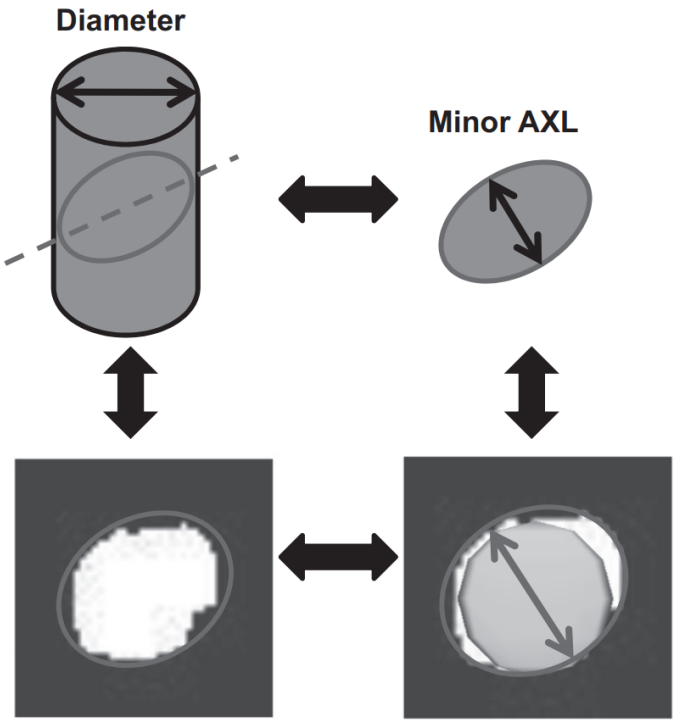

(a) The length of minor axis is a diameter of the vessel. Adapted from [49].

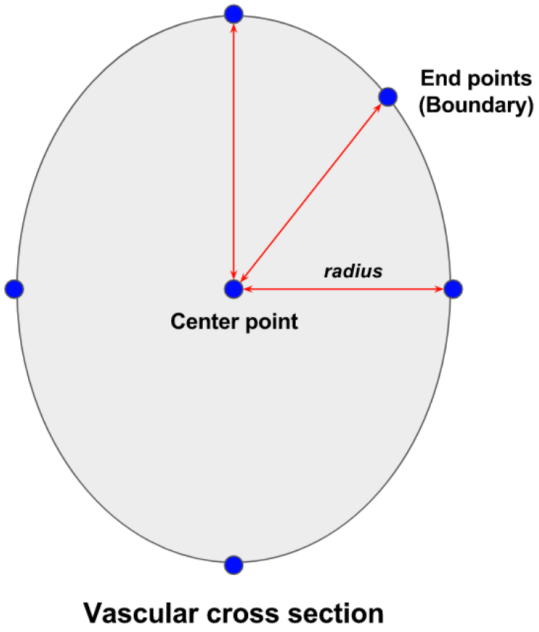

(b) Method for measuring the radius

Figure 5.7: **2D-Based distance to boundary for measuring diameter.** (a) The length of minor axis is a diameter of the vessel. (b) Measuring radius method. I picked the center point of the microvacular segments. Then, for each segment, distances from the center point to the boundary pixels were measured, among which the minimum distance was used for a radius, and twice the radius is the diameter.

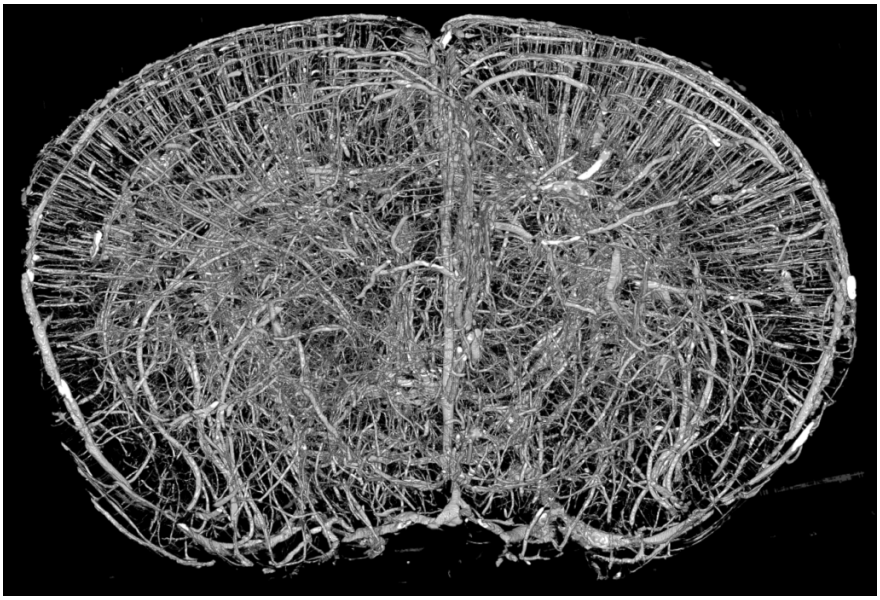

(a) Coronal view (↑: Dorsal, ↓: Ventral)

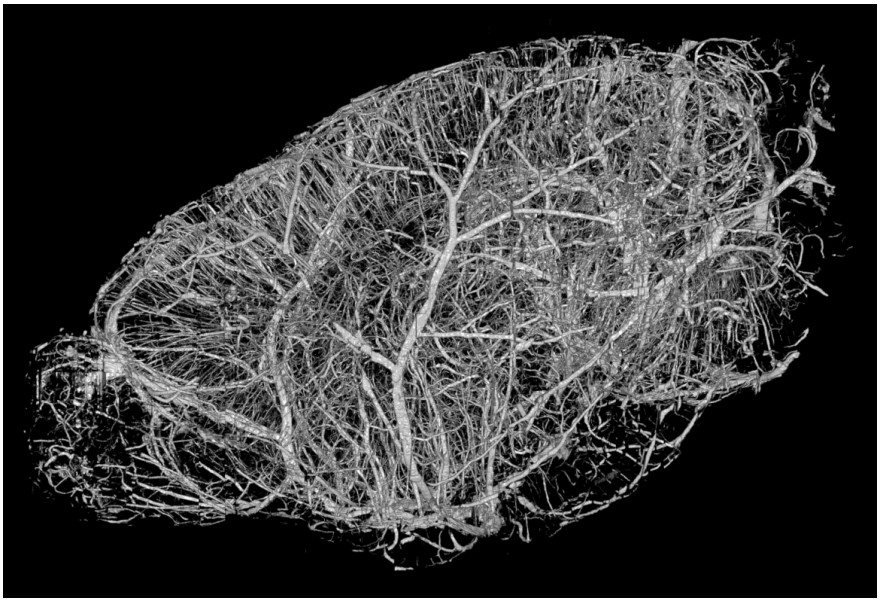

(b) Sagittal view (←: Anterior, →: Posterior)

Figure 5.8: **3D reconstruction of a microvascular structure using the KESM dataset with minimum threshold method.** (a), (b) shows the 3D reconstruction of the microvascular network of the whole mouse brain restored with the ImageJ software.Adapted from [47].

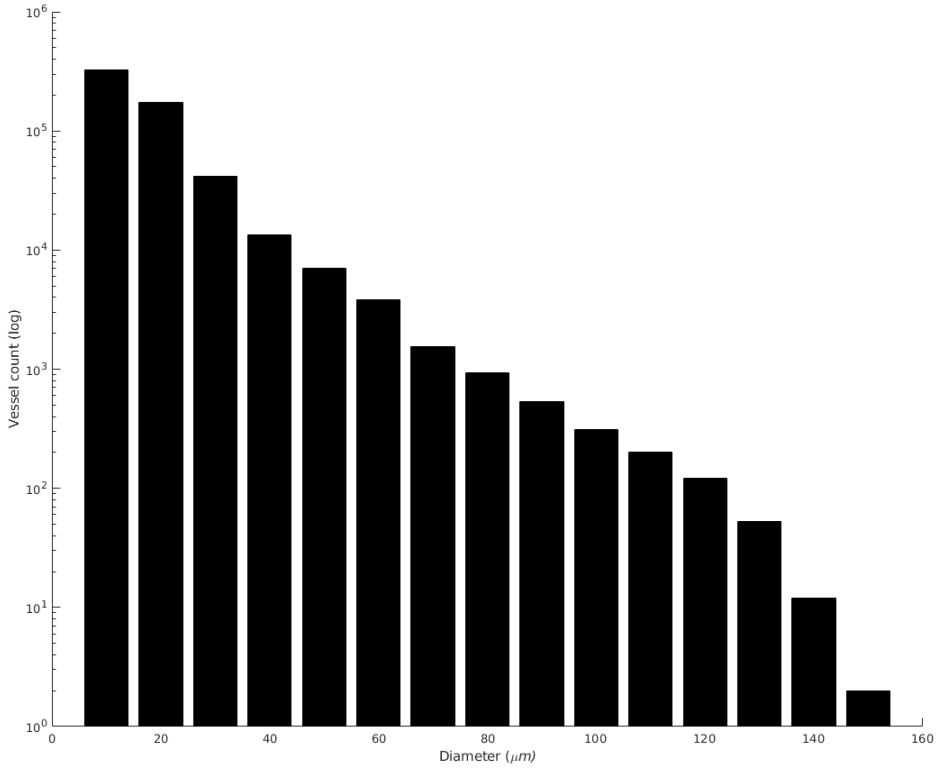

(a) Vessel counts by diameter size. Adapted from [48].

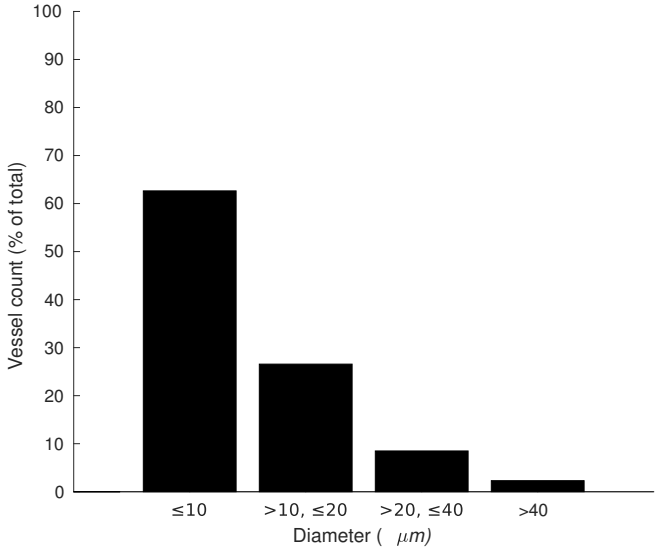

(b) Vascular counts by categorized diameter size.

Figure 5.9: **Distribution of diameter** The graphs of distribution of microvascular diameters using the KESM dateset with minimum threshold method.

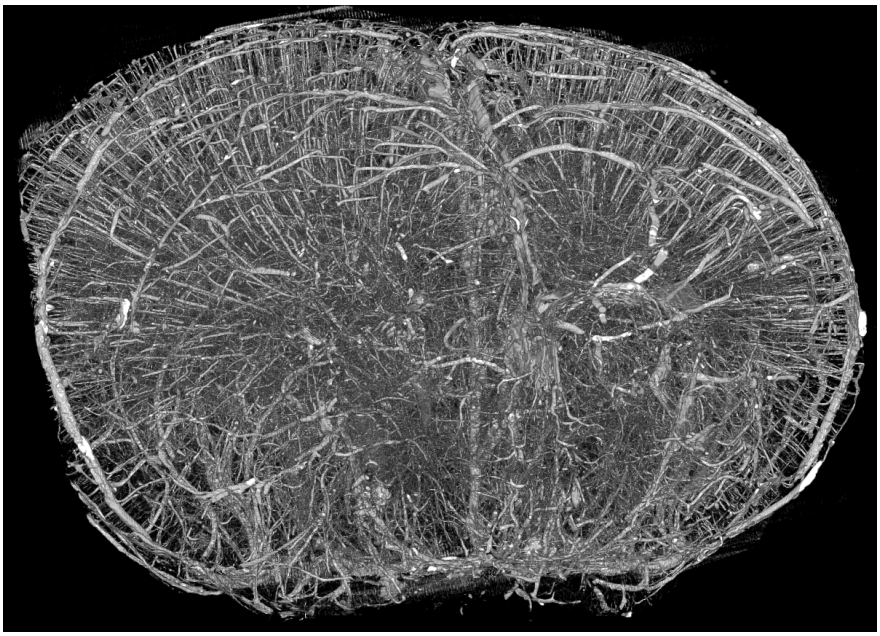

(a) Coronal view (↑: Dorsal, ↓: Ventral)

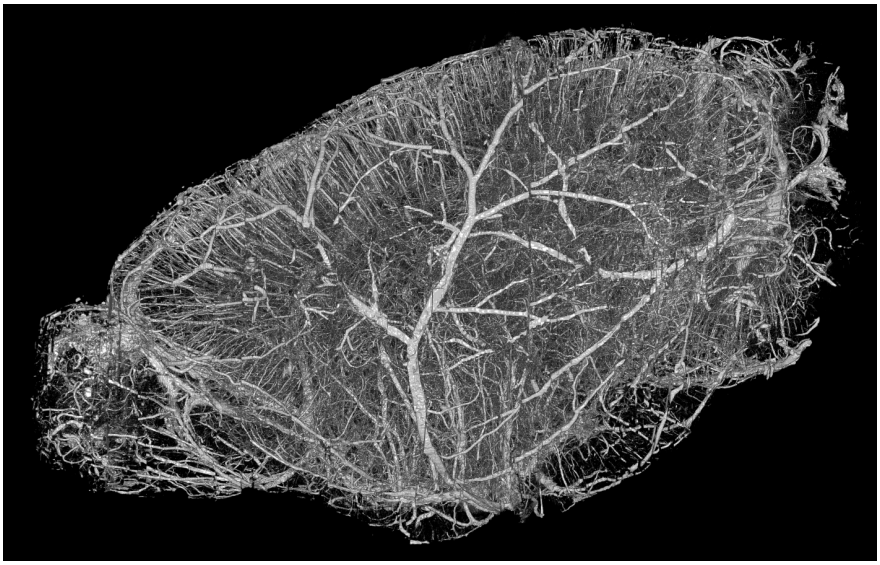

(b) Sagittal view (←: Anterior, →: Posterior)

Figure 5.10: **3D reconstruction of a microvascular structure using the KESM dataset with Otsu's threshold method.** (a), (b) shows the 3D reconstruction of the microvascular network of the whole mouse brain restored with the ImageJ software.

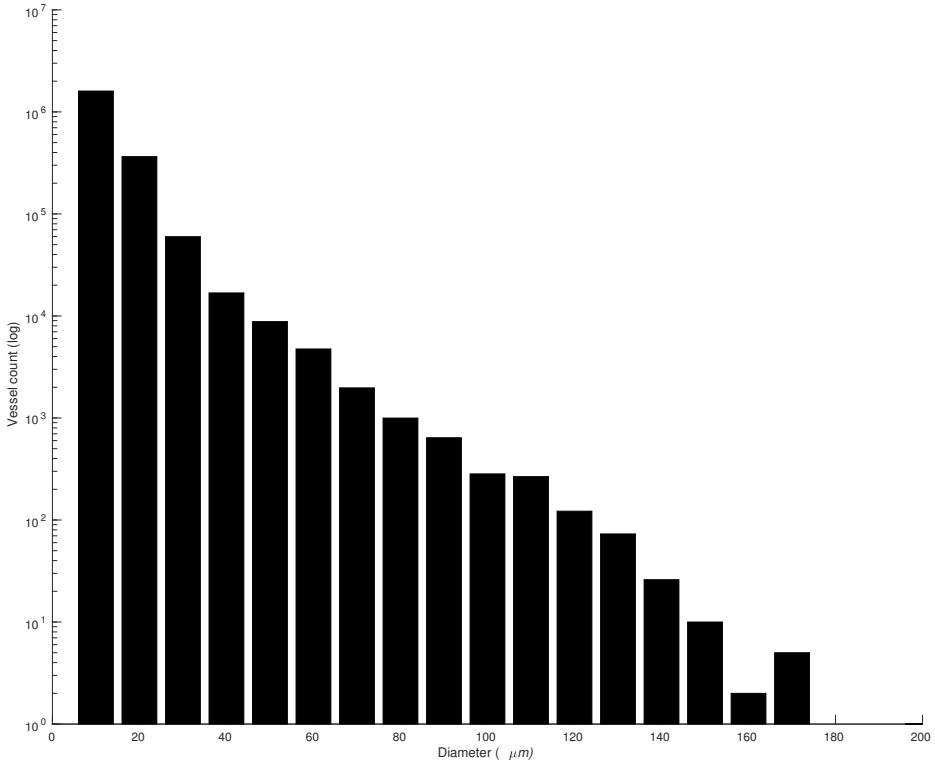

(a) Vessel counts by diameter size.

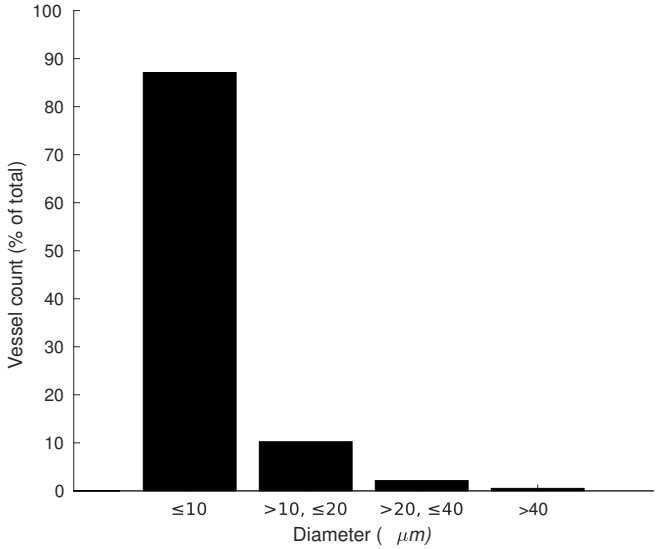

(b) Vascular counts by categorized diameter size.

Figure 5.11: **Distribution of diameter.** The graphs of distribution of microvascular diameters using the KESM dateset with Otsu's threshold method.

Table 5.1 shows the comparison results of the average, median, minimum and maximum diameter values by the microvascular in 2D and 3D situations. It can be seen that there is about a two-fold difference in value between the median and minimum between 2D and 3D. The reason for this result is that the Vaa3d plugin measures the longest distance from the center to boundaries of the blood vessel as a radius [71]. This difference shows that the minimum distance measured in the binarized 2D image may not be the exact diameter of the microvascular. The average value of the Otsu's threshold method is smaller than that of the minimum threshold method. On the other hand, the maximum diameter value of the Otsu's threshold method is larger than that of the minimum threshold method. This difference is due to the fact that I have obtained abundant information about blood vessels using the more aggressive threshold method (Otsu's). This also helped to obtain information about small-sized vessels, including capillaries.

Xie $et\ al.$ [95] used twelve adult male C57BL/6 mice and obtained the mean vascular diameters of BA (basal artery), ACA (anterior cerebral artery), and MCA (middle cerebral artery) with Micro-X-ray computerized tomography. The results were $190 \pm 5\mu\mathrm{m}$, $100 \pm 5\mu\mathrm{m}$, and $120 \pm 5\mu\mathrm{m}$, respectively. The largest diameter result ($190 \pm 5\mu\mathrm{m}$) is similar to my results (in Table. 5.1).

Table. 5.2 describes a geometric analysis of the total microvascular network. I divided the KESM dataset into 11 parts to analyze the whole brain blood vessel (Figure 5.6). This table lists the number of bifurcations and the volume of each segment with two types of threshold method (minimum and Otsu's). The bifurcations and the volume size when using the Otsu's threshold method in all segments were larger than when using the minimum threshold method. In addition, Table. 5.3 describes a geometric analysis of the microvascular network of length and surface. Same as Table. 5.2, the length and the surface size when using the Otsu's threshold method in all segments were larger than when using the minimum threshold method.

Figure 5.12 and Figure 5.14 show the microvascular tracing result of the whole mouse brain restored using two kinds of threshold methods (minimum and Otsu's) with ParaView software. From this result, I can confirm that the Otsu's threshold method obtained more abundant vessel information than the tracing result using the minimum threshold method. Figure 5.13 and Figure

Table 5.2: Geometric analysis of the total microvascular network

Segments No.	Minimum threshold method		Otsu's threshold method	
	Bifurcations	Volume (μm^3)	Bifurcations	Volume (μm^3)
1	279	5,319,400	1,399	16,495,300
2	1,773	42,458,800	5,361	83,664,700
3	2,459	89,324,200	8,558	116,135,700
4	4,196	165,699,000	18,702	313,694,000
5	5,081	209,196,000	20,766	385,968,000
6	5,239	240,860,000	20,883	431,921,000
7	5,904	214,802,000	20,597	293,508,000
8	6,623	204,284,000	14,169	227,700,000
9	7,291	252,251,000	22,692	417,472,000
10	5,912	181,771,000	19,103	329,648,000
11	2,694	90,513,400	20,123	266,320,000
Total	47,451	1,696,478,800	203,406	3,328,966,700

Table 5.3: Geometric analysis of the microvascular network of length and surface

Segments No.	Minimum threshold method		Otsu's threshold method	
	Length (μm)	Surface (μm^2)	Length (μm)	Surface (μm^2)
1	34,857	1,408,480	147,556	5,213,160
2	214,081	9,313,500	580,142	21,996,400
3	410,220	18,349,000	1,079,710	41,348,800
4	705,703	31,245,900	2,229,000	82,362,000
5	927,198	41,092,400	2,596,870	98,217,000
6	992,270	44,961,400	2,682,450	103,525,000
7	960,776	43,053,600	2,268,020	81,862,400
8	966,280	41,929,000	1,715,530	62,438,600
9	1,003,830	45,875,400	2,580,110	99,147,600
10	811,091	36,516,700	2,140,390	81,867,500
11	407,150	17,842,300	2,148,830	76,277,800
Total	7,433,456	331,587,680	23,505,218	876,447,260

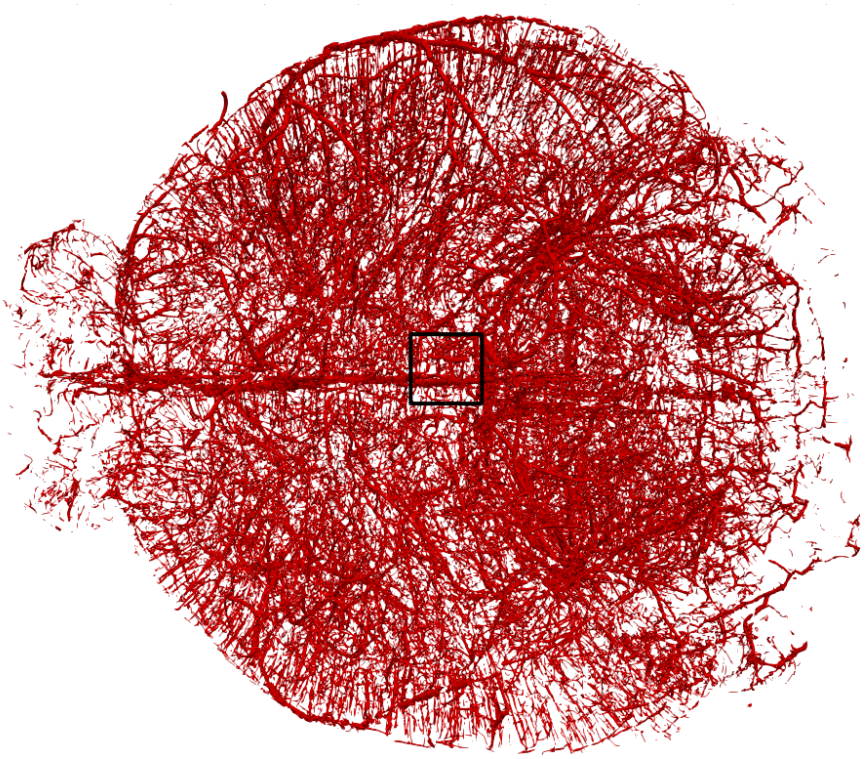

(a) Horizontal view (←: Anterior, →: Posterior)

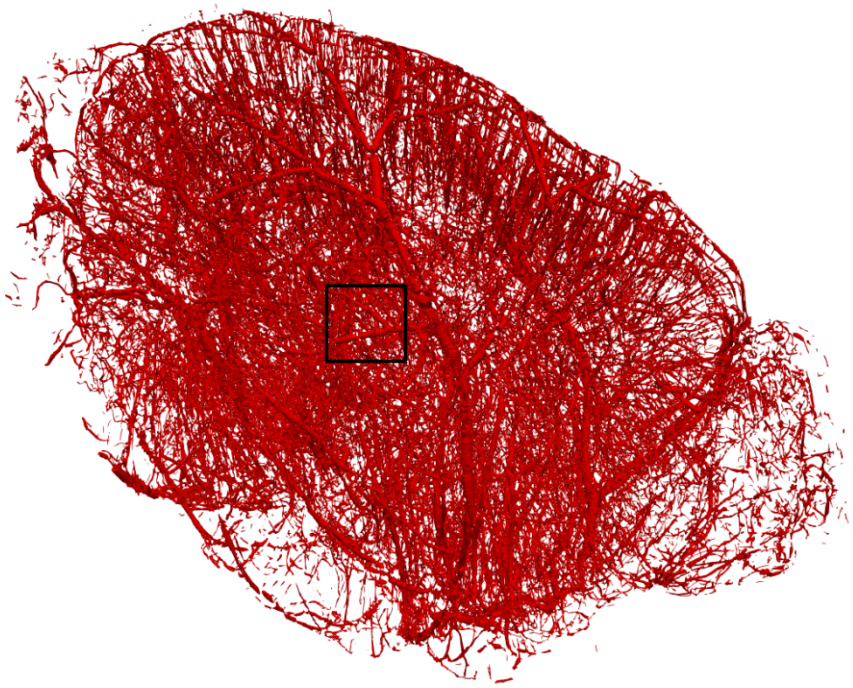

(b) Sagittal view (←: Posterior, →: Anterior)

Figure 5.12: **Network tracing based on minimum threshold method results.** (a) and (b) are the microvascular tracing results of the whole mouse brain restored with the ParaView software. Adapted from [47].

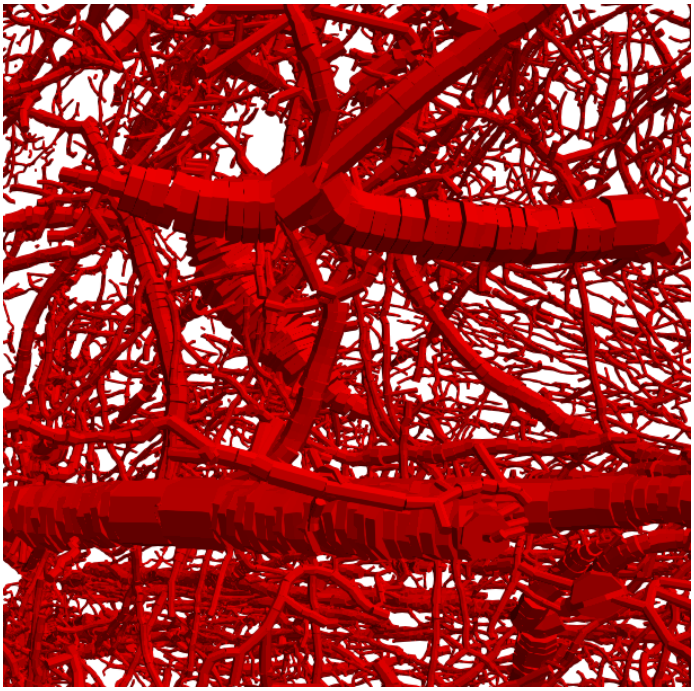

(a) Enlargement of Figure 5.12a (←: Anterior, →: Posterior)

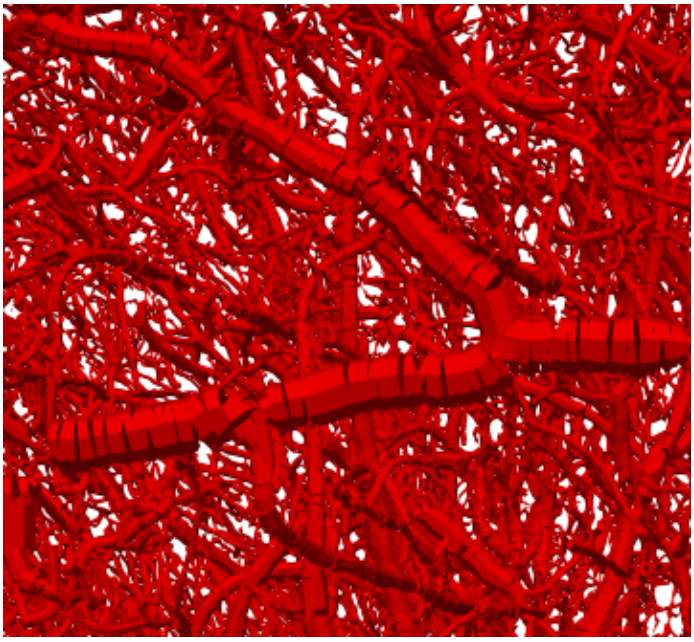

(b) Enlargement of Figure 5.12b (←: Posterior, →: Anterior)

Figure 5.13: **Enlarged images of tracing based on minimum threshold method results.** (a) and (b) are the enlargements of the black rectangular part of Figure 5.12a and Figure 5.12b. Adapted from [47].

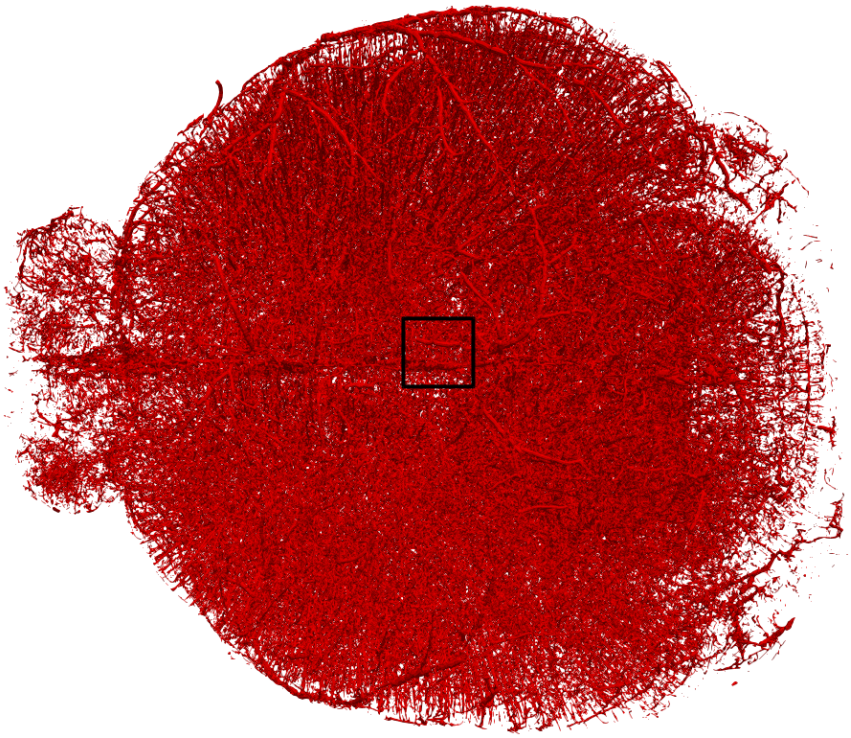

(a) Horizontal view (←: Anterior, →: Posterior)

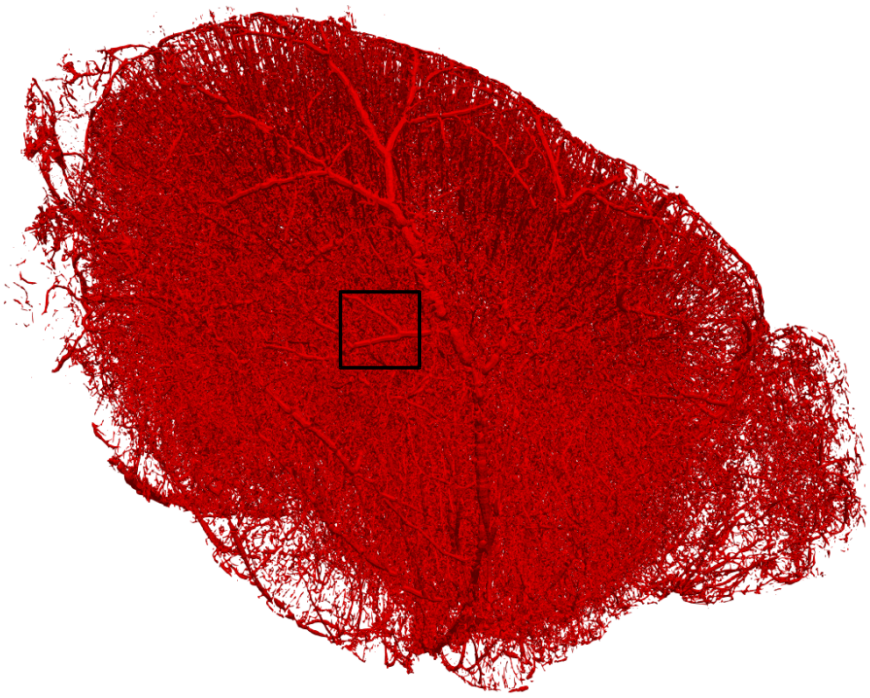

(b) Sagittal view (←: Posterior, →: Anterior)

Figure 5.14: **Network tracing based on Otsu's threshold method results.** (a) and (b) are the microvascular tracing results of the whole mouse brain restored with the ParaView software. I was able to obtain more abundant vascular information using a more aggressive threshold option (Otsu's method). Adapted from [48].

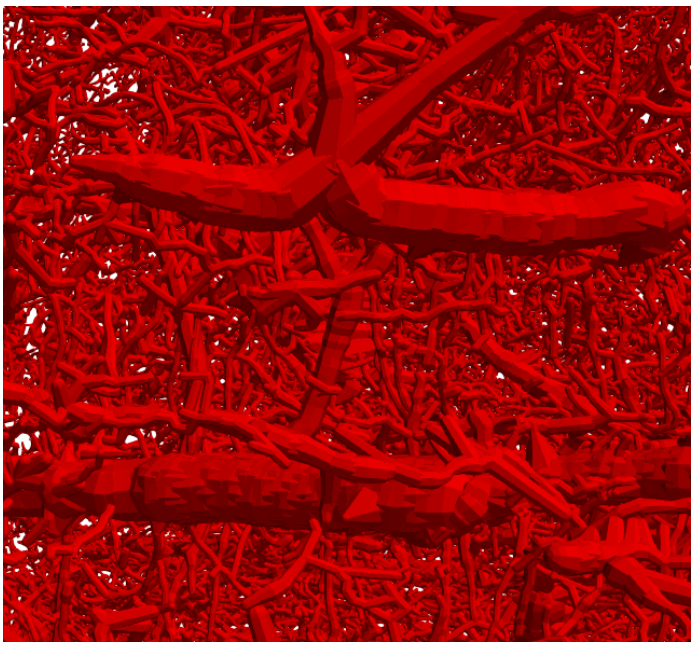

(a) Enlargement of Figure 5.14a (←: Anterior, →: Posterior)

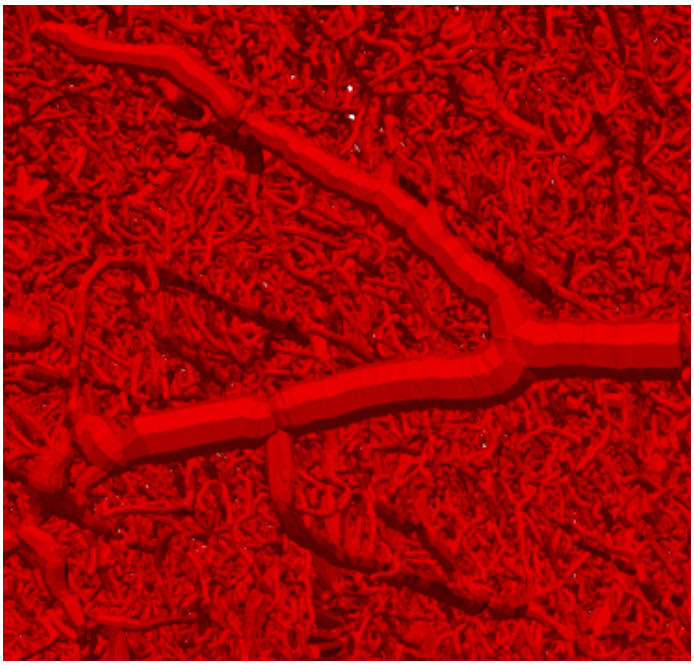

(b) Enlargement of Figure 5.14b (←: Posterior, →: Anterior)

Figure 5.15: **Enlarged images of tracing based on Otsu's threshold method results.** (a) and (b) are the enlargements of the black rectangular part of Figure 5.14a and Figure 5.14b. Adapted from [48].

5.15 show the enlargement of the black rectangles in Figure 5.12 and Figure 5.14, and I can see that when using the Otsu's threshold method, the number of small vessels increase, and that the larger vessels become clearer.

In conclusion, I was able to obtain richer blood vessel information and analyze the vascular structure of the whole mouse brain when using the Otsu's threshold method through 3D reconstruction, tracing, analyzing the geometric results.

CONVOLUTIONAL NEURAL NETWORK (CNN) FOR THE AUTOMATIC CLASSIFICATION OF IMPAIRED MOUSE BRAIN IMAGES.

Motivation

In Figure. 3.3, I manually selected the heavily damaged images due to the serial sectioning process from the KESM dataset in order to replace them with blank images. This manual operation requires a lot of time and effort, and was used in previous studies [50, 6] with KESM datasets as well. In this dissertation, I propose a method for the automatic classification of impaired mouse brain images to replace the manual operation. I utilized Convolutional Neural Network (CNN) [45, 100, 32] for the classification task. CNN is a type of Deep Learning [81] method that has been successfully applied to image classification and object detection [27, 88] tasks such as handwritten digit identification [44, 97], recognition of traffic signs [86], and classification of 1,000 different object classes [40].

Background

Convolutional Neural Network (CNN)

Figure 6.1 illustrates the experiment by David Hubel and Torsten Wiesel [35, 36]. This is an experiment to record the individual visual cortex neuron's response in a cat given the visual stimulation in the form of light bars shown on the screen. When they experimented with the cat, they found that only neurons responded to only inputs at specific locations in the visual field. Also, the responses were very specific to certain kinds of inputs, which was oriented bars. CNN was created based on this concept of local processing with a small set of common features.

However, using multi-layer perceptron (MLP) [26, 73] or multi-layered neural network in areas

Part of this chapter is reprinted with permission from "Tracing and analysis of the whole mouse brain vasculature with systematic cleaning to remove and consolidate erroneous images." by Junseok Lee, Jaewook Yoo, and Yoon-suck Choe. 2018. 40th Annual International Conference of the IEEE. Engineering in Medicine and Biology Society (EMBC), EMBC copyright line © 2018 under IEEE.

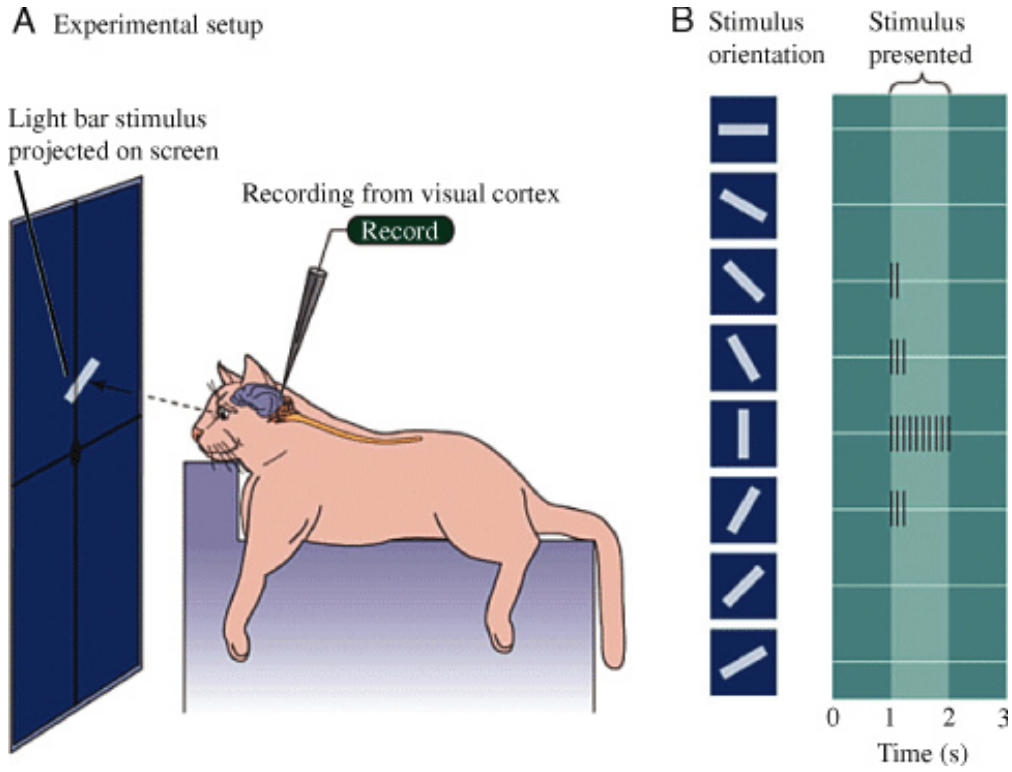

Figure 6.1: **Hubel and Wiesel's vision experiments.** This is an experiment to record the individual visual cortex response of a cat to oriented light bar stimulation displayed on the screen. When they experimented with the cat, they found that only neurons responded to only inputs at specific locations in the visual field. Also, the responses were very specific to certain kinds of inputs, which was oriented bars. Adapted from [75].

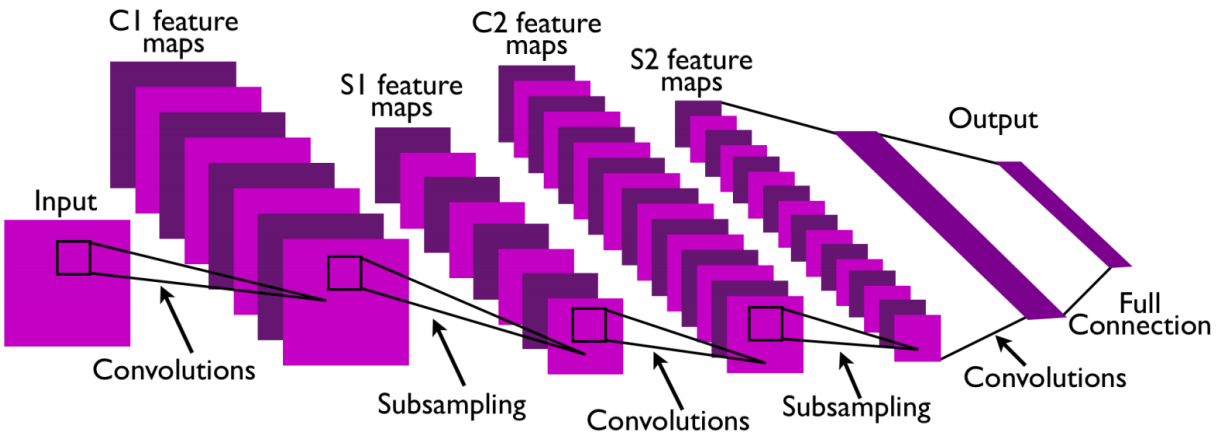

Figure 6.2: **Typical CNN architecture with convolution and subsampling layers.** CNN architecture consists of convolution and pooling (subsampling) layers optionally followed by fully connected layers. The correlation between spatially adjacent information is extracted using a convolutional filter. Various feature maps can be extracted by applying multiple filters. Sub-sampling (pooling) reduces input data size and combines with iterative filtering to obtain a global feature. In this case, the number of parameters is reduced by sharing the free parameter (weight, bias) applied to the entire input, thereby lowering learning time and overfitting. In other words, a salient feature with invariance (or robustness) independent of the phase change of the input data can be derived. Adapted from [46].

such as image recognition, MLP sees that all inputs have the same level of importance regardless of their location. Therefore, when a fully-connected neural network is constructed using this, there is a problem that the size of the parameter becomes extremely large. CNN also solves this problem by local processing (receptive field) and shared weights.

Figure 6.2 shows a typical CNN architecture that consists of convolution and pooling (subsampling) layers optionally followed by fully connected layers. In the field of image processing, convolution is mainly used for filter operation, and convolution is used to implement a filter to extract specific features from an image. As shown in Figure 6.3a, that is, if the window or mask of m by m is repeatedly performed on the entire image, an appropriate result can be obtained according to the coefficient values of the mask.

Pooling uses only neighboring pixel values, similar to convolution, but does not require special operations to multiply or add, as shown in Figure 6.3b. Pooling reduces the size of the image. Typical sub-sampling methods are max pooling and average pooling. Max pooling sets the largest

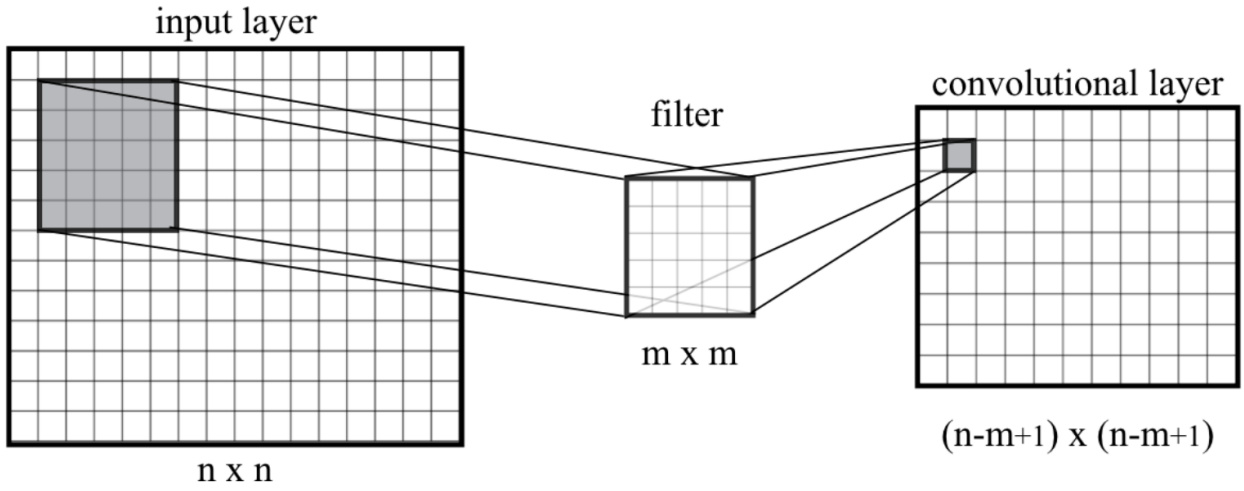

(a) Convolution process.

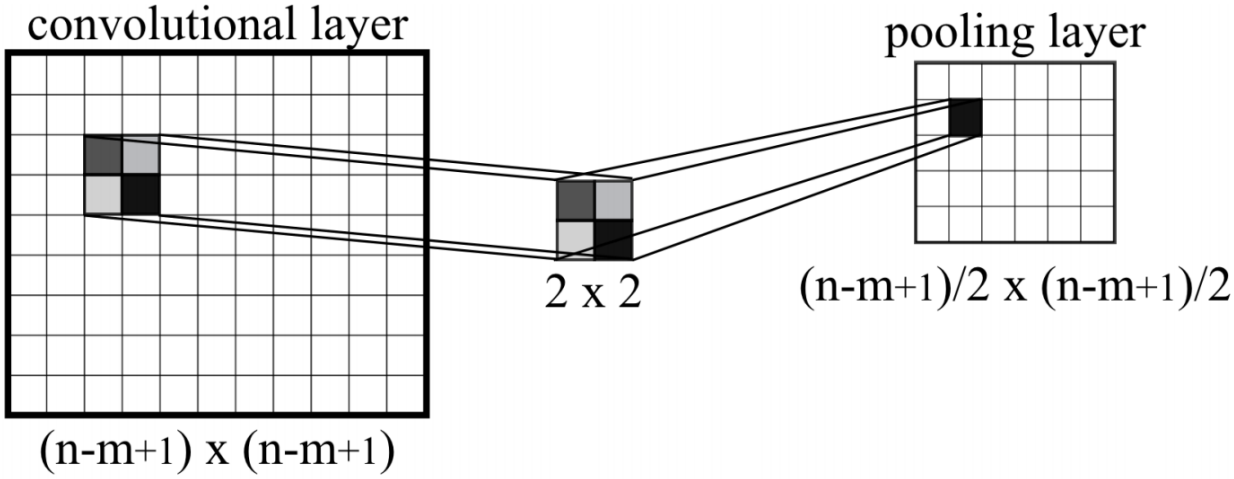

(b) Pooling process.

Figure 6.3: **Details of convolution and pooling processes in Figure 6.2.** (a) Convolution process. If the window or mask of m by m is repeatedly performed on the entire image (n by n), an appropriate result (n-m+1) by (n-m+1) can be obtained according to the coefficient values of the mask. (b) Pooling process. Pooling uses only neighboring pixel values, similar to convolution, but does not require special operations to multiply or add. Pooling reduces the size of the image. Adapted from [93].

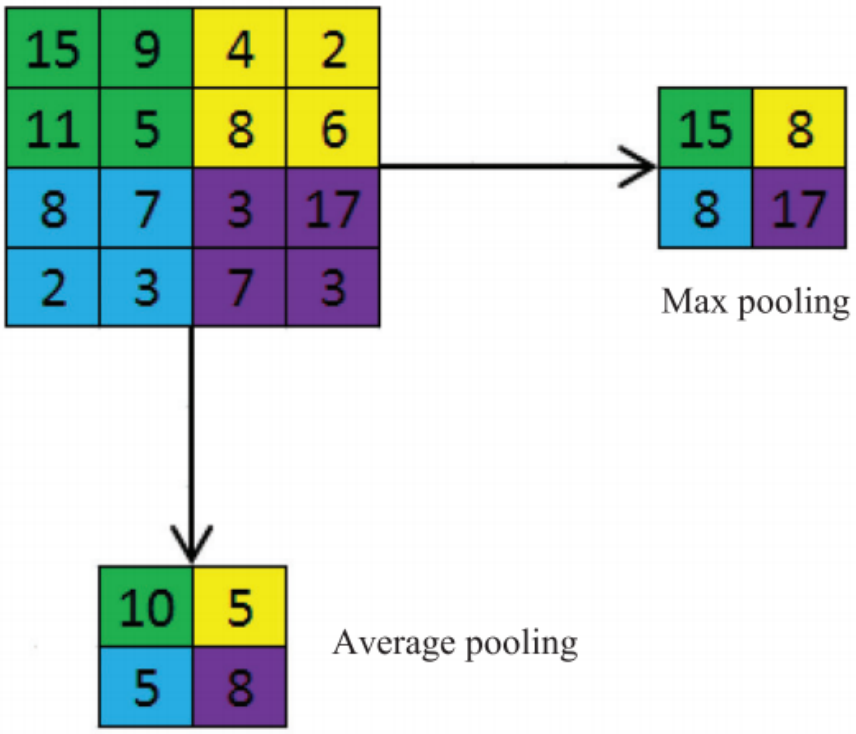

Figure 6.4: **Max and average pooling methods.** Typical sub-sampling methods are max pooling and average pooling. Max pooling sets the largest value in the adjacent pixels to the new pixel value, and average pooling sets the average value of the adjacent pixels to the new pixel value. Adapted from [76].

value in the adjacent pixels to the new pixel value, and average pooling sets the average value of the adjacent pixels to the new pixel value (Figure 6.4). At the end of the various convolution and pooling processes and flattening of layers, a high level of inference of the neural network is performed through fully connected layers.

Finally, the correlation between spatially adjacent information is extracted using a convolutional filter and various feature map can be extracted by applying multiple filters. Sub-sampling (pooling) reduces input data size, and combines with iterative filtering to obtain a global feature.

Inception V3

CNN shows better performance with deeper networks [84, 88, 63]. Google has developed an Inceptive module [88] that has a much deeper network depth than the architecture of Krizhevsky $et\ al.$ [40], but with 12 times fewer parameters and higher accuracy. The Inception v1 named GoogLeNet [88] was awarded the best prize in 2014 by participating in the ImageNet Large Scale Visual Recognition Challenge (ILSVRC 2014) [79], which evaluates image classification technology.

Figure 6.5 shows the Inception module. It is possible to effectively extract features of various scales through the convolution kernels (blue rectangle) of different sizes in the inception module. In addition, through the 1×1 convolution layer (yellow rectangle) used in various places inside the Inception module, it is possible to increase the input area and depth of the network by greatly reducing the calculation amount.

Inception V3 [89] is a model that improves the large-scale convolutions (e.g. 5×5 or 7×7) to a small-sized multi-layer structure by applying the factorization method. If the 5×5 convolution is replaced by two 3×3 convolutions as shown in Figure 6.6b, the computation is reduced by about 28% (25:18). Figure 6.6c shows the factorization of the $N \times N$ convolution to $1 \times N$ and $N \times 1$, and the computation is reduced by 33%. This improved version of Inception v3 shows good performance in image classification and reduces image classification errors by almost half compared to GoogLeNet.

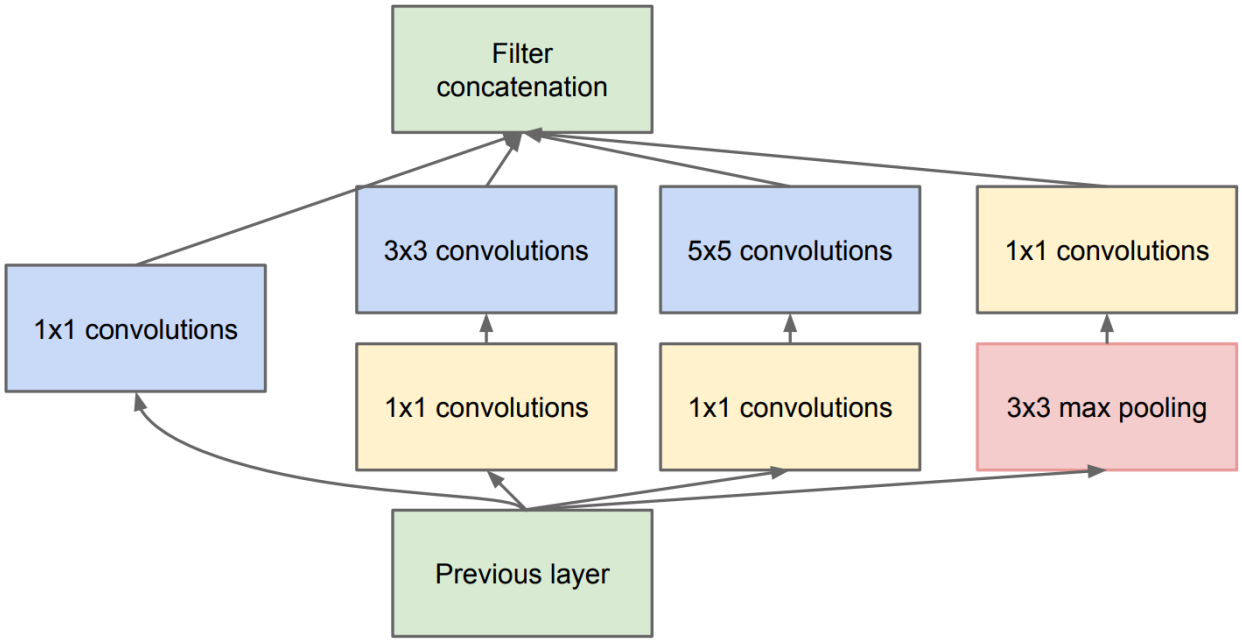

Figure 6.5: **Inception module.** It is possible to effectively extract features of various scales through the convolution kernels (blue rectangle) of different sizes in the inception module. In addition, through the 1×1 convolution layer (yellow rectangle) used in various places inside the Inception module, it is possible to increase the area and depth of the network by greatly reducing the calculation amount. Adapted from [88].

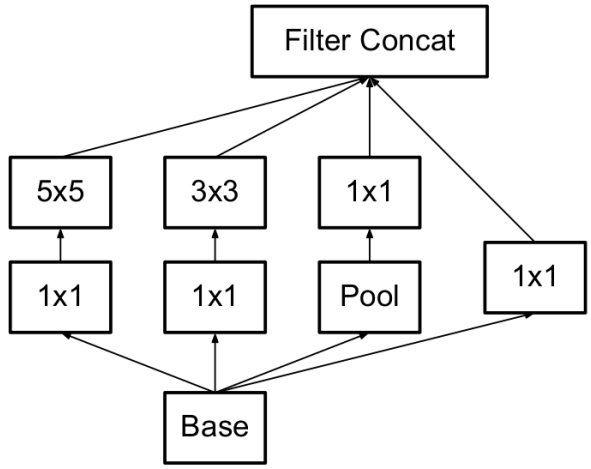

(a) Original Inception module

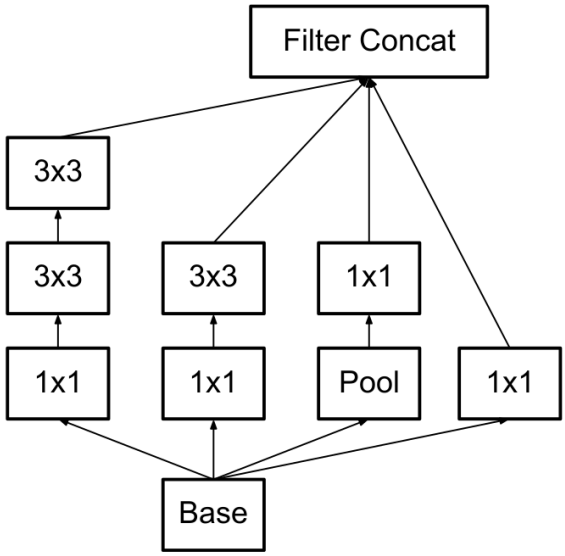

(b) Replacing each 5×5 convolution with two 3×3 convolutions.

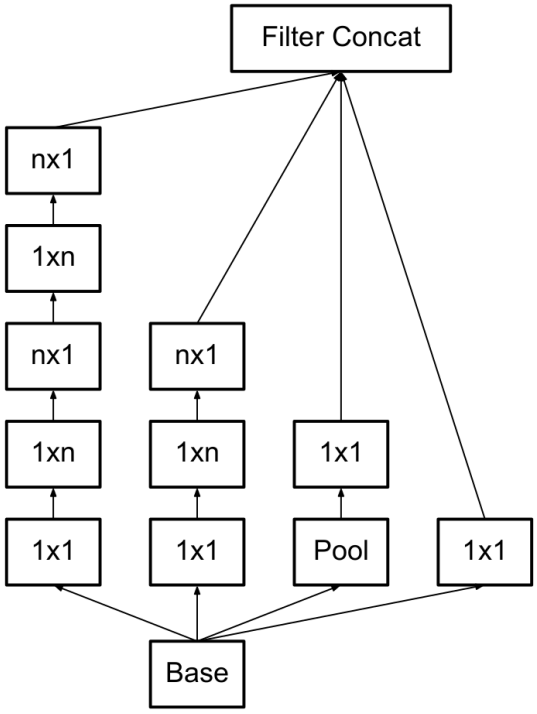

(c) Factorization of convolution in N $\times$ N form to 1$\times$N and N$\times$1.

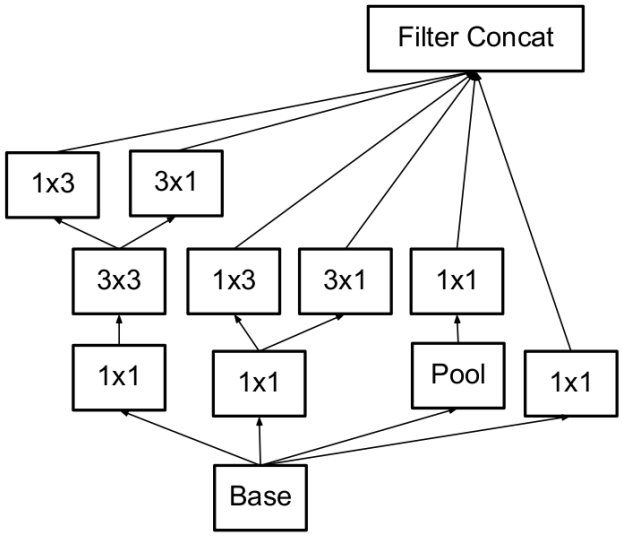

(d) Extended the filter bank outputs.

Figure 6.6: **Inception V3 module.** (a) Original Inception module. Inception V3 is a model that improves the large-scale convolutions (e.g. 5$\times$5 or 7$\times$7) to a small-sized multi-layer structure by applying the factorization method. (b) The 5×5 convolution is replaced by two 3×3 convolutions, the computation is reduced by about 28% (25:18). (c) The factorization of the N x N convolution to 1 x N and N x 1, and the computation is reduced by 33%. (d) Extended the filter bank outputs. Adapted from [88, 89].

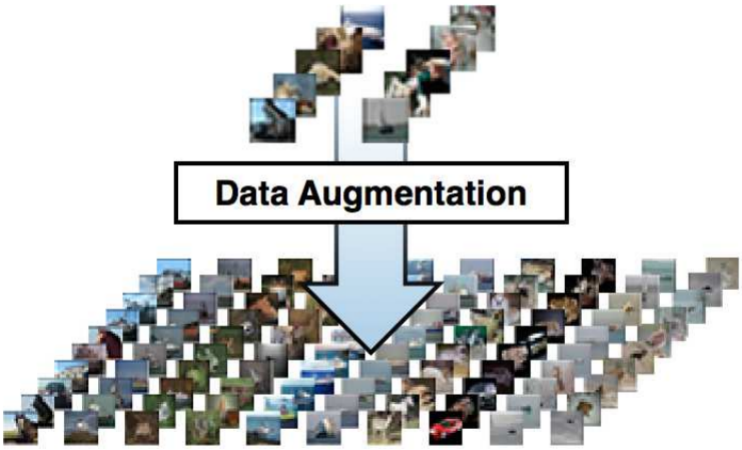

(a) Concept of data augmentation

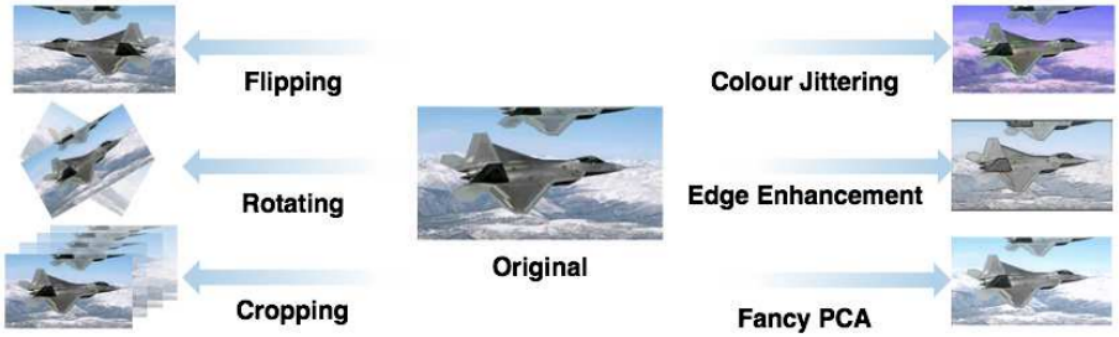

(b) Various methods of data augmentation.

Figure 6.7: **Data augmentation using label preserving transformations.** (a) Concept of data augmantation. (b) Various methods of data augmentation. Adapted from [90].

Approach / Method

The data preparation process for training the CNN model is shown in Figure. 6.9. I apply the convex hull mask images (C) on the raw images (R) to create the masked images (M). The convex hull masks were used to create images that focus only on the part of the mouse brain tissue. Artificial neural networks need large amounts of training dataset to obtain effective learning outcomes [11, 53]. Since the amount of KESM data is limited, I applied the data augmentation [98] method to artificially increase the amount of data.

Figure 6.7 shows data augmentation using label preserving transformations. In order to artificially increase the number of KESM data, I prepared the data using the flipping and the rotating techniques in Figure 6.7b. The images are flipped vertically, horizontally, and vertically and horizontally (V, H, and VH) for data augmentation (Figure 6.9). After the preparation process, the 8,142 raw KESM images become 32,568 images that are sufficient for training and testing. 80% of the images are used for training and 20% are used for testing. 10% from the training set is used as a validation set.

Figure 6.10 shows the overview of the proposed method with the KESM dataset for impaired image classification (two cases: "good" or "impaired". The Inception V3 model is utilized for the CNN architecture. The architecture consists of 5 convolutional layers and 2 pooling layers. For the input images of the CNN, the images from the preparation process with the resolution of 7790×6050 are sub-sampled to the resolution of 299×299. The labels of the images ("good" or "impaired) are provided. Also, I compared the classification accuracy of the impaired images for the KESM datasets between the CNN and a baseline method, Support Vector Machine (SVM) [18, 3].

Figure 6.8 illustrates the SVM, a traditional classification approach. As shown in Figure 1.1, there are several ways (discrimination boundaries) to classify two classes -1 and +1. SVM tries to find the best hyperplane (the maximum margin boundary) separating two classes -1 and +1 [65].

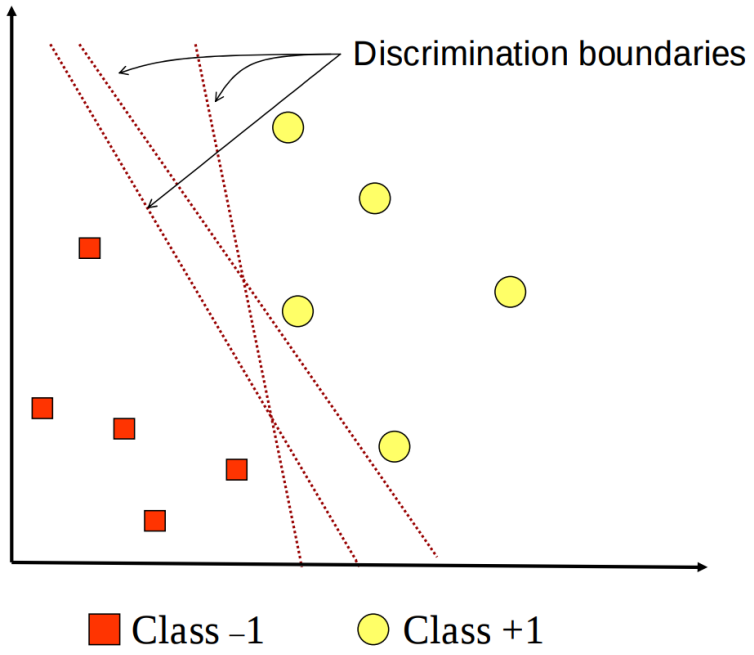

(a) Possible solutions.

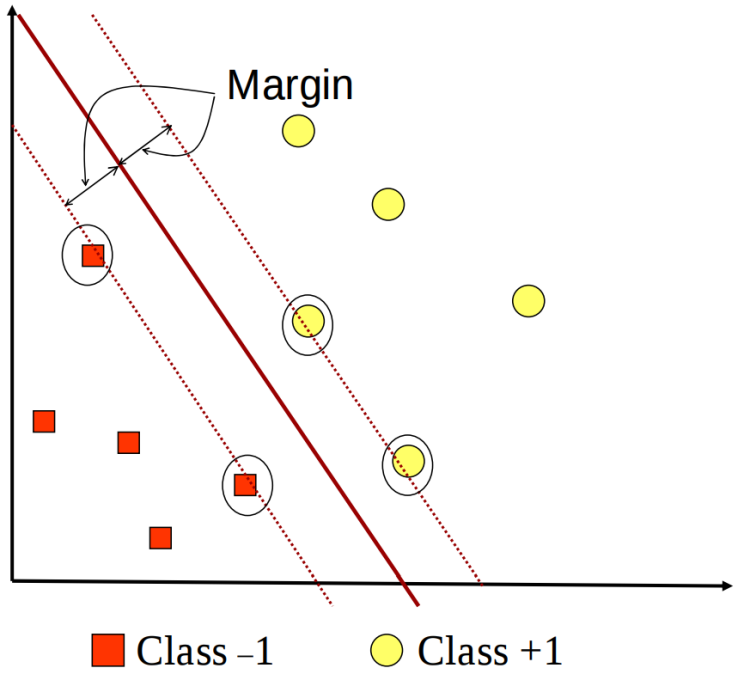

(b) The maximum margin boundary.

Figure 6.8: **The motivation of Support Vector Machine (SVM).** (a) Possible solutions for separating two classes -1 and +1. (b)The maximum margin boundary. SVM tries to find the best hyperplane separating two classes -1 and +1. Adapted from [65].

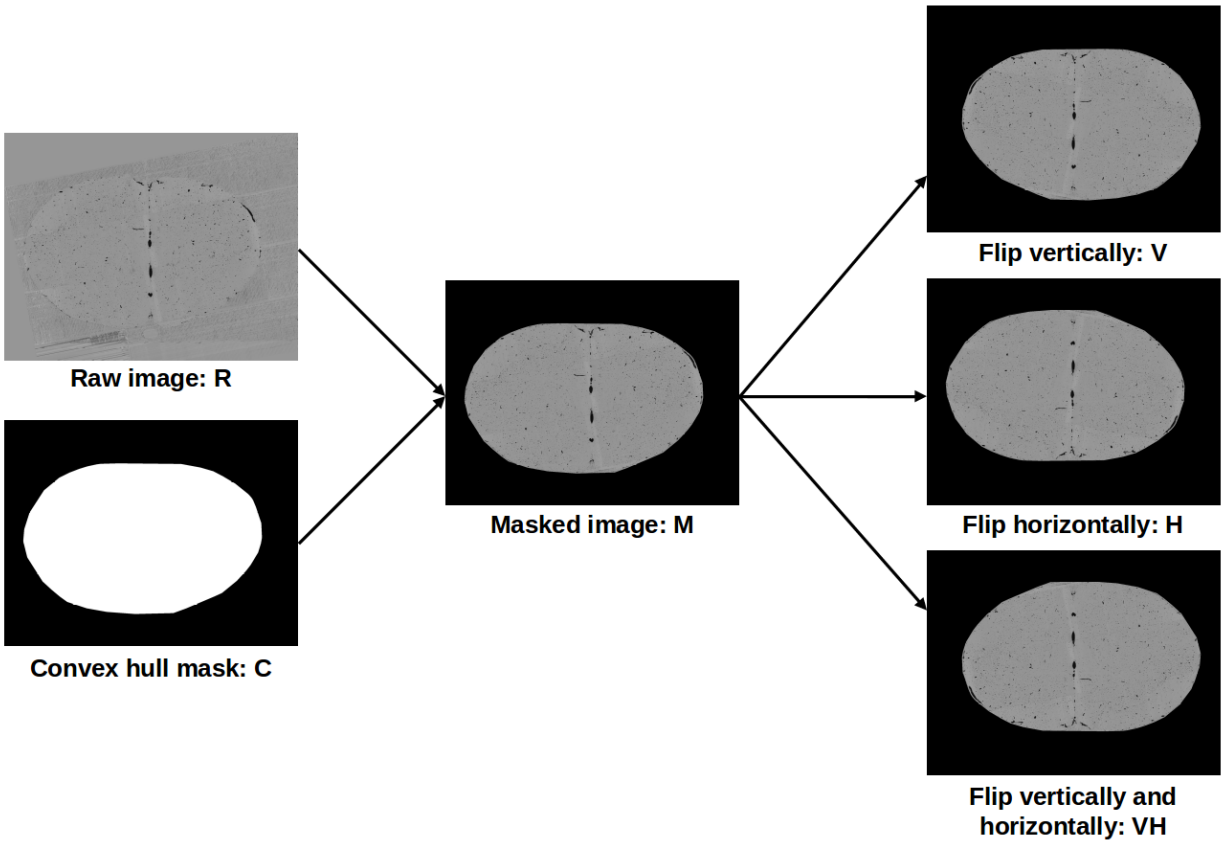

Figure 6.9: **Dataset for the Convolutional Neural Network with convex hull and data augmentation methods.** Masked image (M) is made by covering Convex hull mask (C) on raw image (R), and (V, H, and VH) are created by horizontal and vertical rotation. After the preparation process, the 8,142 raw KESM images becomes 32,568 images that is sufficient for training and testing.

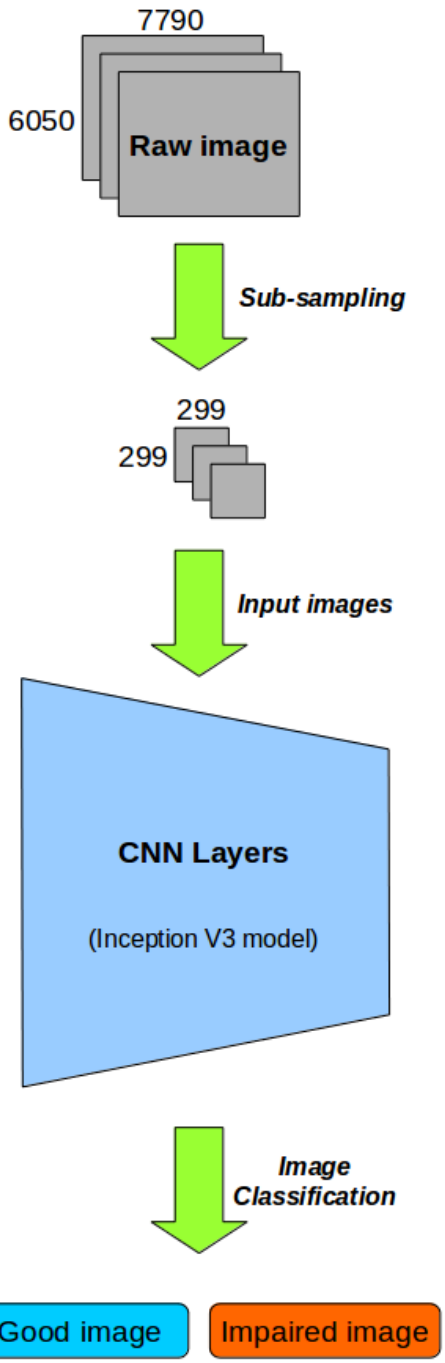

Figure 6.10: **Tracing of the Convolution Neural Network with KESM data set for the impaired image classification.** The Inception V3 model is utilized for the CNN architecture. The architecture consists of 5 convolutional layers and 2 pooling layers. For the input images of the CNN, the images from the preparation precess (Figure 6.9) with the resolution of 7790 $\times$ 6050 are sub-sampled to the images with the resolution of 299 $\times$ 299. The labels of the images ("good" or "impaired") are provided. Adapted from [48].

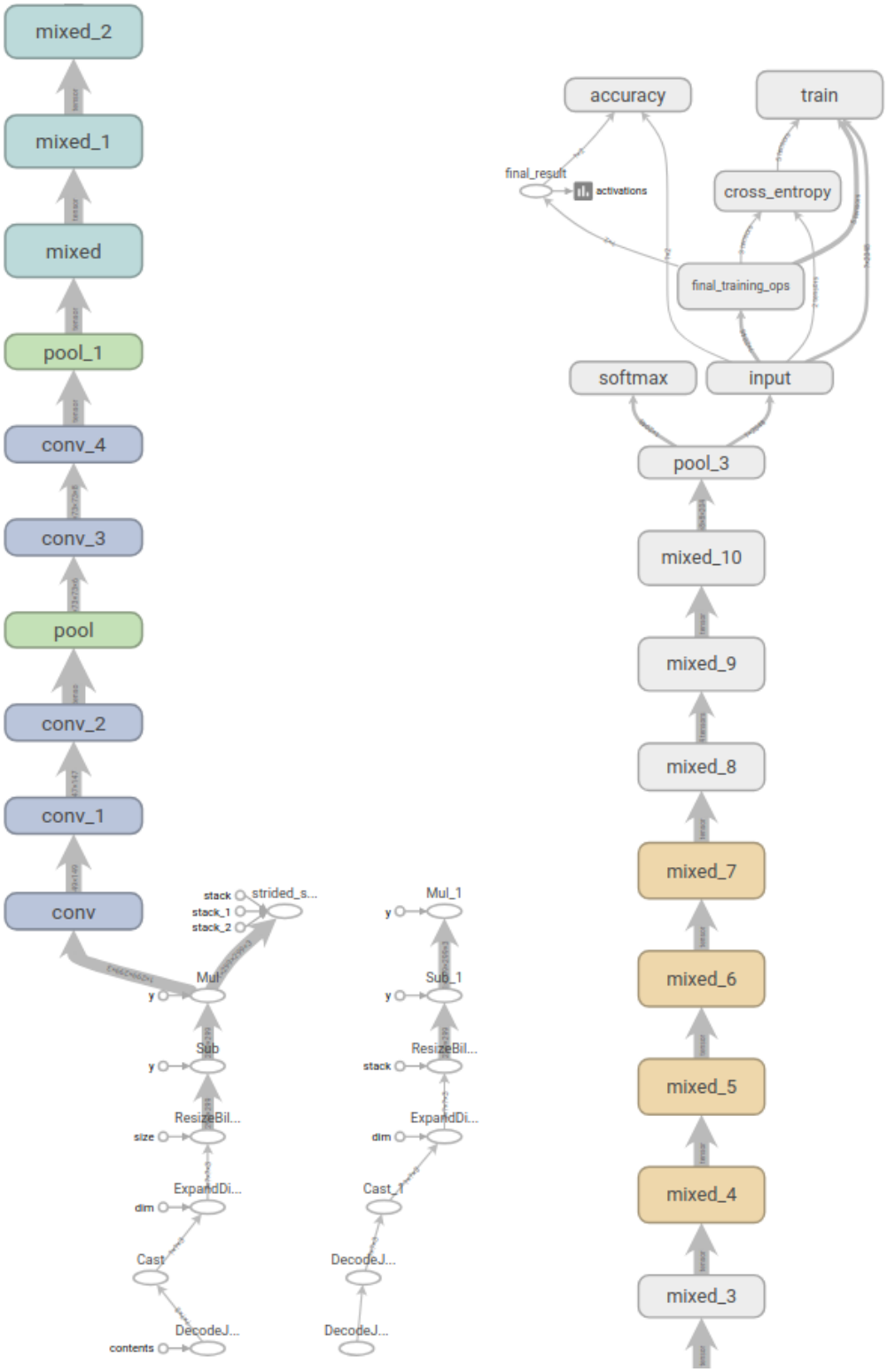

Figure 6.11: **Computational graph of Inception V3 model as visualized using TensorBoard.** The architecture consists of 5 convolutional layers and 3 pooling layers.

Experiments

The Inception V3 model was trained using an AMD FX (tm) -8320 CPU (Eight-Core, 3.5 GHz) and a GeForce GTX TITAN X GPU (12 GB). I utilized the TensorFlow [2] framework for the implementation of the experiments. Figure 6.11 is a computational graph of Inception V3 as visualized using TensorBoard. (TensorBoard is a visualization tools provided by TensorFlow.) The graph architecture consists of 5 convolutional layers and 3 pooling layers. After training the Inception V3 model, I got the accuracy value (Equation. 6.1) [67], and I can obtain true positive (TP), true negative (TN), false positive (FP), and false negative (FN) values through evaluation analysis (comparison of ground truth and experiment results).

Figure 6.12 is the confusion matrix. If the actual good image is a good image in the predicted result, it is true positive (TP). If the real impaired image is a impaired image, it is true negative (TN). False negative (FN) is a good image misclassified as an impaired image in the predicted result, and false positive (FP) is an impaired image misclassified as a good image in the predicted result.

		Ground truth	
		Good	Impaired
Predicted result	Good	True positive (TP)	False positive (FP)
	Impaired	False negative (FN)	True negative (TN)

Figure 6.12: **Confusion matrix.** If the actual good image is a good image in the predicted result, it is true positive (TP). If the real impaired image is a impaired image, it is true negative (TN). False negative (FN) is a good image misclassified as an impaired image in the predicted result, and false positive (FP) is an impaired image misclassified as a good image in the predicted result.

In addition, other features (Precision, Recall, and F1 score [67].) for performance evaluation were obtained by referring to the following equations.

$$\text{Accuracy} = \frac{TP + TN}{TP + TN + FP + FN} \tag{6.1}$$

$$\text{Precision} = \frac{TP}{TP + FP} \tag{6.2}$$

$$\text{Recall} = \frac{TP}{TP + FN} \tag{6.3}$$

$$\text{F1 score} = 2 \times \frac{Precision \times Recall}{Precision + Recall} \tag{6.4}$$

Results and analysis

Figure 6.13, Figure 6.14, and Figure 6.15 show the training curve (4,000 (default), 8,000, and 12,000 iterations) for the CNN model, where the accuracies and cross entropies (a loss function that shows the progress of the learning.) of the train and validation set were plotted (orange: train, blue: validation). As the training iteration increases, the accuracy value gradually increases and the cross entropy value gradually decreases.

Table. 6.1 shows the performance evaluation results of the image classification ("good" or "impaired") accuracy, precision, recall, and F1 score of the trained CNN and SVM models. The CNN model shows higher accuracy, precision, and F1 score than the SVM, which indicates that the approach using CNN is better for classifying the impaired image data obtained from a serial sectioning process such as the KESM dataset. In the CNN model, when the training repetition value is set to 12,000, the corresponding values (accuracy, precision, recall, and F1 score) are not significantly changed comparing to the training iteration value of 8,000. The performance

evaluation graph of the image classification result is shown in Figure 6.16, and the difference can be easily recognized.

There is room for improvement with the accuracy of 90%. Actually, even for a human, some images are too ambiguous to be labeled as good or impaired. Therefore, as a future work, I plan to utilize the CNN model developed recently to improve image classification accuracy.

I randomly selected and categorized image data for training (80%) and testing (20%). However, if I selected a specific part of the image data (the anterior and posterior of the brain in Figure. 7.5) for training (80%) and testing (20%), then the accuracies were about 61% and 87% respectively (Table. 6.2).

This chapter presented the CNN based method for classifying good and impaired images automatically. The CNN based model showed better accuracy than the baseline model SVM on the random dataset. I expect that this method could be of great help in screening damaged or impaired images in future KESM datasets.

Table 6.1: Performance evaluation of SVM and CNN (%). Adapted from [48].

	Support Vector Machine	Convolutional Neural Network		
		4,000	8,000	12,000 (training iterations)
Accuracy	88.60	90.79	91.54	91.39
Precision	89.30	95.86	96.76	96.76
Recall	97.97	92.88	92.70	92.70
F1 score	93.43	94.35	94.69	94.69

Table 6.2: Performance evaluation of CNN with a specific part of the image data (%)

	Anterior of the brain data	Posterior of the brain data
Accuracy	61.07	87.18
Precision	94.29	95.16
Recall	57.09	89.39
F1 score	71.12	92.19

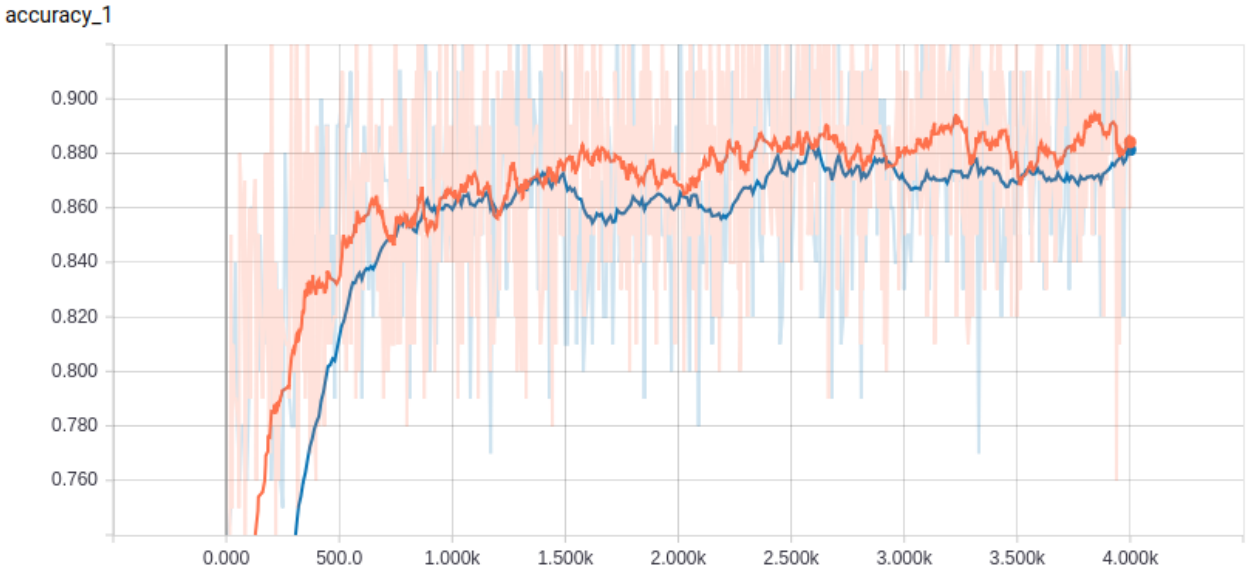

(a) Accuracy curve

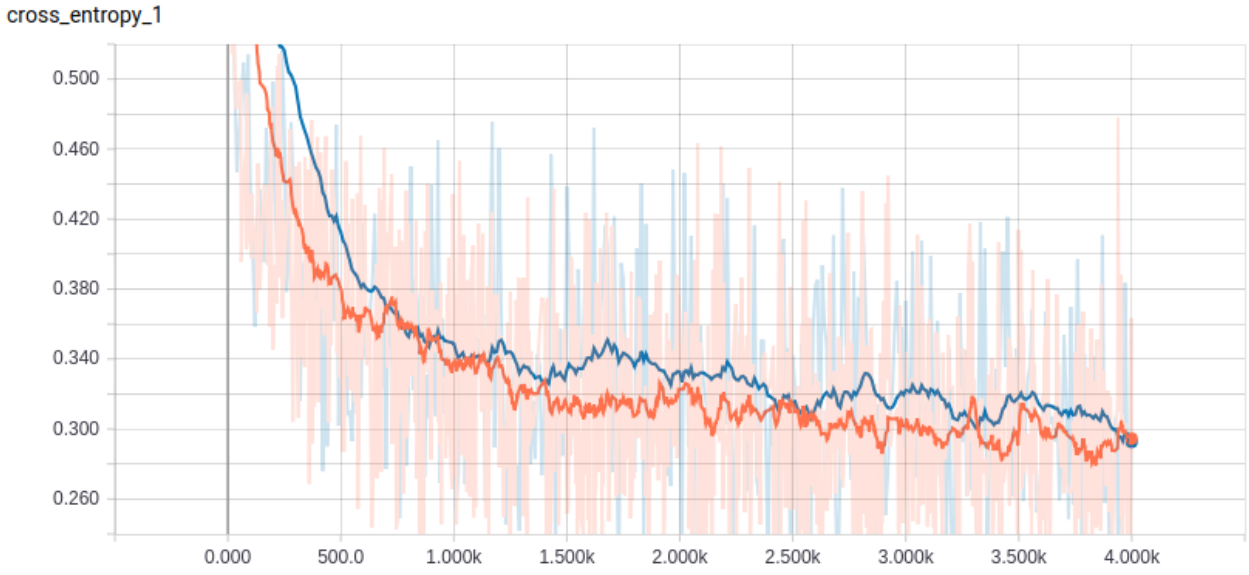

(b) Cross entropy curve

Figure 6.13: **Training curve of the CNN model with 4,000 training iterations.** The accuracy and cross entropy change during training is shown. The light colored traces in the back represent mean standard deviation. (Orange: train, Blue: validation). Adapted from [48].

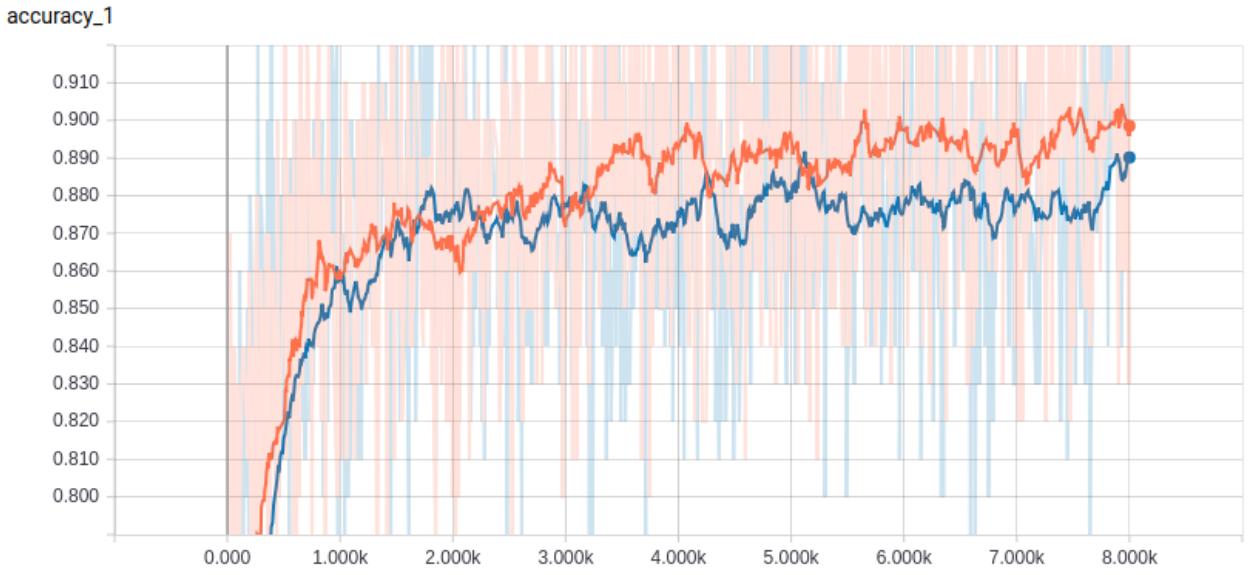

(a) Accuracy curve

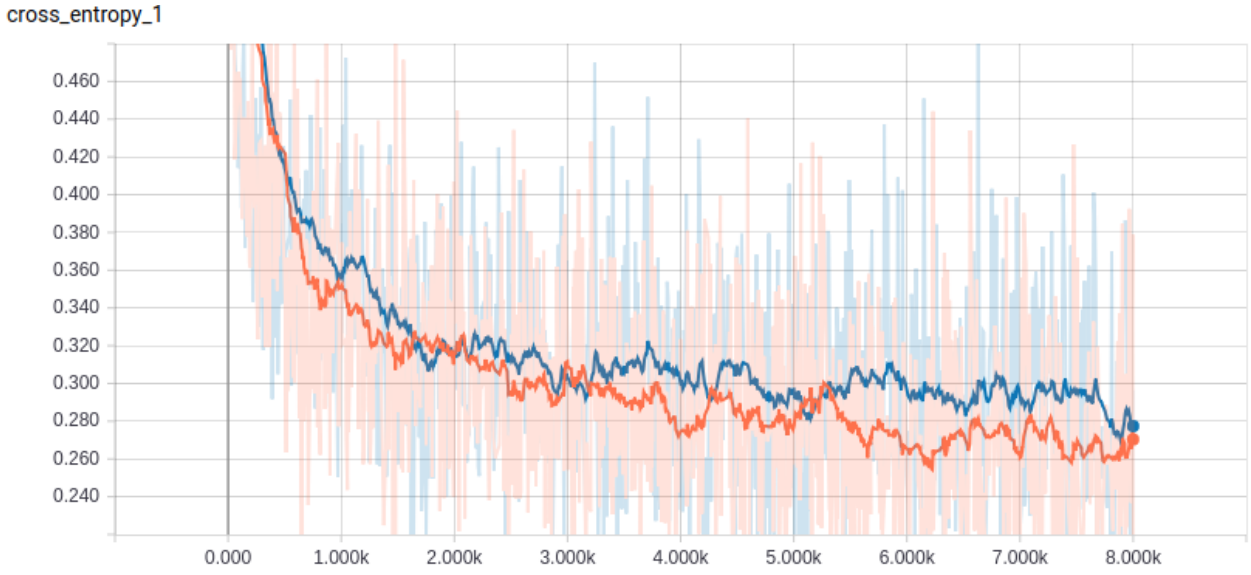

(b) Cross entropy curve

Figure 6.14: **Training curve of the CNN model with 8,000 training iterations.** The accuracy and cross entropy change during training is shown. The light colored traces in the back represent mean standard deviation. (Orange: train, Blue: validation)

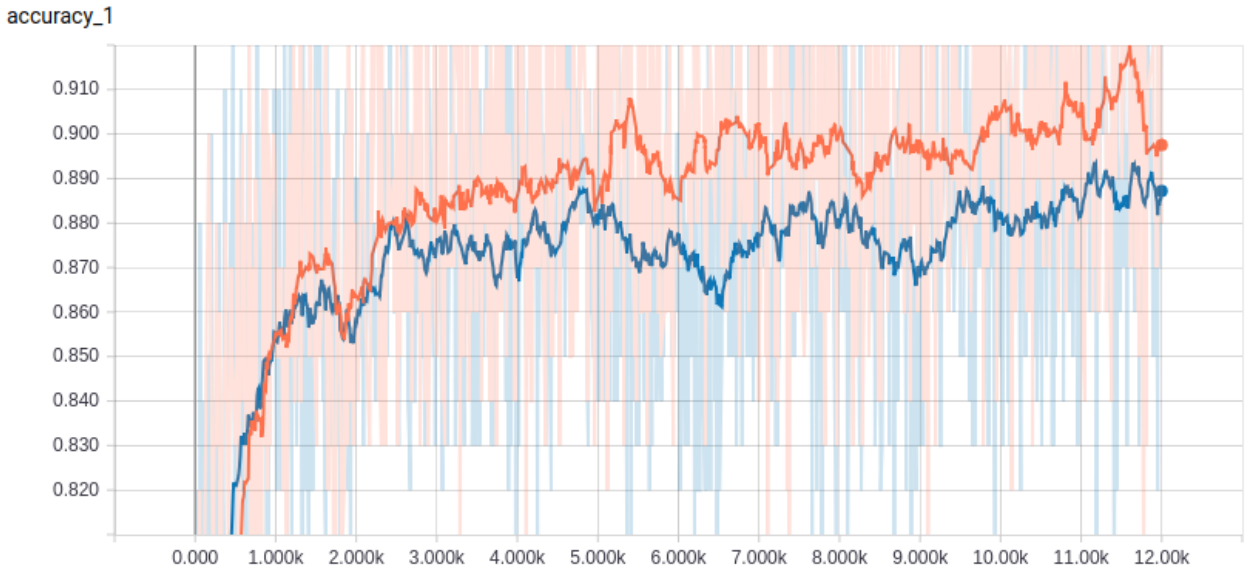

(a) Accuracy curve

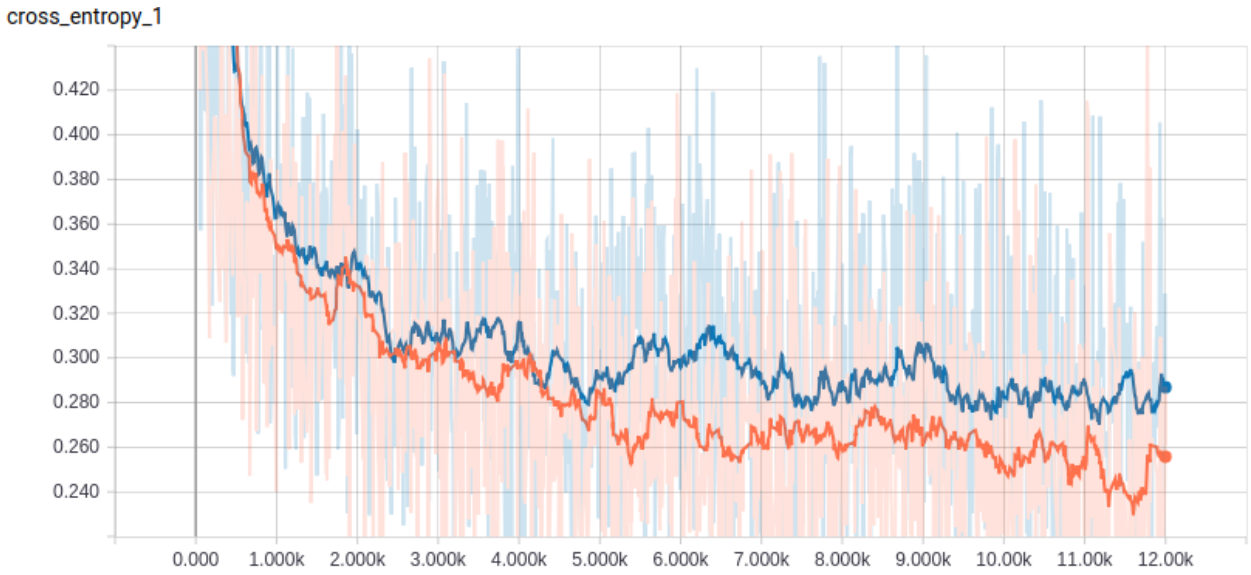

(b) Cross entropy curve

Figure 6.15: **Training curve of the CNN model with 12,000 training iterations.** The accuracy and cross entropy change during training is shown. The light colored traces in the back represent mean standard deviation. (Orange: train, Blue: validation)

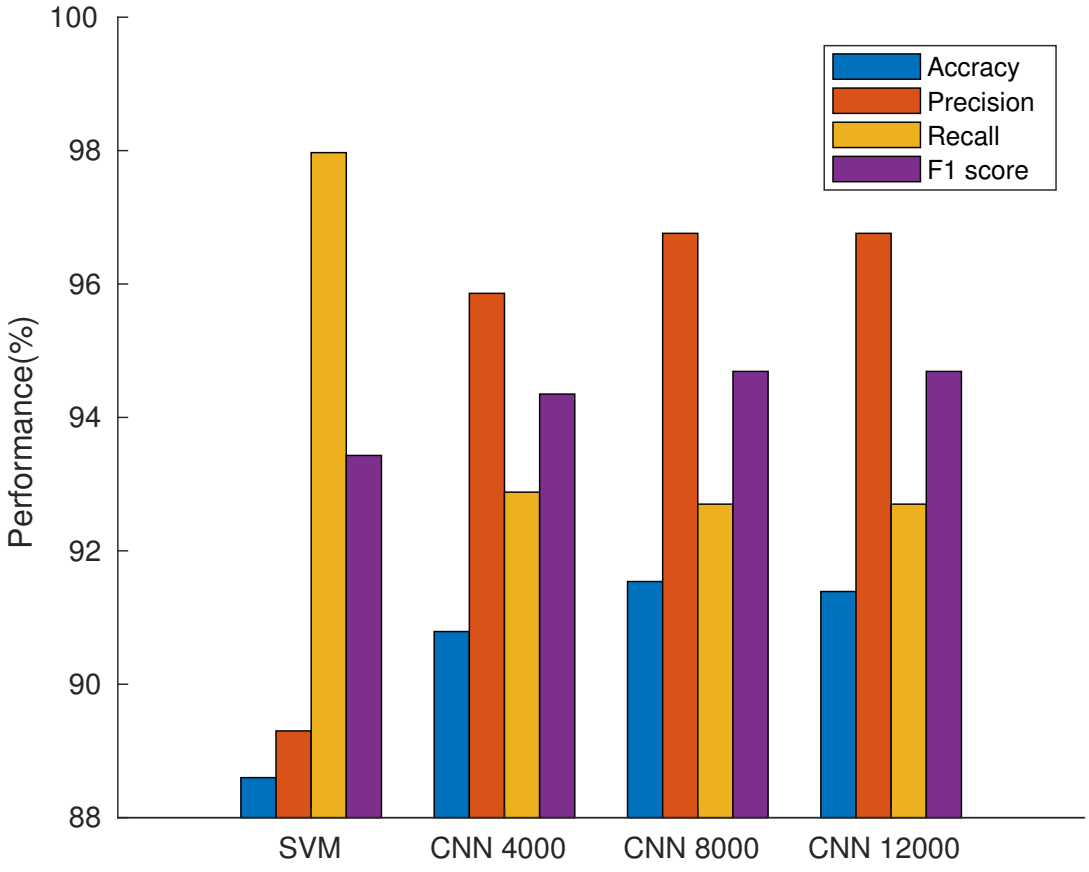

Figure 6.16: **Performance evaluation of SVM and CNN.** The performance evaluation graph of the image classification result is shown, and the difference can be easily recognized.

COMPARISON OF RESULTS TO DATA FROM THE LITERATURE.

In this dissertation, I reconstructed the vascular structure of the whole mouse brain in 3D, traced the vessel, and conducted of geometric analysis using the results obtained in the process. In order to verify these results, it is necessary to analyze and compare the results with previous studies. First, I compared the results of measurements of the quantity of blood vessels in the mouse brain.

Zhang $et\ al.$ [51] applied the optimized CLARITY protocol [99] to quantify blood vessels in the mouse brain. CLARITY [16] is a method to make brain tissue transparent. Figure 7.1a shows how the whole adult mouse brain can be made transparent. After the CLARITY method, the mouse brain is subjected to a step of extracting and analyzing the image using confocal scanning microscopy. Figure 7.1b describes the visualization and quantification of the vessels network in the sham and tMCAO (transient middle cerebral artery occlusion) mouse brain coronal section, and the quantification of the blood vessels is about 0.8% of the mouse brain coronal section ($504\,\mu\mathrm{m}\times504\,\mu\mathrm{m}\times886\,\mu\mathrm{m}$ voxel dataset, tMCAO case is not considered).

3Scan, a starting company, partially analyzed the quantification of blood vessels in the mouse brain using data obtained using their own implementation of KESM [72]. Figure 7.2A shows 3Scan's KESM that consists of (1) the knife arm assembly, (2) the optics train and sensor, and (3) the water bath and stages. Figure 7.2B shows the sagittal view of mouse brain. Figure 7.2c and Figure 7.2D are the subregions samples of the forebrain and the cerebellum (gray: microvasculature, red: skeleton). Figure 7.2c and Figure 7.2D used $512\,\mu\mathrm{m}\times512\,\mu\mathrm{m}\times72\,\mu\mathrm{m}$ voxels dataset ($0.7\,\mu\mathrm{m}\times0.7\,\mu\mathrm{m}\times5.0\,\mu\mathrm{m}$ resolution). The quantification of blood vessels measured were 1.07% (forebrain) and 3.18% (cerebellum), respectively.

Wu $et\ al.$ [94] applied a 3D dataset of a whole mouse brain (three male mice, C57BL/6) used to simultaneously visualize the cells and blood vessels. Figure 7.3a is a simultaneous cross-section of

(a) CLARITY method.

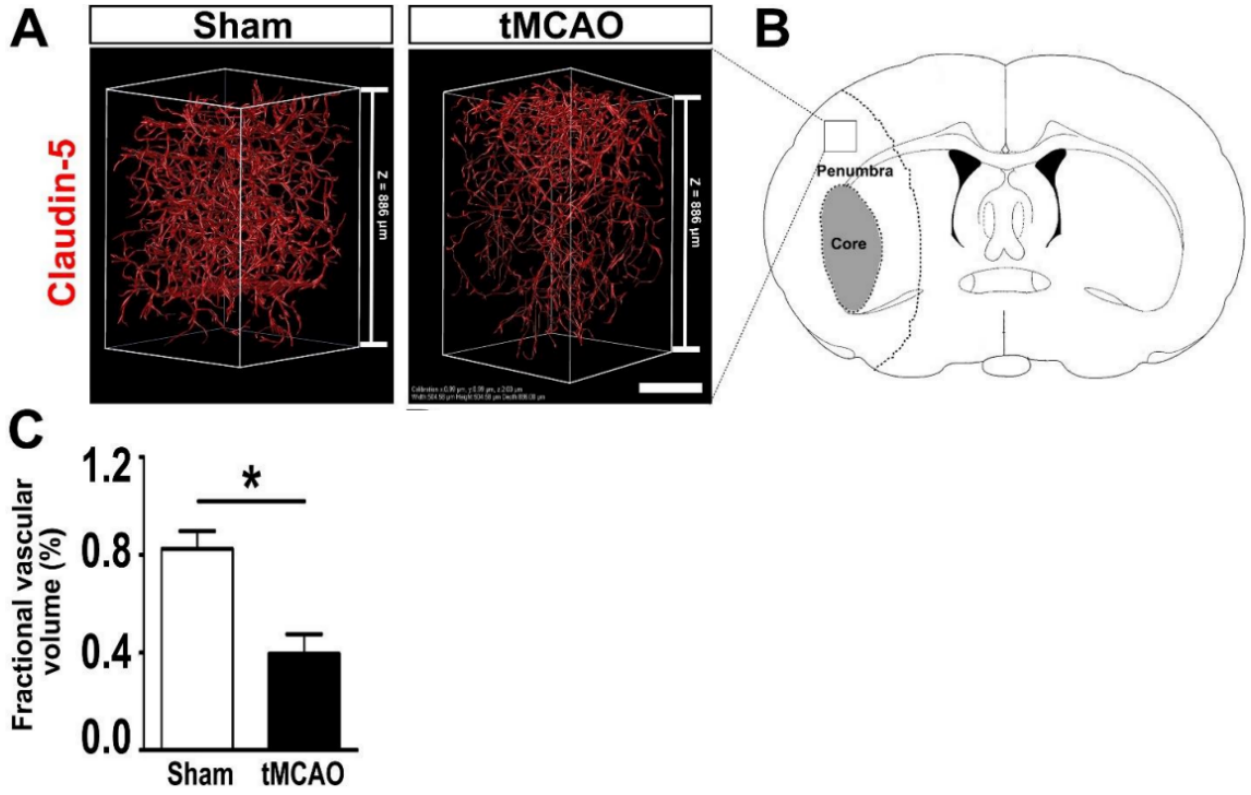

(b) Visualization and quantification of the vessels network in the sham and tMCAO mouse brain.

Figure 7.1: **CLARITY method, visualization, and quantification of the vessels network in the sham and tMCAO mouse brain coronal section.** (a) shows how the whole adult mouse brain becomes transparent. (b) is the visualization and quantification of the vessels network in the sham and tMCAO (transient middle cerebral artery occlusion) mouse brain coronal section. $504\,\mu\text{m}\times504\,\mu\text{m}\times886\,\mu\text{m}$ voxel dataset ($0.99\,\mu\text{m}\times0.99\,\mu\text{m}\times2.0\,\mu\text{m}$ resolution). Scale bar=1mm. Adapted from [51].

cells and blood vessels with $30\,\mu\mathrm{m}$ thickness of posterior direction of the mouse brain. Figure 7.3b shows an enlarged view of the cortical region indicated by the white box in Figure 7.3a. Figure 7.3c describes a quantity of microvascular volume by cortical depth in Figure 7.3b (I, II/III, IV, V, and VI). The red, green and blue curves point to the agranular cortex (M1), the granular (PMBSF) and partially granular cortex (V1), respectively, and the translucent regions indicate the standard deviations. The quantification of microvascular volume measured about 0.4% to 1.6% in cortical regions of the mouse brain.

Figure 7.4 is the datasets for the quantification of blood vessels in the mouse brain (spinal cord, cerebellum, and neocortex). Table 7.2, shows the measurement results of spinal cord, cerebellum, and neocortex at 2.40%, 2.50%, and 1.40%, respectively.

I divided the whole mouse brain into 10 parts as shown in Figure 7.5, and the quantification of each microvascular volume was obtained as shown in Table. 7.1. The quantification of each microvascular volume ranges from 0.81% to 1.65%. I also cropped each dataset as shown in Figure 7.6 to obtain the fractional volume. Using the fractional volumes thus obtained, the results of the quantification of the vasculature in the mouse brain were obtained as shown in Table. 7.1. The quantification of each microvascular volume ranges from 1.03% to 2.62%.

In Table 7.2, I compared the result of the previous study (1.4% for the neocortex) [58] with my percentage of total volume result, and the value of the total with minimum threshold option was low. On the other hand, value (1.37%) using the Otsu's threshold option is similar to the previous study. This is due to the difference in threshold options applied when binarizing the data.

Figure 7.7 is a different cropped portions of the same dataset, and Table. 7.3 shows the quantification of vasculature in the fractional volumes. The distribution ranges from 1.75% to 2.74% depending on the cropped portions. It is possible to confirm that the quantification of the blood vessel varies depending on the cropped portions of the same dataset.

Second, I compared and analyzed the diameter of the cerebral blood vessels. In [101], they used synchrotron radiation to study cerebral vascular architecture in rats. The synchrotron radiation has a voxel size of $5.92\,\mu\mathrm{m}$. Figure 7.8 shows the 3D digitalized angioarchitertural map

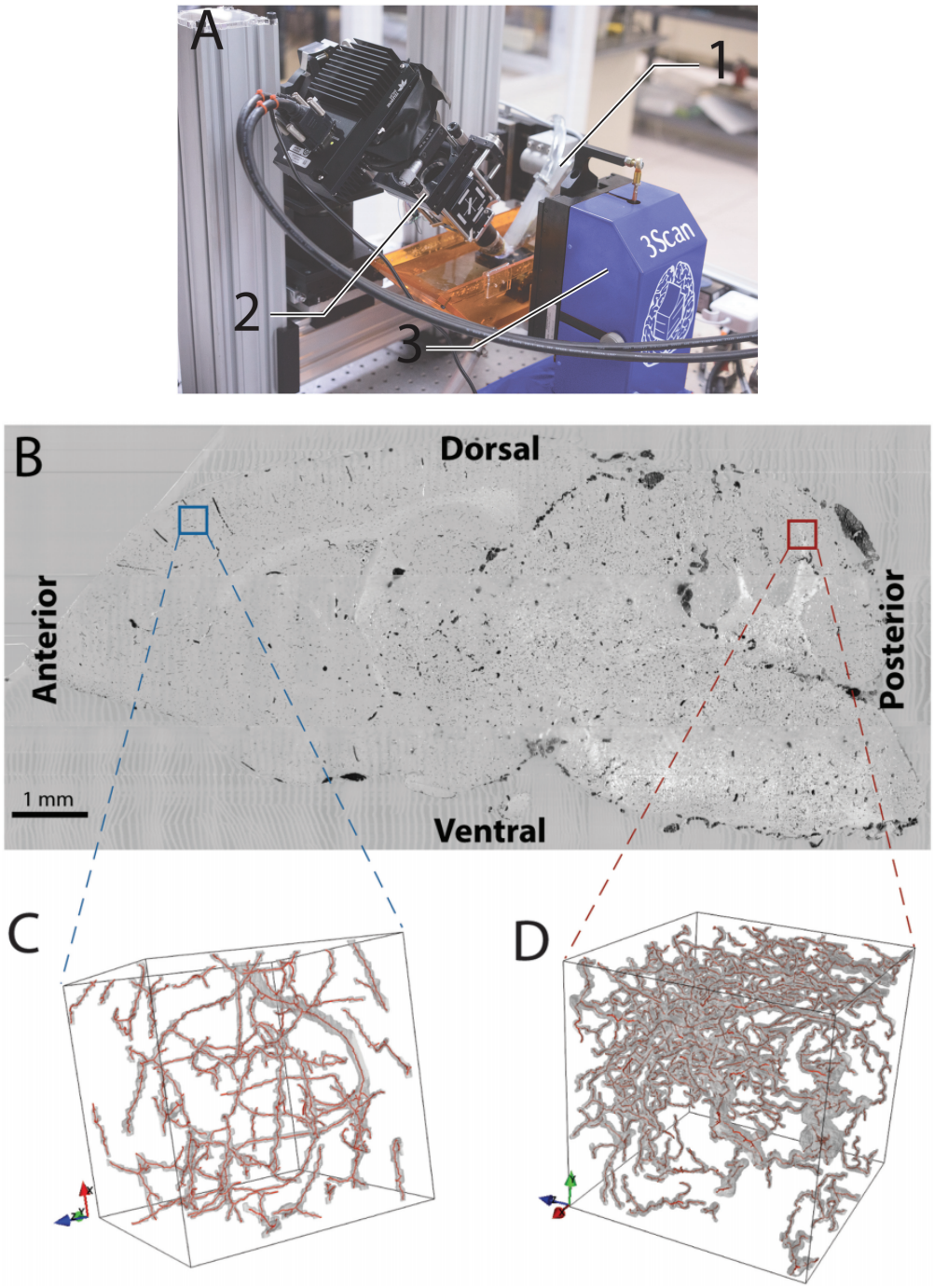

Figure 7.2: **The KESM by 3Scan and the subregion sample of interest in whole mouse brain vasculature.** (A) The KESM consists of (1) the knife arm assembly, (2) the optics train and sensor, and (3) the water bath and stages. (B) Sagittal view of mouse brain. (C) The subregion sample of the forebrain (gray: microvasculature, red: skeleton). (D) The subregion sample of the cerebellum. (C) and (D) used $512\,\mu\text{m}\times512\,\mu\text{m}\times72\,\mu\text{m}$ voxels dataset ($0.7\,\mu\text{m}\times0.7\,\mu\text{m}\times5.0\,\mu\text{m}$ resolution). Adapted from [72].

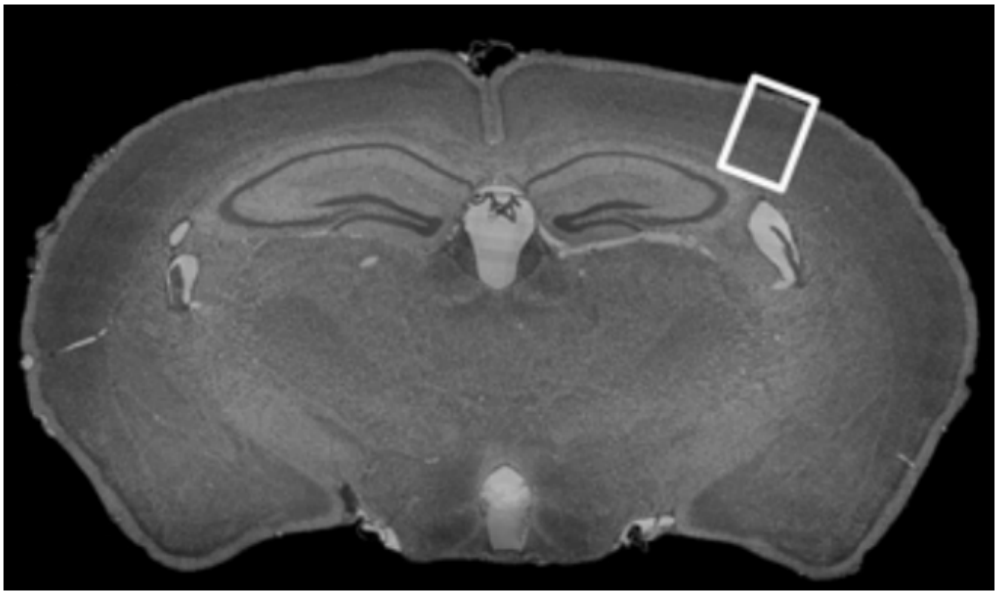

(a) Simultaneous cross-section of cells and blood vessels (thickness: $30\,\mu\mathrm{m}$, posterior direction)

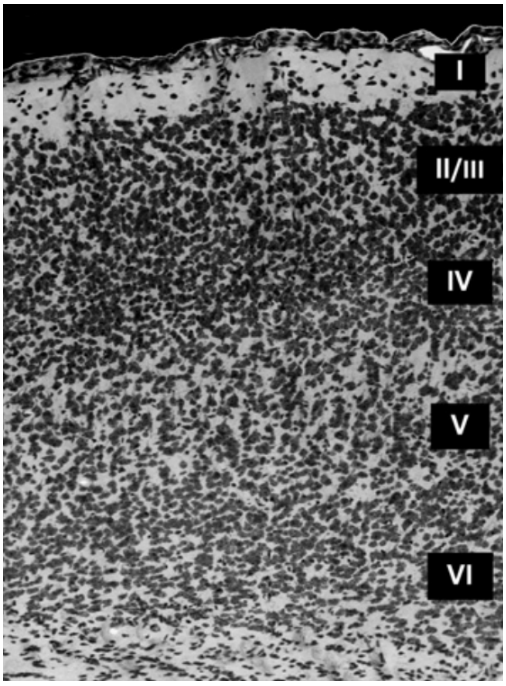

(b) Enlarged view of the cortical region indicated by the white box in (a).

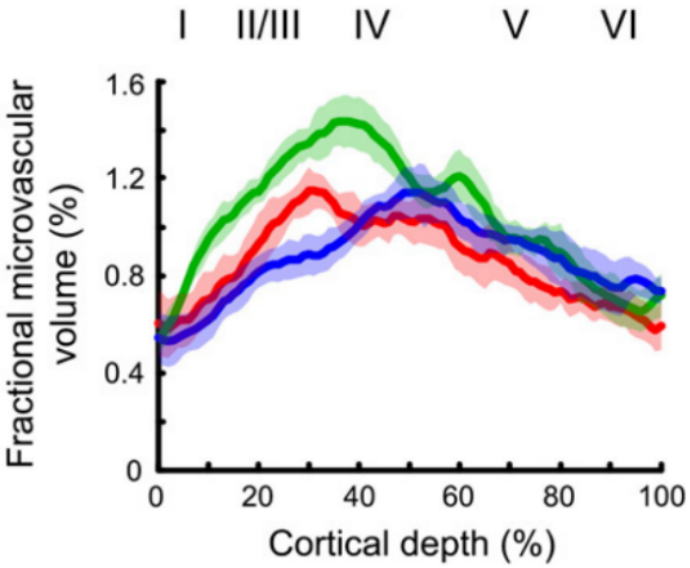

(c) Quantity of microvascular volume by cortical depth in (b).

Figure 7.3: **A dataset of a mouse brain and quantity of microvascular volume by cortical depth (three male mice, C57BL/6).** (a) Simultaneous cross-section of cells and blood vessels (thickness: $30\,\mu\mathrm{m}$, posterior direction). (b) Enlarged view of the cortical region indicated by the white box in (a). (c) Quantity of microvascular volume by cortical depth in (b). The red, green and blue curves point to the agranular cortex (M1), the granular (PMBSF) and partially granular cortex (V1), respectively, and the translucent regions mean the standard deviations. $600\,\mu\mathrm{m}\times600\,\mu\mathrm{m}\times920\,\mu\mathrm{m}$ voxels dataset ($0.4\,\mu\mathrm{m}\times0.35\,\mu\mathrm{m}\times1.0\,\mu\mathrm{m}$ resolution). Adapted from [94].

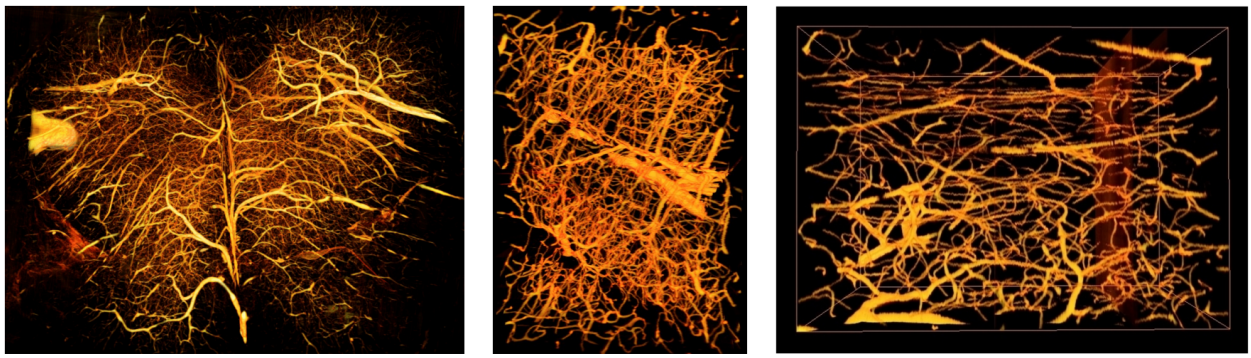

(a) (b) (c)

Figure 7.4: **The datasets of a mouse brain (earlier KESM study).** (a) Spinal cord. (b) A capillary network in the cerebellum. (c) A capillary network in the neocortex. $512\,\mu\text{m}\times512\,\mu\text{m}\times512\,\mu\text{m}$ voxels dataset ($0.6\,\mu\text{m}\times0.7\,\mu\text{m}\times1.0\,\mu\text{m}$ resolution). Adapted from [56].

and distribution of blood vessel diameter size of the whole rat brain. Figure 7.8b describes the distribution percentage of blood vessel diameter size of the whole rat brain. They mentioned approximately 90% of the blood vessels are smaller than $30\,\mu\mathrm{m}$ in diameter. Similar results can be seen in Figure 5.11b, where the distribution of blood vessel size smaller than 30 micrometers in diameter is approximately 99%.

In conclusion, I can confirm that the results of the above-mentioned studies are included in the category of blood vessel quantification in the whole mouse brain I obtained. The differences in the quantification results of the blood vessels are considered to be different depending on the cropped position, volume voxel size, and image resolution. Of course, there are differences between mouse and rat datasets, but my results can prove that my dataset is abundant in smaller-sized cerebrovascular information. Furthermore, I also can quickly obtain the quantification of each microvascular volume at the desired region of the mouse brain.

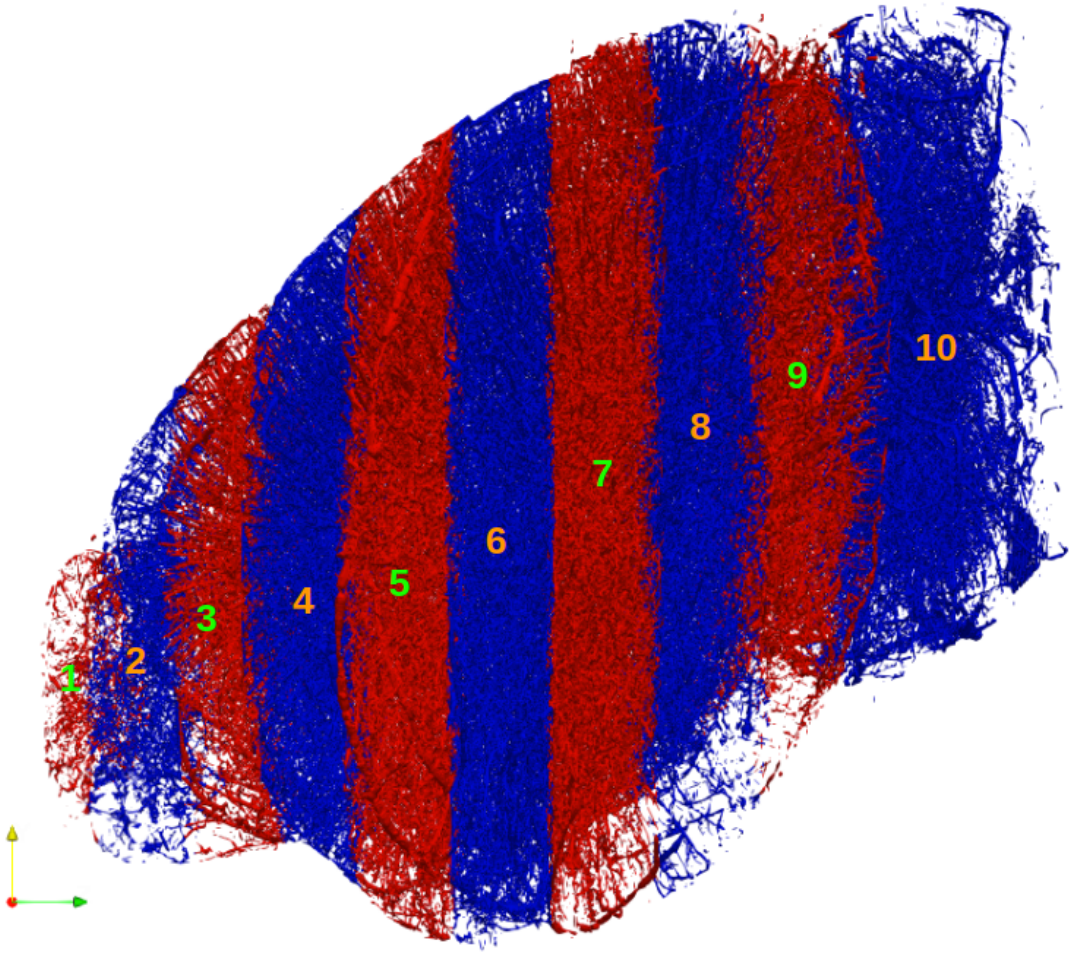

Figure 7.5: **A whole mouse brain divided into 10 parts.** Anterior to posterior was divided into 10 parts. The last posterior part (blue) consists of 234 images, and the remaining 9 parts consist of 200 images. (←: Anterior, →: Posterior)

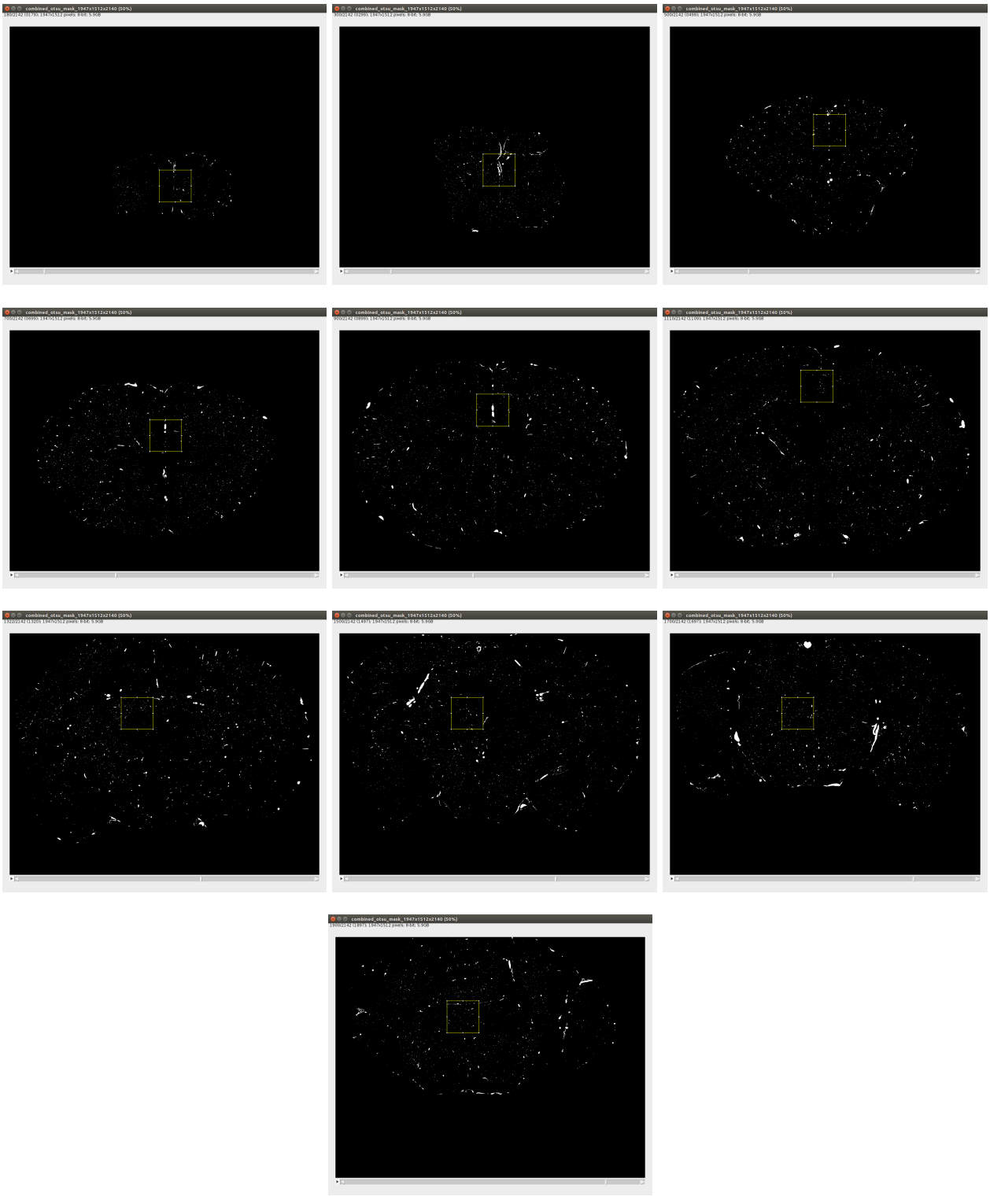

Figure 7.6: **Cropped portion of each dataset.** Left-to-right, top-to-bottom shows the cropped portion (yellow square) of each dataset. ($200\,\mu m \times 200\,\mu m \times 200\,\mu m$ voxel dataset ($4.8\,\mu m \times 5.6\,\mu m \times 4.0\,\mu m$ resolution).

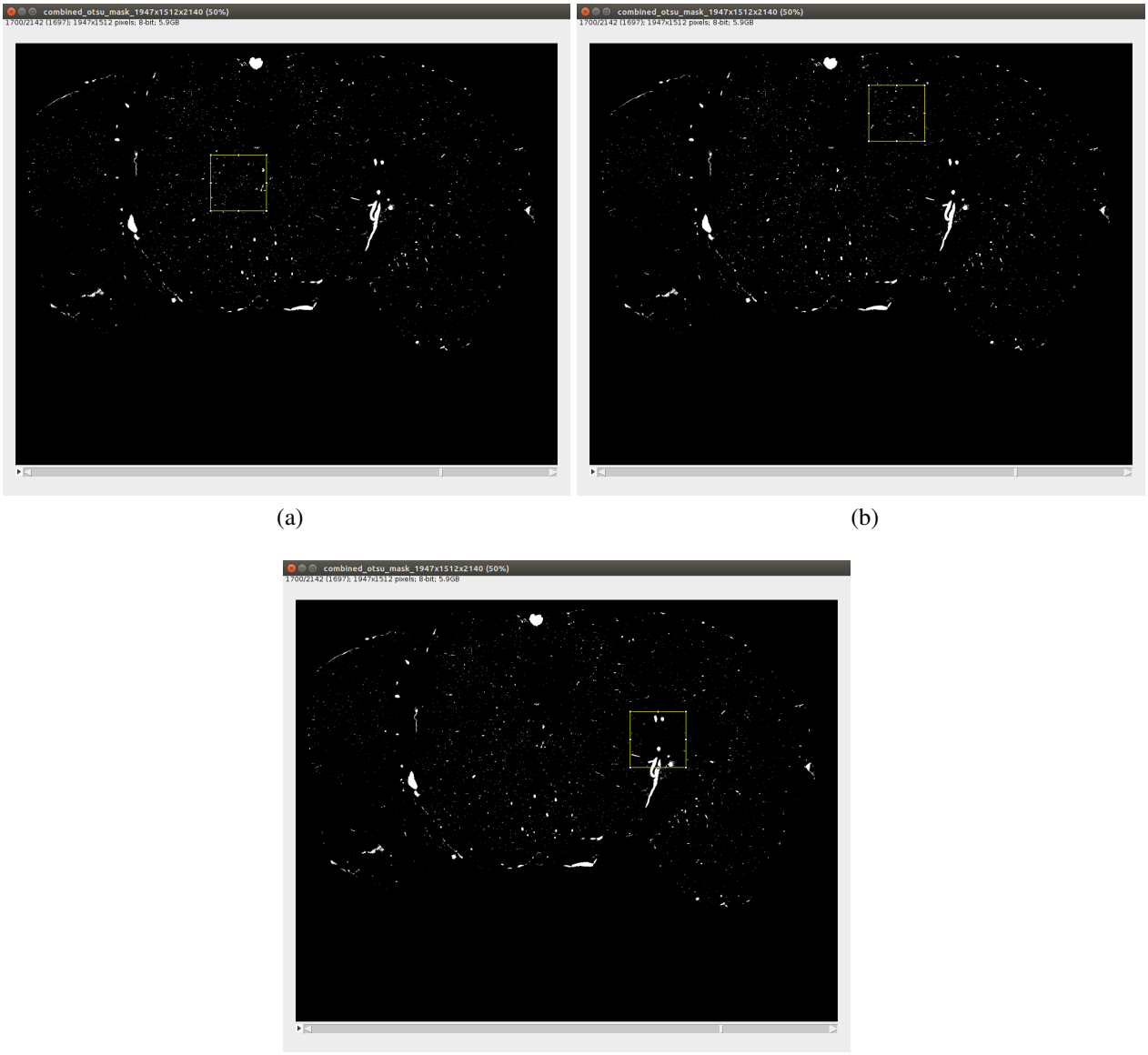

(a) (b)

(c)

Figure 7.7: **Different cropped portions of the same dataset (part 9).** $200\,\mu m \times 200\,\mu m \times 200\,\mu m$ voxel dataset ($4.8\,\mu m \times 5.6\,\mu m \times 4.0\,\mu m$ resolution).

Table 7.1: Analysis of quantity of microvascular network (% of total)

Parts	Volume for each part (Figure 7.5)	Fractional volume (Figure 7.6)
1	0.81	1.34
2	1.21	2.62
3	1.13	1.55
4	1.39	2.32
5	1.23	1.03
6	1.22	1.83
7	1.47	1.10
8	1.17	1.20
9	1.49	1.75
10	1.65	1.53

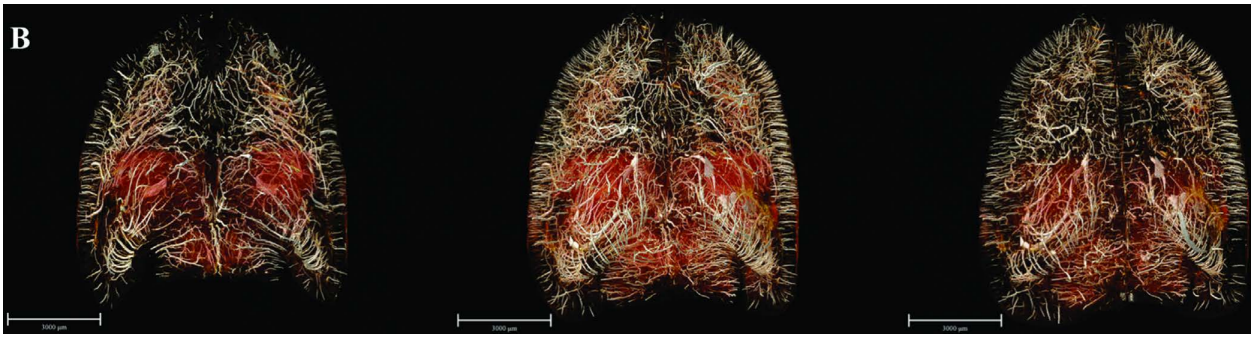

(a) Whole rat brain maps

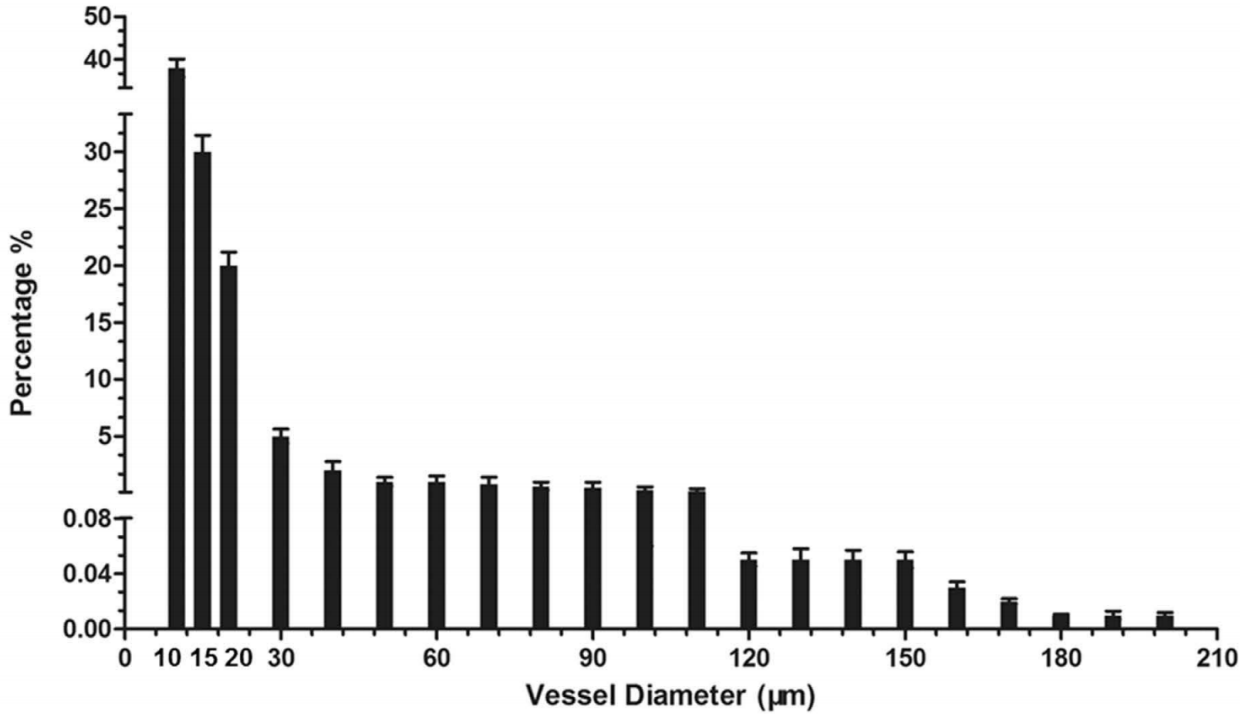

(b) Distribution of blood vessel diameter size

Figure 7.8: **3D digitalized angioarchitertural map and distribution of blood vessel diameter size of the whole rat brain.** (a) The horizontal view of the whole rat brain with the 3D reconstructed (200 serial slice-by-slice respectively). Sclae bar: $3000\,\mu\mathrm{m}$. (b) Distribution percentage of blood vessel diameter size of the whole rat brain. Adapted from [101].

Table 7.2: Analysis of total microvascular network. Adapted from [48].

	3D (whole)		Mayerich's [56] ($512\,\mu m \times 512\,\mu m \times 512\,\mu m$)		
	Minimum	Otsu's	Spinal Cord	Celebellum	Neocortex
Volume (% of total)	0.71	1.37	2.40	2.50	1.40

Table 7.3: Analysis of quantity of different cropped portions of the same dataset

	Figure 7.7a	Figure 7.7b	Figure 7.7c
Volume (% of total)	1.75	1.92	2.74

DISCUSSION AND CONCLUSION

In Chapter. 5, I divided the dataset into 10 parts to obtain the results of the blood vessel tracing for the whole mouse brain and combined each of the results into one. There are some cases in which the tracing results of the blood vessels are well connected as shown in Figure. 8.1a. However, some parts of the blood vessels that are not completely connected as shown in Figure. 8.1b. I need a stitching method for partly traced vasculature results to be connected while considering the starting and ending points in future work. Another way to obtain the tracing results is to get the tracing results of the whole brain blood vessels at once, using a further subsampled data set. Figure. 8.2 shows the tracing results obtained at once. The tracing results for visualization can be obtained in a single file, but for geometric analysis, I still need to split the dataset and analyze the partial results.

The future works can be summarized as follows. (1) Topological analysis of the reconstructed vascular network. (2) Stitching 11 vascular tracing results into one while considering the starting and ending points. (3) Analyzing the results by applying different models of CNN architecture. (4) Making a dataset using more sophisticated threshold method. (better than Otsu's)

In my dissertation, to build and analyze the full structure of the whole mouse brain at submicrometer resolution, I have to complete four goals. (1) For preparing a whole mouse brain dataset, I proposed an axial direction sub-sampling method, where averaging consecutive image pairs and replacing significant degraded images with a blank image were used. The resulting sub-sampled images are greatly reduced in size for visualizing and analyzing, but retain more information than sub-sampled images from other sub-sampling methods. In addition, I proposed a convex hull masking method to automatically detect the boundary of the mouse brain and eliminate unnecessary information (including noise) outside of the region of interest (ROI). This method allows me to use a more aggressive threshold option, which results in more abundant vascular information. As a result of image processing and convex hull mask methods, the raw image at 7790×6050 resolution was downsized to 1947×1512 resolution, and through the two step process of combining

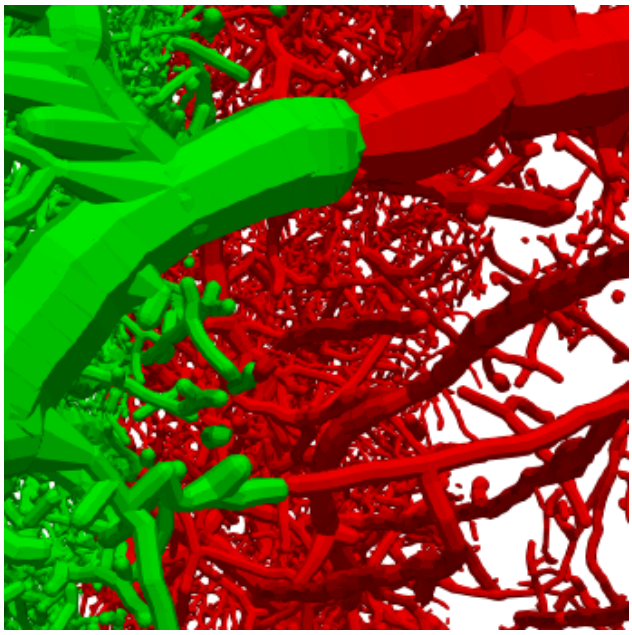

(a) A well-connected image.

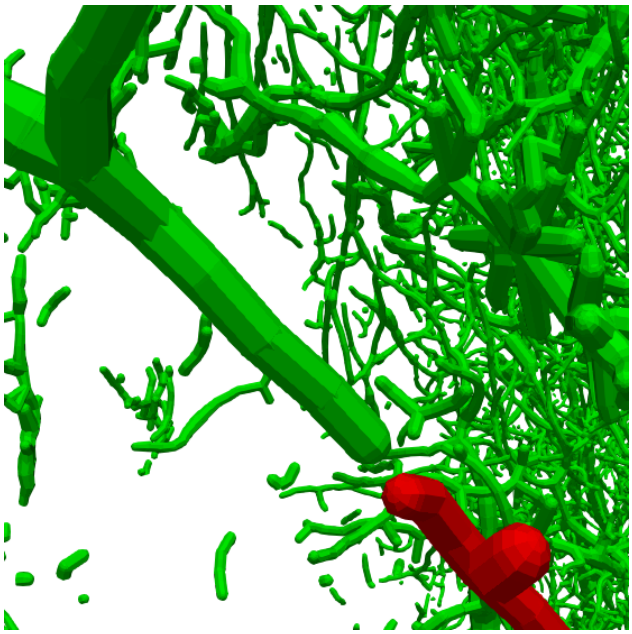

(b) An incomplete connection image.

Figure 8.1: **Traced vasculature results near the boundary of two data sets (6 and 7 in Figure. 7.5).** (a) shows a well-connected image. (b) shows an incomplete connection image.

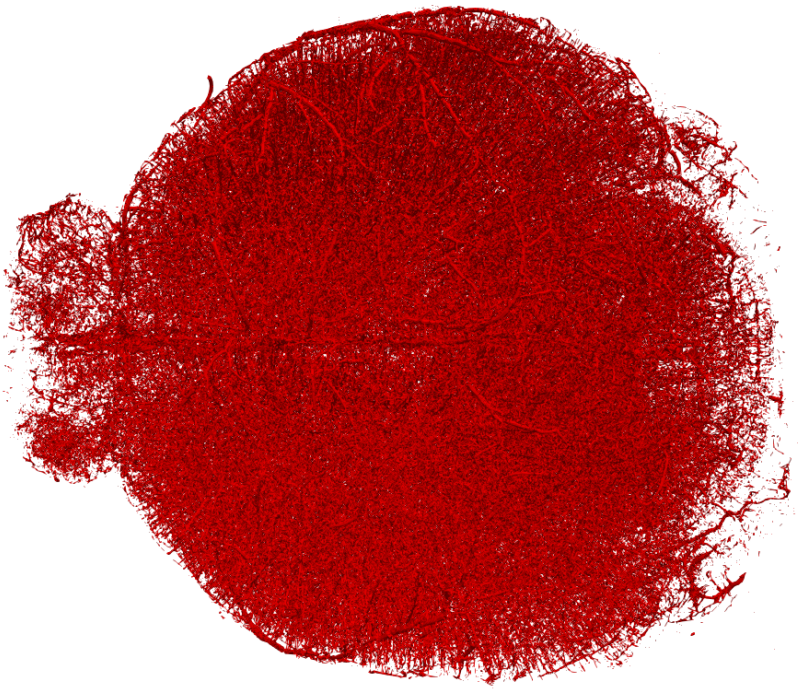

(a) Horizontal view (←: Anterior, →: Posterior)

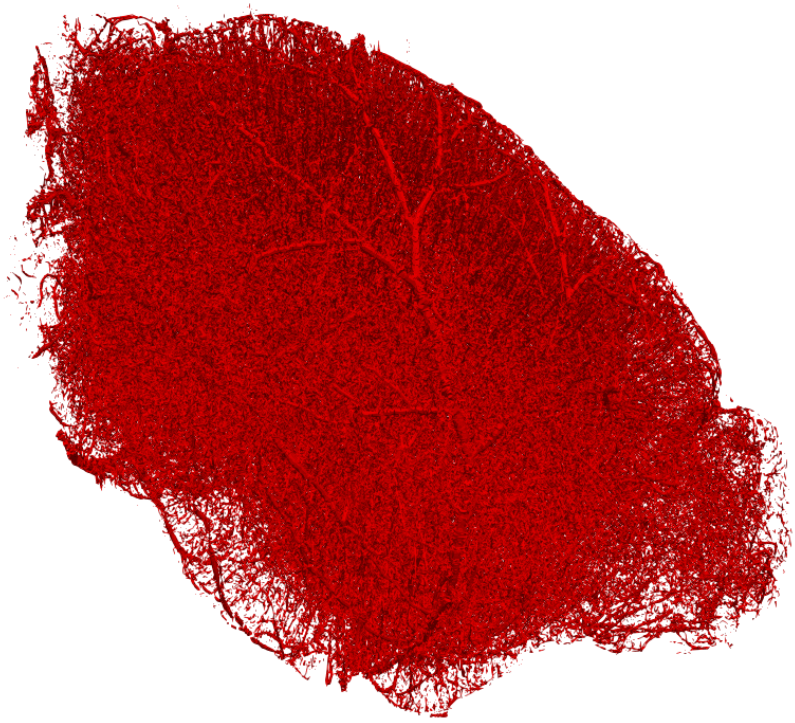

(b) Sagittal view (←: Posterior, →: Anterior)

Figure 8.2: **Network tracing results of a whole mouse brain vasculature at submicrometer resolution.** (a) and (b) are the microvascular tracing results of the whole mouse brain restored with the ParaView software. I was able to obtain one VTK file as a result of tracing the entire cerebral vessels.

two consecutive images $8,460$ raw images were rebuilt into a $2,140$ dataset.

(2) For measuring and categorizing by the vascular diameter of the KESM dataset from goal (1), I calculated the diameters of the mouse brain vessels in the sections images and categorized them according to the diameter sizes (capillaries: $Diameter \leq 10.4 \pm 0.8\mu m$, medium-sized vessels: $10.4 \pm 0.8\mu m < Diameter \leq 20.8 \pm 1.6\mu m$, large-sized vessels: $20.8 \pm 1.6\mu m < Diameter \leq 41.6 \pm 3.2\mu m$, and veins and arteries: $Diameter > 41.6 \pm 3.2\mu m$). Then, for tracing, the center lines were extracted by connecting the center points of two vessels if their cross-sectional regions are connected in consecutive slices along the z-axis. The distribution of the vessels along with different diameter sizes were visualized and analyzed using the centerlines and diameters.

(3) For 3D tracing and geometric analysis, I created a 3D reconstruction of the whole mouse brain vessels and trace the vascular structure of it. From the tracing result, the geometrical features (diameter, number of bifurcation point, length, surface, and volume) of the whole brain vascular structure were analyzed. I was able to obtain richer blood vessel information and analyze the vascular structure of the whole mouse brain when using Otsu's threshold method through 3D reconstruction, tracing, and the total percentage of volume results.

(4) I proposed a CNN based method to automatically classify impaired mouse brain images in the KESM dataset. I could get performance evaluation results of the image classification ("good" and "impaired") accuracy, precision, recall, and F1 score of the trained CNN and SVM models. The CNN model showed higher accuracy, precision, and F1 score than that of the SVM ones, which indicates that the approach using CNN is better for classifying the impaired image data obtained from a serial sectioning process such as the KESM dataset. The accuracy, precision, recall and F1 score of image classification by the CNN model when the training iteration value is set to 4,000, 8,000 and 12,000, confirm that the change of the corresponding values is not large even if the training iteration value is increased. I expect that this method could be a great help in screening damaged or impaired images in the future KESM datasets.

Overall, the studies in this dissertation enable the full tracing and analysis of the whole mouse brain at submicrometer resolution along with the systematic cleaning to remove and consolidate

erroneous images, automatically. I expect the results of this dissertation can provide rich insights into the brain for neuroscience researchers.

REFERENCES

[1] Fadilah Ab Hamid, Mohd Zulfaezal Che Azemin, Adzura Salam, Amilia Aminuddin, Norsyazwani Mohd Daud, and Ilyanoon Zahari. Retinal vasculature fractal dimension measures vessel density. *Current eye research*, 41(6):823–831, 2016.

[2] Martín Abadi, Ashish Agarwal, Paul Barham, Eugene Brevdo, Zhifeng Chen, Craig Citro, Greg S Corrado, Andy Davis, Jeffrey Dean, Matthieu Devin, et al. Tensorflow: Large-scale machine learning on heterogeneous distributed systems. *arXiv preprint arXiv:1603.04467*, 2016.

[3] Mathias M Adankon and Mohamed Cheriet. Support vector machine. In *Encyclopedia of biometrics*, pages 1303–1308. Springer, 2009.

[4] Stephen P Amato, Feng Pan, Joel Schwartz, and Timothy M Ragan. Whole brain imaging with serial two-photon tomography. *Frontiers in neuroanatomy*, 10:31, 2016.

[5] Woo Kyung An. Automated reconstruction of neurovascular networks in knife-edge scanning microscope mouse and rat brain nissl stained data sets. Master's thesis, Texas A&M University, 2016.

[6] Wookyung An and Yoonsuck Choe. Automated reconstruction of neurovascular networks in knife-edge scanning microscope rat brain nissl data set. In *International Symposium on Visual Computing*, pages 439–448. Springer, 2016.

[7] Utkarsh Ayachit. The paraview guide: a parallel visualization application. 2015.

[8] TH Bär and JR Wolff. The formation of capillary basement membranes during internal vascularization of the rat's cerebral cortex. *Zeitschrift für Zellforschung und mikroskopische Anatomie*, 133(2):231–248, 1972.

[9] Christopher JC Burges. A tutorial on support vector machines for pattern recognition. *Data mining and knowledge discovery*, 2(2):121–167, 1998.

[10] RC Cannon, DA Turner, GK Pyapali, and HV Wheal. An on-line archive of reconstructed hippocampal neurons. *Journal of neuroscience methods*, 84(1):49–54, 1998.

[11] Ken Chatfield, Karen Simonyan, Andrea Vedaldi, and Andrew Zisserman. Return of the devil in the details: Delving deep into convolutional nets. *arXiv preprint arXiv:1405.3531*, 2014.

[12] Yoonsuck Choe, Louise C Abbott, Donghyeop Han, Pei-San Huang, John Keyser, Jaerock Kwon, David Mayerich, Zeki Melek, and Bruce H McCormick. Knife-edge scanning microscopy: high-throughput imaging and analysis of massive volumes of biological microstructures. *High-Throughput Image Reconstruction and Analysis: Intelligent Microscopy Applications*, pages 11–37, 2008.

[13] Yoonsuck Choe, David Mayerich, Jaerock Kwon, Daniel E Miller, Ji Ryang Chung, Chul Sung, John Keyser, and Louise C Abbott. Knife-edge scanning microscopy for connectomics research. In *Neural Networks (IJCNN), The 2011 International Joint Conference on*, pages 2258–2265. IEEE, 2011.

[14] Yoonsuck Choe, David Mayerich, Jaerock Kwon, Daniel E Miller, Chul Sung, Ji Ryang Chung, Todd Huffman, John Keyser, and Louise C Abbott. Specimen preparation, imaging, and analysis protocols for knife-edge scanning microscopy. *Journal of visualized experiments: JoVE*, (58), 2011.

[15] Ji Ryang Chung, Chul Sung, David Mayerich, Jaerock Kwon, Daniel E Miller, Todd Huffman, John Keyser, Louise C Abbott, and Yoonsuck Choe. Multiscale exploration of mouse brain microstructures using the knife-edge scanning microscope brain atlas. *Frontiers in neuroinformatics*, 5, 2011.

[16] Kwanghun Chung, Jenelle Wallace, Sung-Yon Kim, Sandhiya Kalyanasundaram, Aaron S Andalman, Thomas J Davidson, Julie J Mirzabekov, Kelly A Zalocusky, Joanna Mattis, Aleksandra K Denisin, et al. Structural and molecular interrogation of intact biological systems. *Nature*, 497(7449):332, 2013.

[17] NG Conradi, J Engvall, and JR Wolff. Angioarchitectonics of rat cerebellar cortex during pre-and postnatal development. *Acta neuropathologica*, 50(2):131–138, 1980.

[18] Corinna Cortes and Vladimir Vapnik. Support-vector networks. *Machine learning*,

20(3):273–297, 1995.

[19] Sarbani Datta and Monisha Chakraborty. Patellar fracture analysis using segmentation and global thresholding techniques. In *Computational Intelligence and Information Technology: First International Conference, CIIT 2011, Pune, India, November 7-8, 2011. Proceedings*, volume 250, page 171. Springer, 2011.

[20] Mark De Berg, Marc Van Kreveld, Mark Overmars, and Otfried Cheong Schwarzkopf. Computational geometry. In *Computational geometry*, pages 1–17. Springer, 2000.

[21] Jack C de la Torre. Is alzheimer's disease a neurodegenerative or a vascular disorder? data, dogma, and dialectics. *The Lancet Neurology*, 3(3):184–190, 2004.

[22] JC De la Torre and T Mussivan. Can disturbed brain microcirculation cause alzheimer's disease? *Neurological research*, 15(3):146–153, 1993.

[23] Winfried Denk and Heinz Horstmann. Serial block-face scanning electron microscopy to reconstruct three-dimensional tissue nanostructure. *PLoS biology*, 2(11):e329, 2004.

[24] Luigi Yuri Di Marco, Eszter Farkas, Chris Martin, Annalena Venneri, and Alejandro F Frangi. Is vasomotion in cerebral arteries impaired in alzheimer's disease? *Journal of Alzheimer's Disease*, 46(1):35–53, 2015.

[25] Tiago Ferreira and Wayne Rasband. Imagej user guide. *ImageJ/Fiji*, 1, 2012.

[26] Emile Fiesler and Russell Beale. *Handbook of neural computation*. CRC Press, 1996.

[27] Andrea Frome, Greg S Corrado, Jon Shlens, Samy Bengio, Jeff Dean, Tomas Mikolov, et al. Devise: A deep visual-semantic embedding model. In *Advances in neural information processing systems*, pages 2121–2129, 2013.

[28] M Fukui et al. Guidelines for the diagnosis and treatment of spontaneous occlusion of the circle of willis (moyamoya'disease). *Clinical neurology and neurosurgery*, 99:S238–S240, 1997.

[29] Antonios Georgantzoglou, Joakim da Silva, and Rajesh Jena. Image processing with matlab and gpu. In *MATLAB Applications for the Practical Engineer*. InTech, 2014.

[30] Charles R Giardina and Edward R Dougherty. Morphological methods in image and signal

processing. *Engelwood Cliffs: Prentice Hall, 1988*, 1988.

[31] Rafael C Gonzalez and Richard E Woods. Image processing toolbox user's guide. *The Mathworks. Inc*, 2000.

[32] Ian Goodfellow, Yoshua Bengio, and Aaron Courville. *Deep Learning*. MIT Press, 2016. `http://www.deeplearningbook.org`.

[33] KJ Hayworth, N Kasthuri, R Schalek, and JW Lichtman. Automating the collection of ultrathin serial sections for large volume tem reconstructions. *Microscopy and Microanalysis*, 12(S02):86, 2006.

[34] T Huang, G Yang, and G Tang. A fast two-dimensional median filtering algorithm. *IEEE Transactions on Acoustics, Speech, and Signal Processing*, 27(1):13–18, 1979.

[35] David H Hubel and Torsten N Wiesel. Receptive fields of single neurones in the cat's striate cortex. *The Journal of physiology*, 148(3):574–591, 1959.

[36] David H Hubel and Torsten N Wiesel. Receptive fields, binocular interaction and functional architecture in the cat's visual cortex. *The Journal of physiology*, 160(1):106–154, 1962.

[37] O Hunziker, H Frey, and U Schulz. Morphometric investigations of capillaries in the brain cortex of the cat. *Brain research*, 65(1):1–11, 1974.

[38] Rajesh N Kalaria. Cerebral vessels in ageing and alzheimer's disease. *Pharmacology & therapeutics*, 72(3):193–214, 1996.

[39] Mehmet Kanbay, Laura-Gabriela Sánchez-Lozada, Martha Franco, Magdalena Madero, Yalcin Solak, Bernardo Rodriguez-Iturbe, Adrian Covic, and Richard J Johnson. Microvascular disease and its role in the brain and cardiovascular system: a potential role for uric acid as a cardiorenal toxin, 2010.

[40] Alex Krizhevsky, Ilya Sutskever, and Geoffrey E Hinton. Imagenet classification with deep convolutional neural networks. In *Advances in neural information processing systems*, pages 1097–1105, 2012.

[41] G Landini. Auto threshold (imagej), 2009.

[42] Stéphane Laurent, Sandrine Katsahian, Céline Fassot, Anne-Isabelle Tropeano, Isabelle

Gautier, Brigitte Laloux, and Pierre Boutouyrie. Aortic stiffness is an independent predictor of fatal stroke in essential hypertension. *Stroke*, 34(5):1203–1206, 2003.

[43] Bàrbara Laviña. Brain vascular imaging techniques. *International journal of molecular sciences*, 18(1):70, 2016.

[44] Yann LeCun, Bernhard E Boser, John S Denker, Donnie Henderson, Richard E Howard, Wayne E Hubbard, and Lawrence D Jackel. Handwritten digit recognition with a back-propagation network. In *Advances in neural information processing systems*, pages 396–404, 1990.

[45] Yann LeCun, Léon Bottou, Yoshua Bengio, and Patrick Haffner. Gradient-based learning applied to document recognition. *Proceedings of the IEEE*, 86(11):2278–2324, 1998.

[46] Yann LeCun, Koray Kavukcuoglu, and Clément Farabet. Convolutional networks and applications in vision. In *Circuits and Systems (ISCAS), Proceedings of 2010 IEEE International Symposium on*, pages 253–256. IEEE, 2010.

[47] Junseok Lee, Wookyung An, and Yoonsuck Choe. Mapping the full vascular network in the mouse brain at submicrometer resolution. In *Engineering in Medicine and Biology Society (EMBC), 2017 39th Annual International Conference of the IEEE*, pages 3309–3312. IEEE, 2017.

[48] Junseok Lee, Jaewook Yoo, and Yoonsuck Choe. Tracing and analysis of the whole mouse brain vasculature with systematic cleaning to remove and cosolidate erroneous images. In *Engineering in Medicine and Biology Society (EMBC), 2018 40th Annual International Conference of the IEEE*. IEEE, 2018.

[49] Yik Ching Lee, Alys R Clark, Matthew K Fuld, Susan Haynes, Abhay A Divekar, Eric A Hoffman, and Merryn H Tawhai. Mdct-based quantification of porcine pulmonary arterial morphometry and self-similarity of arterial branching geometry. *Journal of Applied Physiology*, 114(9):1191–1201, 2013.

[50] Sungjun Lim, Michael R Nowak, and Yoonsuck Choe. Automated neurovascular tracing and analysis of the knife-edge scanning microscope rat nissl data set using a computing

cluster. In *Engineering in Medicine and Biology Society (EMBC), 2016 IEEE 38th Annual International Conference of the*, pages 6445–6448. IEEE, 2016.

[51] Zhang Lin-Yuan et al. Clarity for high-resolution imaging and quantification of vasculature in the whole mouse brain. *Aging and Disease*, page 0, 2017.

[52] Erlen Lugo-Hernandez, Anthony Squire, Nina Hagemann, Alexandra Brenzel, Maryam Sardari, Jana Schlechter, Eduardo H Sanchez-Mendoza, Matthias Gunzer, Andreas Faissner, and Dirk M Hermann. 3d visualization and quantification of microvessels in the whole ischemic mouse brain using solvent-based clearing and light sheet microscopy. *Journal of Cerebral Blood Flow & Metabolism*, 37(10):3355–3367, 2017.

[53] Robert Mash, Brett Borghetti, and John Pecarina. Improved aircraft recognition for aerial refueling through data augmentation in convolutional neural networks. In *International Symposium on Visual Computing*, pages 113–122. Springer, 2016.

[54] M Mato and S Ookawara. A simple method for observation of capillary nets in rat brain cortex. *Experientia*, 35(4):501–503, 1979.

[55] David Mayerich, L Abbott, and B McCormick. Knife-edge scanning microscopy for imaging and reconstruction of three-dimensional anatomical structures of the mouse brain. *Journal of microscopy*, 231(1):134–143, 2008.

[56] David Mayerich, Jaerock Kwon, Yoonsuck Choe, Louise Abbott, and John Keyser. Constructing high resolution microvascular models. In *Third Workshop on Microscopic Image Analysis with Applications in Biology*, 2008.

[57] David Mayerich, Bruce H McCormick, and John Keyser. Noise and artifact removal in knife-edge scanning microscopy. In *2007 4th IEEE International Symposium on Biomedical Imaging: From Nano to Macro*, pages 556–559. IEEE, 2007.

[58] David Matthew Mayerich. *Imaging and computational methods for exploring sub-cellular anatomy*. PhD thesis, Citeseer, 2009.

[59] Bruce H McCormick. System and method for imaging an object, June 1 2004. US Patent 6,744,572.

[60] Bruce H McCormick and DM Mayerich. Three-dimensional imaging using knife-edge scanning microscopy. *Microscopy and Microanalysis*, 10(S02):1466, 2004.

[61] Helen Michaloudi, Christos Batzios, Ioannis Grivas, Maria Chiotelli, and Georgios C Papadopoulos. Developmental changes in the vascular network of the rat visual areas 17, 18 and 18a. *Brain research*, 1103(1):1–12, 2006.

[62] Kristina D Micheva and Stephen J Smith. Array tomography: a new tool for imaging the molecular architecture and ultrastructure of neural circuits. *Neuron*, 55(1):25–36, 2007.

[63] Kien Nguyen, Clinton Fookes, Arun Ross, and Sridha Sridharan. Iris recognition with off-the-shelf cnn features: A deep learning perspective. *IEEE Access*, 2017.

[64] Michael R Nowak and Yoonsuck Choe. Learning to distinguish cerebral vasculature data from mechanical chatter in india-ink images acquired using knife-edge scanning microscopy. In *Engineering in Medicine and Biology Society (EMBC), 2016 IEEE 38th Annual International Conference of the*, pages 3989–3992. IEEE, 2016.

[65] Anto Satriyo Nugroho, Arief Budi Witarto, and Dwi Handoko. Support vector machine. *Teori dan Aplikasinya dalam Bioinformatika, Ilmu Komputer. com, Indonesia*, 2003.

[66] Andre Obenaus, Michelle Ng, Amanda M Orantes, Eli Kinney-Lang, Faisal Rashid, Mary Hamer, Richard A DeFazio, Jiping Tang, John H Zhang, and William J Pearce. Traumatic brain injury results in acute rarefication of the vascular network. *Scientific reports*, 7(1):e239–e239, 2017.

[67] David L Olson and Dursun Delen. *Advanced data mining techniques*. Springer Science & Business Media, 2008.

[68] Nobuyuki Otsu. A threshold selection method from gray-level histograms. *IEEE transactions on systems, man, and cybernetics*, 9(1):62–66, 1979.

[69] Michael F O'Rourke and Michel E Safar. Relationship between aortic stiffening and microvascular disease in brain and kidney: cause and logic of therapy. *Hypertension*, 46(1):200–204, 2005.

[70] Hanchuan Peng, Alessandro Bria, Zhi Zhou, Giulio Iannello, and Fuhui Long. Extensi-

ble visualization and analysis for multidimensional images using vaa3d. *Nature protocols*, 9(1):193, 2014.

[71] Hanchuan Peng, Zongcai Ruan, Fuhui Long, Julie H Simpson, and Eugene W Myers. V3d enables real-time 3d visualization and quantitative analysis of large-scale biological image data sets. *Nature biotechnology*, 28(4):348–353, 2010.

[72] Michael J Pesavento, Caroline Miller, Katy Pelton, Molly Maloof, Corey E Monteith, Venkata Vemuri, and Megan Klimen. Knife-edge scanning microscopy for bright-field multi-cubic centimeter analysis of microvasculature. *Microscopy Today*, 25(4):14–21, 2017.

[73] Marius-Constantin Popescu, Valentina E Balas, Liliana Perescu-Popescu, and Nikos Mastorakis. Multilayer perceptron and neural networks. *WSEAS Transactions on Circuits and Systems*, 8(7):579–588, 2009.

[74] Judith Prewitt and Mortimer L Mendelsohn. The analysis of cell images. *Annals of the New York Academy of Sciences*, 128(1):1035–1053, 1966.

[75] Dale Purves. The visual system and the brain: Hubel and wiesel redux. *Purves, D.(2009). Brains: How They Seem to Work*, pages 105–122, 2009.

[76] Waseem Rawat and Zenghui Wang. Deep convolutional neural networks for image classification: A comprehensive review. *Neural computation*, 29(9):2352–2449, 2017.

[77] MATLAB Release. The mathworks. *Inc., Natick, Massachusetts, United States*, 488, 2013.

[78] Alfredo Rodriguez, Douglas B Ehlenberger, Patrick R Hof, and Susan L Wearne. Three-dimensional neuron tracing by voxel scooping. *Journal of neuroscience methods*, 184(1):169–175, 2009.

[79] Olga Russakovsky, Jia Deng, Hao Su, Jonathan Krause, Sanjeev Satheesh, Sean Ma, Zhiheng Huang, Andrej Karpathy, Aditya Khosla, Michael Bernstein, et al. Imagenet large scale visual recognition challenge. *International Journal of Computer Vision*, 115(3):211–252, 2015.

[80] Benjamin Schmid, Johannes Schindelin, Albert Cardona, Mark Longair, and Martin Heisenberg. A high-level 3d visualization api for java and imagej. *BMC bioinformatics*, 11(1):274,

2010.

[81] Jürgen Schmidhuber. Deep learning in neural networks: An overview. *Neural networks*, 61:85–117, 2015.

[82] William J Schroder, Kenneth M Martin, and Lisa S Avila. Vtk user's guide-vtk file formats, chapter 14. *Kitware Inc*, 2000.

[83] Mehmet Sezgin et al. Survey over image thresholding techniques and quantitative performance evaluation. *Journal of Electronic imaging*, 13(1):146–168, 2004.

[84] Karen Simonyan and Andrew Zisserman. Very deep convolutional networks for large-scale image recognition. *arXiv preprint arXiv:1409.1556*, 2014.

[85] Ankur Singhal. Skeletonization-based automated tracing and reconstruction of neurovascular networks in knife-edge scanning microscope mouse brain india ink dataset. Master's thesis, Texas A&M University, 2015.

[86] Johannes Stallkamp, Marc Schlipsing, Jan Salmen, and Christian Igel. The german traffic sign recognition benchmark: a multi-class classification competition. In *Neural Networks (IJCNN), The 2011 International Joint Conference on*, pages 1453–1460. IEEE, 2011.

[87] C Sung, J Chung, D Mayerich, J Kwon, D Miller, T Huffman, J Keyser, L Abbott, and Y Choe. Knife-edge scanning microscope brain atlas: A web-based, light-weight 3d mouse brain atlas. In *Front. Neuroinform. Conference Abstract: 4th INCF Congress of Neuroinformatics. doi: 10.3389/conf. fninf*, volume 36, 2011.

[88] Christian Szegedy, Wei Liu, Yangqing Jia, Pierre Sermanet, Scott Reed, Dragomir Anguelov, Dumitru Erhan, Vincent Vanhoucke, Andrew Rabinovich, et al. Going deeper with convolutions. Cvpr, 2015.

[89] Christian Szegedy, Vincent Vanhoucke, Sergey Ioffe, Jon Shlens, and Zbigniew Wojna. Rethinking the inception architecture for computer vision. In *Proceedings of the IEEE Conference on Computer Vision and Pattern Recognition*, pages 2818–2826, 2016.

[90] Luke Taylor and Geoff Nitschke. Improving deep learning using generic data augmentation. *arXiv preprint arXiv:1708.06020*, 2017.

[91] Philbert S Tsai, Beth Friedman, Agustin I Ifarraguerri, Beverly D Thompson, Varda Lev-Ram, Chris B Schaffer, Qing Xiong, Roger Y Tsien, Jeffrey A Squier, and David Kleinfeld. All-optical histology using ultrashort laser pulses. *Neuron*, 39(1):27–41, 2003.

[92] Harm J van de Haar, Jacobus FA Jansen, Matthias JP van Osch, Mark A van Buchem, Majon Muller, Sau May Wong, Paul AM Hofman, Saartje Burgmans, Frans RJ Verhey, and Walter H Backes. Neurovascular unit impairment in early alzheimer's disease measured with magnetic resonance imaging. *Neurobiology of aging*, 45:190–196, 2016.

[93] Chen Wang and Yang Xi. Convolutional neural network for image classification.

[94] Jingpeng Wu, Yong He, Zhongqin Yang, Congdi Guo, Qingming Luo, Wei Zhou, Shangbin Chen, Anan Li, Benyi Xiong, Tao Jiang, et al. 3d braincv: simultaneous visualization and analysis of cells and capillaries in a whole mouse brain with one-micron voxel resolution. *Neuroimage*, 87:199–208, 2014.

[95] Bohua Xie, Peng Miao, Yuhao Sun, Yongting Wang, and Guo-Yuan Yang. Micro-computed tomography for hemorrhage disruption of mouse brain vasculature. *Translational stroke research*, 3(1):174–179, 2012.

[96] Benyi Xiong, Anan Li, Yang Lou, Shangbin Chen, Ben Long, Jie Peng, Zhongqin Yang, Tonghui Xu, Xiaoquan Yang, Xiangning Li, et al. Precise cerebral vascular atlas in stereotaxic coordinates of whole mouse brain. *Frontiers in neuroanatomy*, 11:128, 2017.

[97] Lei Xu, Adam Krzyzak, and Ching Y Suen. Methods of combining multiple classifiers and their applications to handwriting recognition. *IEEE transactions on systems, man, and cybernetics*, 22(3):418–435, 1992.

[98] Larry S Yaeger, Richard F Lyon, and Brandyn J Webb. Effective training of a neural network character classifier for word recognition. In *Advances in neural information processing systems*, pages 807–816, 1997.

[99] Bin Yang, Jennifer B Treweek, Rajan P Kulkarni, Benjamin E Deverman, Chun-Kan Chen, Eric Lubeck, Sheel Shah, Long Cai, and Viviana Gradinaru. Single-cell phenotyping within transparent intact tissue through whole-body clearing. *Cell*, 158(4):945–958, 2014.

[100] Matthew D Zeiler and Rob Fergus. Visualizing and understanding convolutional networks. In *European conference on computer vision*, pages 818–833. Springer, 2014.

[101] Meng-Qi Zhang, Luo Zhou, Qian-Fang Deng, Yuan-Yuan Xie, Ti-Qiao Xiao, Yu-Ze Cao, Ji-Wen Zhang, Xu-Meng Chen, Xian-Zhen Yin, and Bo Xiao. Ultra-high-resolution 3d digitalized imaging of the cerebral angioarchitecture in rats using synchrotron radiation. *Scientific reports*, 5:14982, 2015.